

博士学位論文

Atmospheric concentration and deposition of cosmogenic ^7Be and airborne ^{210}Pb in Osaka Japan and identification of major chemical composition with size distributions of aerosols including air pollutants as the carrier of ^7Be

令和 3 年 2 月 9 日

大阪産業大学大学院

人間環境学研究科人間環境学専攻

NOITHONG PANNIPA

Doctoral Dissertation

Atmospheric concentration and deposition of cosmogenic ^7Be and airborne ^{210}Pb in Osaka Japan and identification of major chemical composition with size distributions of aerosols including air pollutants as the carrier of ^7Be

February 2021

Graduate School of Human Environment

Osaka Sangyo University

NOITHONG PANNIPA

Doctoral Dissertation

Authored by

NOITHONG PANNIPA

Supervised by

RYUTA HAZAMA

February 2021

Graduate School of Human Environment

Osaka Sangyo University

ABSTRACT

This study aimed to understand the behaviour of cosmogenic airborne ^7Be and airborne ^{210}Pb , and the relationship between the particle size distribution and major chemical composition of aerosols attached by ^7Be . Air dust samples, total deposition samples, and aerosol size distribution were collected at the rooftop of building No. 16, Osaka Sangyo University located in Daito, Osaka, Japan (34.71°N , 135.64°E ; the height above ground level was 31 m).

Air dust samples in near-surface air were collected weekly. The seasonal ^{210}Pb and ^7Be concentrations were determined from January 8, 2018 to December 31, 2020. The average monthly concentration of ^7Be ranged from 2.15 ± 0.28 to 8.84 ± 0.62 mBq/m^3 , and the average value was 5.04 ± 1.12 mBq/m^3 . The average monthly concentration of ^{210}Pb ranged from 0.43 ± 0.17 to 1.93 ± 0.02 mBq/m^3 , and the average value was 0.78 ± 0.30 mBq/m^3 . Despite their different origins and distribution throughout the atmosphere, they presented the same seasonal variation. Furthermore, there was a tendency for a maximum during the spring and autumn season, and a minimum during summer. The variation in concentration showed a strong correlation between ^{210}Pb and ^7Be ($\text{CC} = 0.72$). The seasonal pattern from the ^7Be concentration showed good agreement with the long-term study (15 years) at Sakai, Osaka, which was reported by Megumi et al. (2000). To understand the seasonal pattern of ^{210}Pb and ^7Be , the factors causing the variation were analysed. For ^7Be , the results showed a medium correlation for the total suspended particle (TSP) ($\text{CC} = 0.53$) and percentage of the relative humidity (%RH) ($\text{CC} = -0.40$), a weak correlation in precipitation ($\text{CC} = 0.32$) and particulate matter (PM) 2.5 ($\text{CC} = 0.32$), very weak in the sunspot number ($\text{CC} = -0.17$), and neutron flux from the cosmic rays ($\text{CC} = 0.02$). For ^{210}Pb , the results showed a strong correlation in TSP ($\text{CC} = 0.63$), and a weak correlation in pressure ($\text{CC} = -0.27$), wind speed ($\text{CC} = -0.25$), precipitation ($\text{CC} = 0.25$) and %RH ($\text{CC} = -0.23$), and very weak PM 2.5 ($\text{CC} = 0.12$). Although the local meteorological factors were necessary to understand the seasonal pattern of ^7Be and ^{210}Pb , the results showed almost a weak

correlation. Thus, the transportation processes of ^7Be and ^{210}Pb were investigated on a global scale. The air mass motions were estimated by using the NOAA HYSPLIT model, and the meteorological data sets from the Global Data Assimilation System (GDAS) to simulate the backward air mass trajectories. ^7Be was produced in the upper atmosphere; the heights were the troposphere where the long-range transportation of aerosols (2,000 m and 6,000 m) occurred, and the border between the troposphere and the stratosphere (20,000 m), which was the level of ^7Be production. Moreover, ^7Be was continuously produced in the lower stratosphere (70%) and upper troposphere (30%), as reported by Yoshimori (2005). The origin of ^{210}Pb came from the ground; the heights were 500 m, 1000 m, and 1,500 m, respectively, which were the atmospheric turbulence that strongly influenced the meteorology and dispersion. In summer, both ^7Be and ^{210}Pb showed an air mass almost passing over the Pacific Ocean, or lower latitudes that carried the low atmospheric concentration level. In winter, spring, and autumn, the air mass almost passed over the continent, or higher latitudes, which the origin of the air mass transported from Eastern and Northern China, and the far eastern part of Russia carried the high atmospheric concentration level.

Monthly deposition samples, including rain and atmospheric deposition, were collected from November 2019 to October 2020. The annual total depositions of ^7Be and ^{210}Pb were $1655 \pm 26 \text{ Bq/m}^2$ and $273 \pm 7 \text{ Bq/m}^2$, respectively. A very strong correlation between precipitation and total deposition of ^7Be ($\text{CC} = 0.88$) and ^{210}Pb ($\text{CC} = 0.85$) was observed. The annual deposition pattern of the total ^7Be and ^{210}Pb deposition showed a high level in March, July, and October. The ^7Be deposition pattern at Sakai, which was a long-term study, showed a spring peak pattern. The results of the current study showed a different pattern with Sakai because this study period was only for one year, and high precipitation was found in March, July, and October. Therefore, for the long-term study, the spring peak was expected in the area. The wet deposition was the main deposition in ^7Be (79.07 %) and ^{210}Pb (67.87%). Thus, high precipitation could increase the ^7Be and ^{210}Pb deposition of air by wash out.

In this study, the relationship between the size distribution of the ^7Be aerosol particles in the surface air and Particulate Matter's (PM) major chemical composition were analysed in size distributions to investigate the PM's main inorganic species in the atmospheric aerosol particles as a carrier of ^7Be . The main inorganic species of the PM were nitrate (NO_3^-), ammonium (NH_4^+), sulfate (SO_4^{2-}), and sea salt, which represented a 1:1 ratio of sodium ion (Na^+) and chloride ion (Cl^-). Every two weeks from June 6, 2020, to August 28, 2020, and in December 2020, aerosol size distributions were collected, and the aerosols were classified into 12 sizes ranging from 0.06 to 12.01 μm . The activity size distribution of the ^7Be -aerosols peaked in the 0.33 ~ 0.55 μm size range. The mass size distribution of NH_4^+ and SO_4^{2-} peaked in the 0.33 ~ 0.55 μm size range, NO_3^- peaked in the 2.20 ~ 3.90 μm size range, and Na^+ and Cl^- peaked in the 1.20 ~ 2.20 μm size range. For the inorganic species, the diameter of aerosol particles in summer was smaller than in winter because summer had lower humidity than winter. High relative humidity conditions resulted in an increased particle size of the atmospheric aerosols that were removed from the atmosphere by the influence of gravity. The dominant ionic species were SO_4^{2-} among anions and NH_4^+ among cations, and their mass median aerodynamic diameter (MMAD) was $0.63 \pm 0.15 \mu\text{m}$ and $0.61 \pm 0.15 \mu\text{m}$, respectively, which was almost identical to the activity median aerodynamic diameter (AMAD) of ^7Be activity size distribution (AMAD = $0.63 \pm 0.15 \mu\text{m}$). For the variation of the inorganic species and the variation of ^7Be , it was found that only SO_4^{2-} had good agreement with the variation of the ^7Be activity. SO_4^{2-} is an anthropogenic product produced by burning fossil fuels from the Asian continent, especially China. Thus, SO_4^{2-} would be the potential medium for ^7Be , and this inorganic species could be traced and predicted based on the behaviour of ^7Be .

Keywords

^7Be concentration, ^{210}Pb concentration, ^7Be deposition, ^{210}Pb deposition, seasonal variation, meteorological parameter, back trajectory, air mass origins, sulphate

ACKNOWLEDGMENTS

First I would like to thank my thesis adviser, Prof. Ryuta Hazama for his continuous consolation and advice academically, along with his support and motivation on fulfilling my thesis research.

I would like to thank Prof. Hisakazu Muramatsu, Chemistry Division, Faculty of Education, Shinshu University for providing much of the equipment required for this study, Prof. Hamasaki Tatsuhide, and Nanthapong Chantaraprachoom, Faculty of Design Technology, Osaka Sangyo University for measuring our sample by suing Ion Chromatography, Prof. Naofumi Akata, Department of Radiochemistry and Radioecology, Hirosaki-University for the resin, Prof. Ryo Horikoshi, Faculty of Design Technology, Department of Environmental Science and Technology, Osaka Sangyo University for the oven, and Prof. Umehara Saori, Research Center for Nuclear Physics, Osaka University for the low background measurement at Kamioka underground laboratory.

I would like to thank Rittirong Anawat, a doctoral student in our lab for kindness helping and supporting my work in many steps.

In addition, this work was supported by the Science Research Promotion Fund from the Promotion and Mutual Aid Corporation for Private Schools of Japan. Finally, my work is supported by the Japanese Government (MEXT) Scholarship.

CONTENT

Abstract	1
– Keywords	3
Acknowledgements	4
Chapter one: Introduction	8
1.1. Introduction	8
1.2. Research objectives	10
1.3. Radionuclides occurring in our natural environment	10
1.3.1 Naturally Occurring Radioactive Materials (NORM)	10
1.3.1.1 Cosmogenic radionuclides	10
1.3.1.2 Primordial Radionuclides	14
1.3.2 Technologically Enhanced Naturally Occurring Radioactive Materials (TENORM)	19
1.4 Environmental radioactivity and beryllium-7 (^7Be) and Lead-210 (^{210}Pb)	20
1.5 Surface air concentrations of ^7Be and ^{210}Pb	23
1.5.1 Surface air concentrations of ^7Be	23
1.5.2 Surface air concentrations of ^{210}Pb	29
1.6 Air pollution	31
1.6.1 Particulate matter (PM)	31
1.6.2 Aerosol transportation and global circulation patterns	33
1.7 Deposition of ^7Be and ^{210}Pb	35
1.7.1 Deposition of ^7Be	35
1.7.2 Deposition of ^{210}Pb	39

CONTENT (Cont.)

1.8 Environmental applications	40
Chapter two: Material and method	48
2.1 Sampling site	48
2.2 Radioactivity measurement	48
2.3 Detection Efficiency	54
2.4 Air dust	57
2.4.1 Samples collation and preparation	57
2.4.2 Atmospheric concentration (Bq/m ³)	59
2.4.3 Factors causing variation	60
2.4.4 The back trajectory simulation	61
2.5 Fallout density	68
2.5.1 Samples collation and preparation	68
2.5.2 Atmospheric deposition (Bq/m ²)	75
2.6 Aerosol size and Chemical form	75
Chapter Three: Results and discussion	81
3.1 Air dust	81
3.1.1 Ruthenium-106 (¹⁰⁶ Ru) measurement	81
3.1.2 ⁷ Be and ²¹⁰ Pb concentration	87
3.1.3 Factors causing variation of ⁷ Be and ²¹⁰ Pb concentration	90
3.1.4 The back trajectory simulation by using HYSPLIT simulation	96
3.2 Fallout density	105
3.3 Aerosol size and Chemical form	108

CONTENT (Cont.)

Chapter four: Conclusions	121
Appendix	127
Appendix 1 Weekly Be-7 and Pb-210 concentration	127
Appendix 2 Be-7 and Pb-210 deposition	131
Appendix 3 Result from the impactor	132

CHAPTER ONE

INTRODUCTION

1.1 Introduction

Radionuclides occurring in our natural environment can be classified in three general categories: (1) primordial radionuclides, i.e., nuclides which have survived since the time when the elements formed, and their progeny nuclides; (2) cosmogenic radionuclides, formed continuously by the interactions of cosmicray particles with matter; and (3) artificial radionuclides, introduced by human activities, e.g., by detonations of nuclear weapons. Radioecology is the study of the occurrence of these radionuclides in the natural environment. This includes the atmosphere, hydrosphere and lithosphere. Studies of environmental radionuclides can provide us with useful geophysical information, such as the timescales over which natural systems are changing or evolving and the underlying mechanistic causes. They can also be used to assess the radiological or radioecological effects of ambient radioactivity.

Beryllium-7 (^7Be) is a cosmogenic radionuclide formed in the atmosphere when cosmic-ray produced neutrons and protons disintegrate the atomic nucleus of nitrogen and oxygen into lighter fragments. It has a relatively short half-life of approximately 53 days. ^7Be is found naturally in air, rainwater, soils and sediments, vegetation, as well as lake, estuarine and ocean waters. The use of ^7Be as a tracer of natural processes has recently been realized, and a number of nuclear techniques have been developed to support ongoing research in this area. Nevertheless, most applications of ^7Be require a detailed understanding of its distribution within different natural systems. Such an understanding is still incomplete.

^{210}Pb is a natural radionuclide in the ^{238}U decay series with relatively long half-life ($T_{1/2} = 22.3$ y). Airborne ^{210}Pb is produced from its precursor, ^{222}Rn ($T_{1/2} = 3.82$ d), emanated from the ground surface. The ^{210}Pb attaches to aerosol particles near the ground surface, and is transported through the atmosphere. Both ^{210}Pb and ^{210}Po in the atmosphere have been used as tracers for studying the mean atmospheric residence time of aerosols and their transportation process through the boundary layer [1].

It is well known that variation of ^7Be concentration in surface air depends on many factors such as solar activity, metrological parameter [2, 3] and particulate pollutants such as Particulate Matter 2.5 (PM_{2.5}). Many studies find that ^7Be concentration is increased during periods of minimal precipitation, indicating the washout of radioactive aerosols by rainfalls [2]. In case of particulate pollutants, the concentration and variation of PM may alter the behavior of ^7Be in the atmosphere because ^7Be is attached to PM after transportation to the lower atmosphere. Accordingly, the behavior of ^7Be relates to the distribution of particulate pollutants [4]. Many researchers have observed the relationship between ^7Be and particulate matter (PM) and note that the concentration and variation of PM can alter the behavior of ^7Be and its atmospheric distribution [4, 5]. However there have been few studies that have estimated the size distributions of atmospheric aerosols attached by ^7Be . It is well known that nitrate (NO_3^-), ammonium (NH_4^+), sulfate (SO_4^{2-}) and sea salt representing a 1:1 ratio of sodium ion (Na^+) and chloride ion (Cl^-) are significant constituents of the [6] the understanding in this field is unclear. Therefore, studies of ^7Be and ^{210}Pb , such as those presented in this thesis, will greatly add to our understanding of the behavior of this radionuclide in the environment and its future use for the evaluation of environmental problems.

1.2 Research objectives

The overall objectives of this research were to (1) measure ^7Be and ^{210}Pb activity in surface air and describe the annual cycle of ^7Be and ^{210}Pb concentrations in surface air and identify factors controlling this behavior; (2) analyze air mass origins by back trajectory analysis for evaluating atmospheric ^7Be and ^{210}Pb concentrations; (3) measure ^7Be and ^{210}Pb activity in wet and dry deposition and identify factors controlling the depositional flux of this radionuclide; and (4) study the relationship between the particle size and chemical form of aerosol attached by ^7Be .

1.3 Radionuclides occurring in our natural environment

The radioactivity on Earth consists of naturally produced radioisotopes and anthropogenic radioactive contamination initiated during the nuclear era (see Anthropogenic Radioactivity; Civilian Nuclear Accidents). Radionuclides occurring in our natural environment categorized into two categories based on the origin of production of the radioisotope: Naturally Occurring Radioactive Materials (NORM), which was categorized into two categories were cosmogenic radionuclides and primordial radionuclides and Technologically Enhanced Naturally Occurring Radioactive Materials (TE-NORM) [7].

1.3.1 Naturally Occurring Radioactive Materials (NORM)

1.3.1.1 Cosmogenic radionuclides

The Earth is constantly bombarded by cosmic radiation composed principally of high-energy particles emanating from extraterrestrial sources. Depending on its origin, the composition of the cosmic radiation varies greatly. Galactic cosmic radiation flux is typically composed of protons (87%), α -particles (11%), a few heavier nuclei with atomic numbers between 4 and 26 ($\sim 1\%$), and some high-energy electrons ($\sim 1\%$) [8]. In comparison, solar cosmic radiation,

produced during solar energetic events, has a much higher proton composition (98%) and lower α -particle contribution (2%) and has no heavier nuclei or energetic electrons [9]. Upon entering the Earth's atmosphere, cosmic radiation interacts with the gaseous and particulate constituents to produce a variety of cosmogenic radioisotopes (**Table 1.1**) [7]. These interactions often generate a cascade of secondary particles such as protons and neutrons (**Fig. 1.1**), which in turn will interact with target nuclei to produce additional cosmogenic nuclides. The largest number of nuclear transformations induced by cosmic radiation occurs within the Earth's atmosphere, where most of the cosmic ray energy is dissipated. In contrast to what occurs within the atmosphere, the rate of nuclear transformations taking place at the Earth's surface is several hundred times smaller, [10]. However, the omnipresence of some elements in soil and water relative to the atmosphere is responsible for the much higher partitioning of some cosmogenic nuclides in the lithosphere (**Table 1.2**). Most cosmogenic radionuclides are produced by one of the three nuclear rearrangement types involving cosmic particles: spallation, neutron capture, or muon capture. Spallation, a process where a nucleus splits into several lighter nuclei, proton, neutron, and muon after collision with a high-energy particle, is by far the most common mode of production of cosmogenic radionuclides in the atmosphere [11]. Neutron and slow muon capture are far more common processes at the Earth's surface, as the energy of the high-energy particles required for spallation is already dissipated in the upper layers of the atmosphere [7].

Table 1.1 Cosmogenic radionuclides [7].

Nuclide	Half-life ^(a)	Decay mode ^(b)	Particle energy (MeV) ^(c)	Production rate atmosphere (atom/cm/s) ^(d)	Atmospheric global inventory (PBq) ^(d)
³ H	12.32 y	β^-	0.0186	0.25	1275
⁷ Be	53.28 d	EC	(0.862)	0.081	413
¹⁰ Be	1.56×10^6 y	β^-	0.555	0.045	230
¹⁴ C	5 715 y	β^-	0.1565	2.5	12 750
²² Na	2.605 y	β^+	0.545	8.6×10^{-5}	0.44
²⁶ Al	7.1×10^5 y	β^+	1.6	1.4×10^{-4}	0.71
²⁸ Mg	21.0 h	β^-	0.459	-	-
³¹ Si	2.6 h	β^-	1.49	-	-
³² Si	160 y	β^-	0.213	1.6×10^{-4}	0.82
³² P	14.28 d	β^-	1.710	8.1×10^{-4}	4.1
³³ P	25.3 d	β^-	0.249	6.8×10^{-4}	3.5
³⁵ S	87.2 d	β^-	0.167	1.4×10^{-4}	7.1
³⁸ S	2.8 h	β^-	(3.0)	-	-
³⁶ Cl	3.01×10^5 y	β^-	0.709	1.1×10^{-3}	5.6
³⁸ Cl	37.2 min	β^-	(4.91)	-	-
³⁹ Ar	268 y	β^-	0.5565	5.6×10^{-3}	28.6
⁵³ Mn	3.7×10^6 y	EC	(0.596)	-	-
⁸¹ Kr	2.2×10^5 y	EC	(0.28)	1.5×10^{-7}	0.005
⁸⁵ Kr	10.7 y	β^-	(0.67)	-	0.0005 ^(e)

^(a) Seconds (s), minutes (min), days (d), years (y).

^(b) EC = electron capture.

^(c) Values within parentheses are decay energies.

^(d) From UNSCEAR [12], except where noted.

^(e) From Rozanski [13].

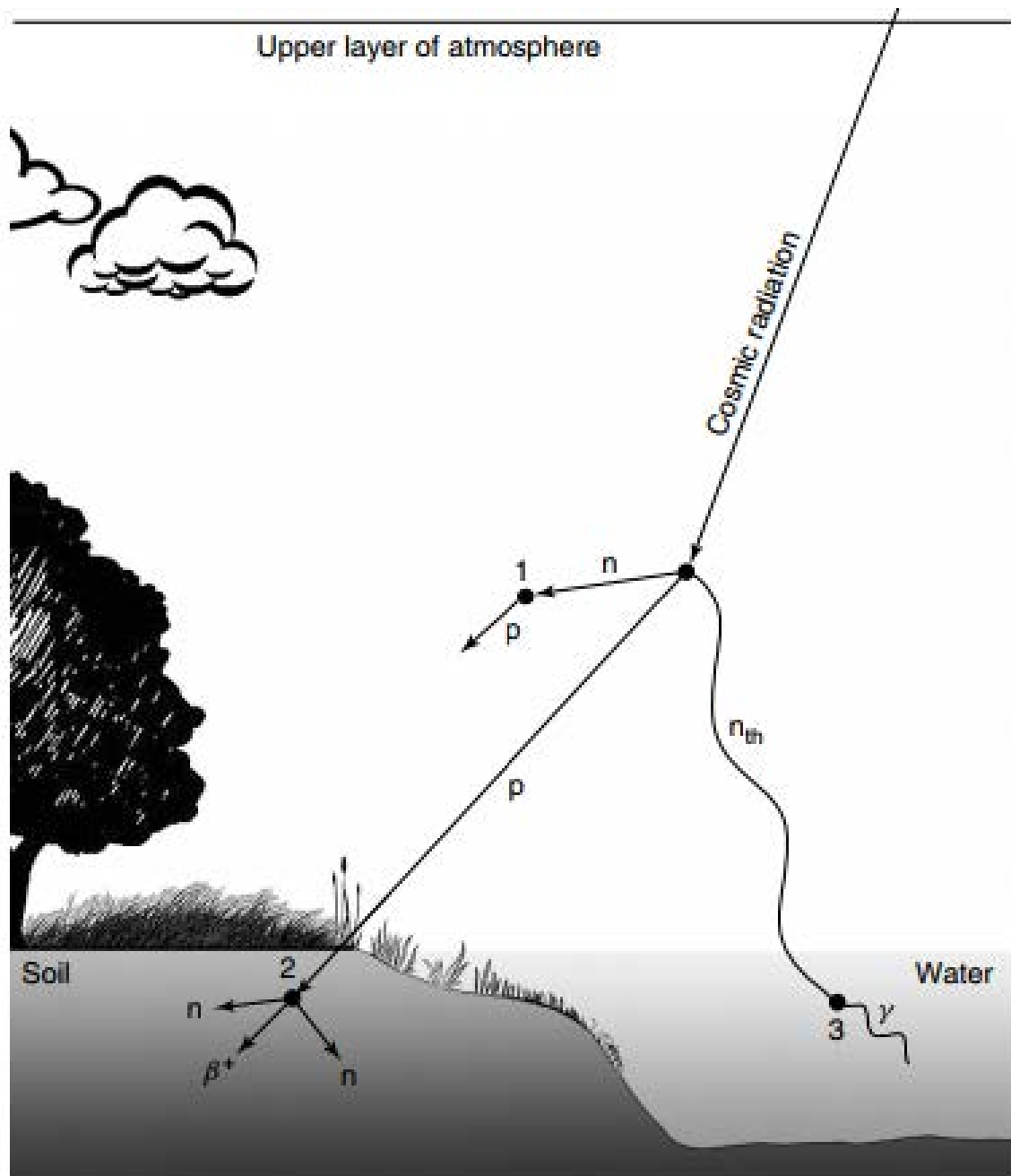


Fig. 1.1 The major components of a cosmic-ray cascade production of secondary particles in the atmosphere and rock. Protons (p), neutrons (n), thermal neutrons (n_{th}), and γ radiation (γ) are represented. Numbers in the figure refer to examples of cosmogenic nuclide interactions in the environment [7].

Table 1.2 Steady-state fractional inventories as a percentage of cosmogenic radionuclides in various exchange reservoirs [7].

Exchange reservoir	Atmosphere		Ecosphere			
	Stratosphere	Troposphere	Earth surface	Mixed oceanic layer	Deep oceanic layer	Ocean sediments
^3H	6.8	0.4	27	35	30	0
^7Be	60	11	8	20	0.2	0
^{10}Be	3.7×10^{-5}	0.23	29 ^(a)	5.7×10^{-4}	0.01	71
^{14}C	0.3	1.6	4	2.2	92	0.4
^{22}Na	25	1.7	21	44	0.4	0
^{26}Al	1.3×10^{-4}	7.7×10^{-6}	29 ^(a)	1.4×10^{-3}	7×10^{-3}	71
^{32}Si	0.19	0.11	29 ^(a)	0.35	68	2.8
^{32}P	60	24	4.7	11	0.01	0
^{33}P	64	16	5.6	13	0.07	0
^{35}S	57	8	10	24	0.4	0
^{36}Cl	1×10^{-4}	6×10^{-6}	29 ^(a)	1.4	69	0
^{39}Ar	16	83	0	0.02	0.3	0
^{81}Kr	16	82	0	0.4	2	0

^(a) Part of the inventory for this reservoir is carried by silt or dust into the ocean before decay.

1.3.1.2 Primordial Radionuclides

Primordial radioactivity originates from radioisotopes which have half-lives comparable to the age of the Earth (4.5×10^9 years). Because of their long half-lives, primordial radionuclides have not decayed beyond the point of non-detection. **Fig. 1.2** illustrates the remaining activity as a function of time for six radionuclides with half-lives ranging from 10^7 to 10^{10} years. Radionuclides with shorter half-lives, exemplified by ^{236}U ($T_{1/2} = 2.37 \times 10^7$ years) in **Fig. 1.2**, have activity levels that are negligible at the present time. Typically (see Uranium), a radionuclide present during the formation of the Earth but with a half-life of 10^8 years or shorter would currently have a remaining activity of less than 2.8×10^{-12} % of its original activity. Therefore, all primordial radionuclides found on Earth have half-lives greater than 5×10^8 years [7].

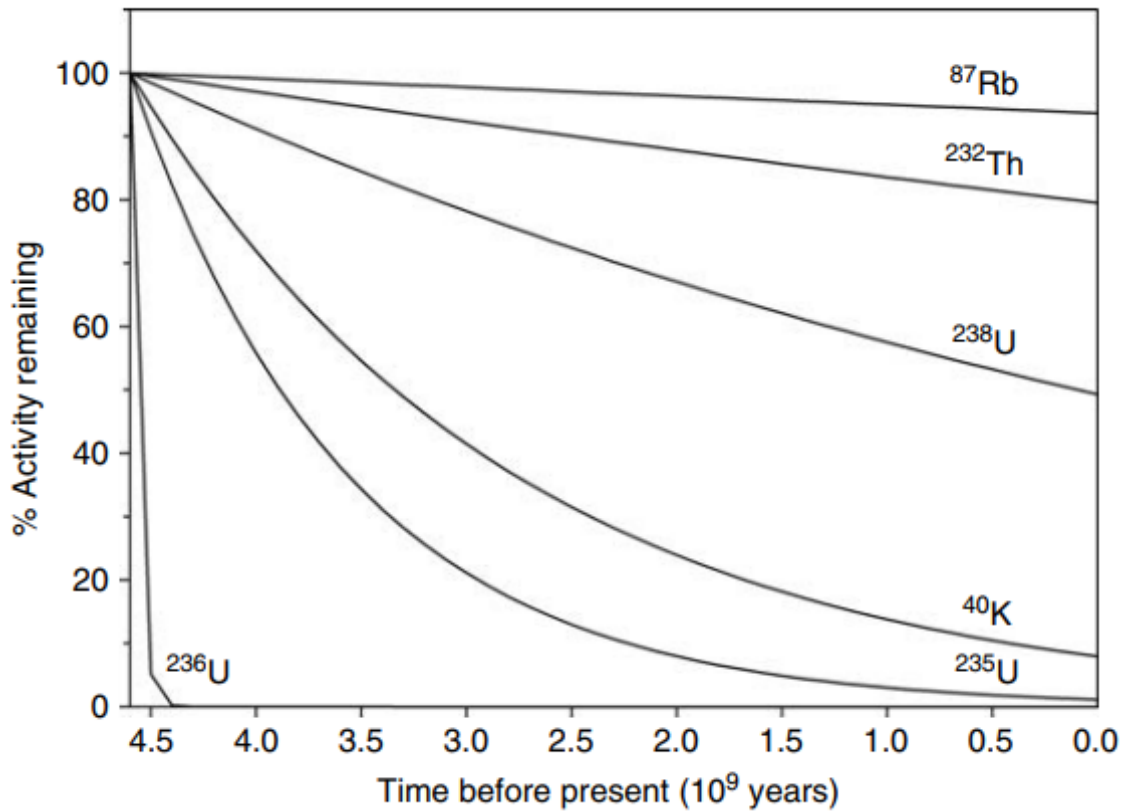


Fig. 1.2 Remaining activity of radionuclides (% of original activity) on Earth from Earth's formation until today [7].

The vast majority of the natural radioactivity detected on Earth and its related dose results from radionuclides belonging to the decay series which have primordial origins. While there were three naturally occurring decay chains, which begin with one of three long-lived parent nuclides. The three decay chains, namely the ^{232}Th or thorium decay chain ($4n$), the ^{238}U or uranium decay chain ($4n + 2$), and the ^{235}U decay chain, also referred to as the actinium decay chain ($4n + 3$), are illustrated in **Fig. 1.3 – 1.5**, respectively. The notations $4n$, $4n + 2$, and $4n + 3$ refer to the mass number A for all nuclides in the respective decay chains, where n is a positive integer between 50 and 60 [7, 15].

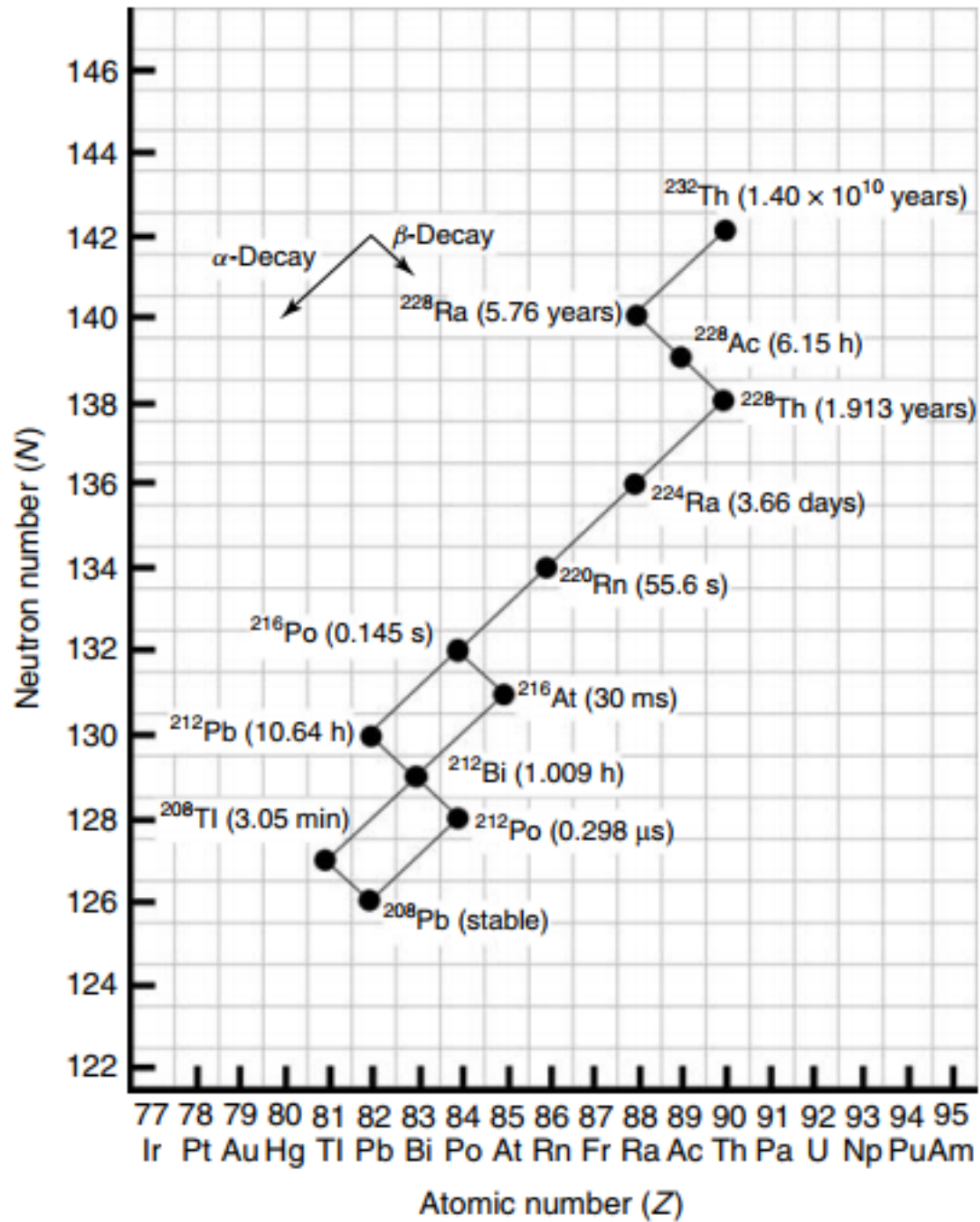


Fig. 1.3 Thorium radioactive decay series (4n series) [7].

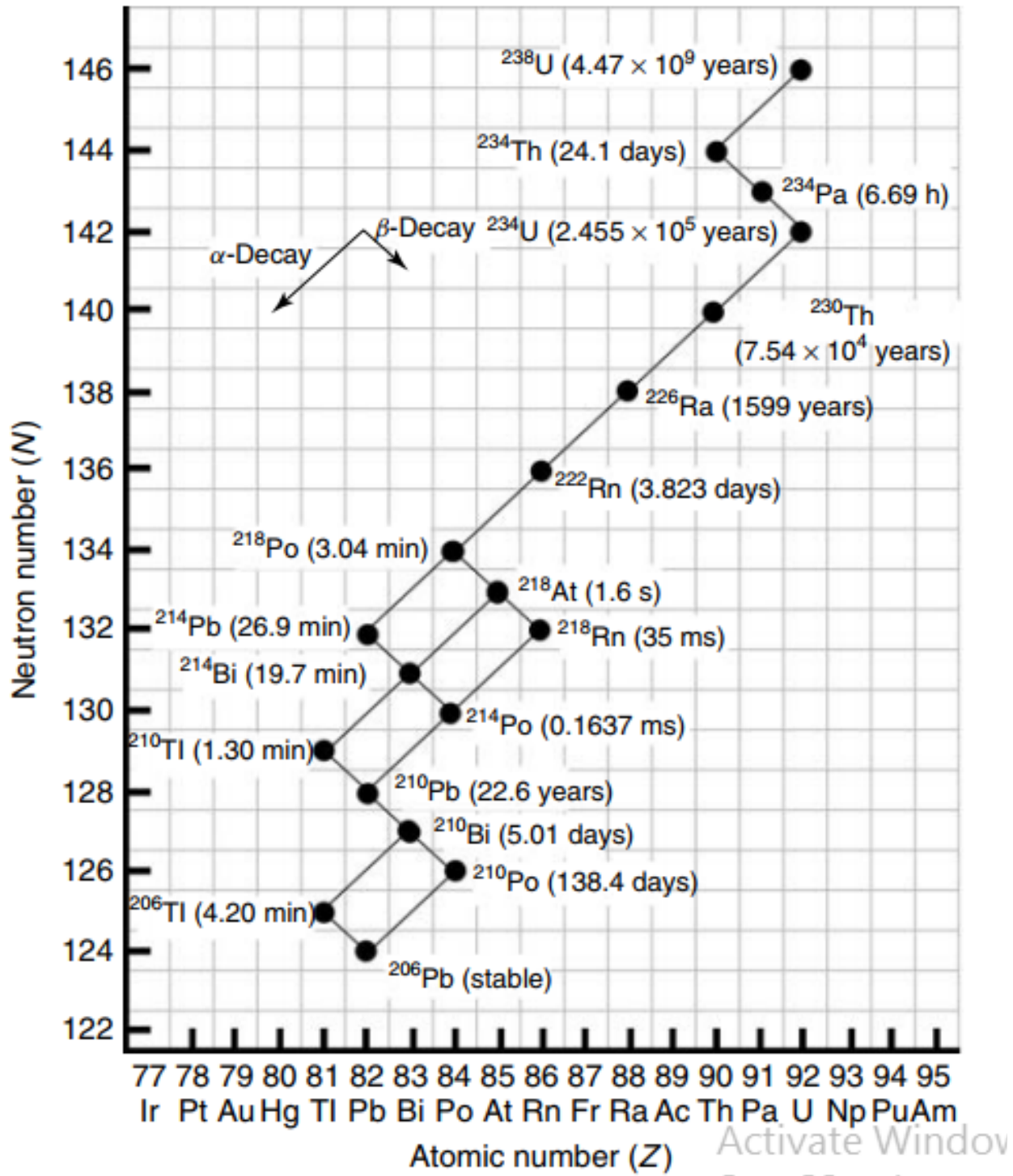


Fig. 1.4 Uranium radioactive decay series ($4n + 2$ series) [7].

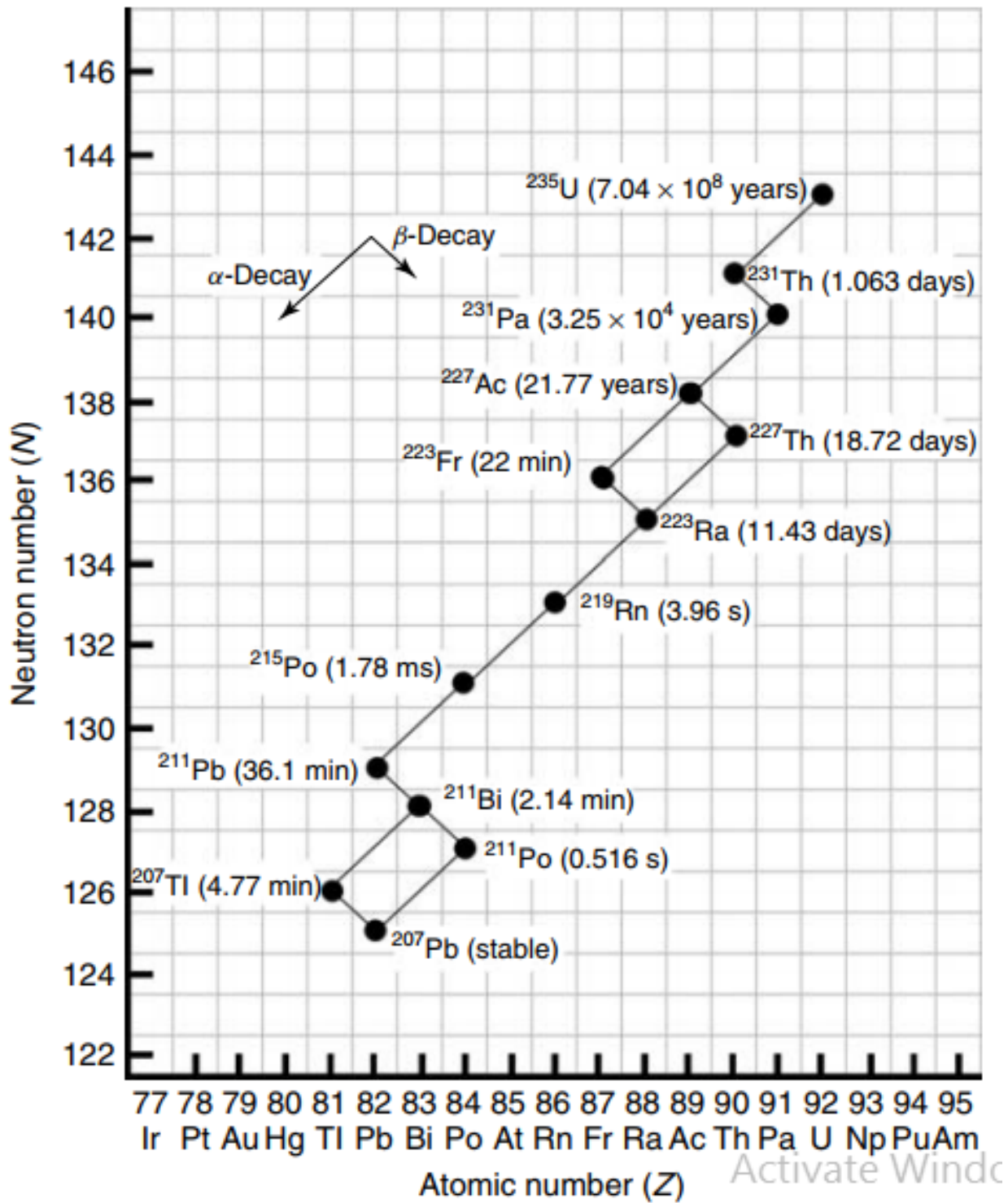


Fig. 1.5 Actinium radioactive decay series ($4n + 3$ series) [7].

1.3.2 Technologically Enhanced Naturally Occurring Radioactive Materials (TENORM)

While not a source of production of natural radionuclides, TENORM is artificial radionuclides responsible for the regional, national, and international distribution of many natural radionuclides in the environment. For this reason, they are briefly discussed in this section. TENORM, a term first coined by Gesell and Pritchard in 1975 [16] describes the concentration of NORM modified to be used in consumer products and other human adaptations. Mining, fertilizer production, fossil fuel use, smelting, and water treatment and purification are examples of human activities known to modify the level of environmental radioactivity, especially in soil, water, and air. The following paragraph highlights how some aspects of human activities magnify the level of natural radioactivity present [7]. Example of artificial and their origin show in **Table 1.3**.

Table 1.3 Example of artificial radionuclides and their origin [17].

Isotope	Half-live (yr)	Origin
^{60}Co	5.3	Activation of ^{59}Co – from test tower steel and from soil
^{106}Ru	1.02	Fission product
^{133}Ba	10.5	Activation of ^{132}Ba . Baratol - $\text{Ba}(\text{NO}_3)_2$ was part of explosive lens system of the Gadget
^{137}Cs	30	Fission product
$^{152}, ^{154}\text{Eu}$	13.3 / 8.8	Activation of stable isotopes $^{151}, ^{153}\text{Eu}$ in soil by slow neutrons
^{155}Eu	4.8	Fission product
^{239}Pu	24110	Principle isotope of nuclear fuel
^{241}Am	433	Mostly present as daughter product of ^{241}Pu (beta emitter), produced mainly from ^{239}Pu during the explosion via double-neutron capture. Based on ^{241}Am ingrowth activity of ^{241}Pu is possible to determine.

1.4 Environmental radioactivity and beryllium-7 and Lead-210

Beryllium-7 (half-life 53.29 d) is one of the radionuclide produced by spallation reactions of cosmic rays with light atmospheric nuclei, such as carbon, nitrogen and oxygen. Approximately 70% of ^7Be produced in the stratosphere, with the remaining 30% produced in the troposphere. A residence time is estimated about a year in the stratosphere, and about six weeks in the troposphere. Most of the ^7Be that are produced in the stratosphere don't reach the troposphere except during spring when seasonal thinning of the tropopause takes place at mid-latitudes, resulting in air exchange between stratosphere and troposphere. ^7Be rapidly associates primarily with submicron-sized aerosol particles. Gravitational settling and precipitation processes largely accomplish transfer to the earth's surface. ^7Be associated with aerosol particles is an ideal tool with which to study atmospheric transport processes. ^7Be quickly becomes an aerosol associated species. It is therefore susceptible to the same transport and deposition processes governing the aerosol, making it a useful atmospheric tracer such as atmospheric pollution, ^7Be is attached to Particulate Matter (PM) after transportation to the lower atmosphere. Accordingly, the behavior of ^7Be relates to the distribution of particulate pollutants [18, 19]. After production of ^7Be , it reacts with air constituents and turns into atoms or ^7BeO or $^7\text{Be}(\text{OH})_2$ molecules, which attached to available aerosol particles (0.07 to 2.00 μm). ^7Be condenses on aerosol population, growing by condensation of non-radioactive species [20, 21] ^7Be aerosols in high relative humidity conditions become more intense, resulting in increased particle size of atmospheric aerosols and are removed from the atmosphere [22, 23]. Transformation of this aerosol as it traverses the atmosphere can occur through a number of physical, chemical and meteorological processes (e.g. coagulation of ultra-fine particles, fog and cloud droplet formation, evaporation and condensation, washout, rainout and sedimentation, and contributions of dust storms and combustion products to the tropospheric aerosol mixture)

which determine the overall activity size distribution of ^7Be on the surface air aerosol population [24]. ^7Be disintegrates by electron capture either directly to the ground state of ^7Li (89.56%) or via the 477 keV of ^7Li (10.44%). Its decay scheme shows in **Fig. 1.6**.

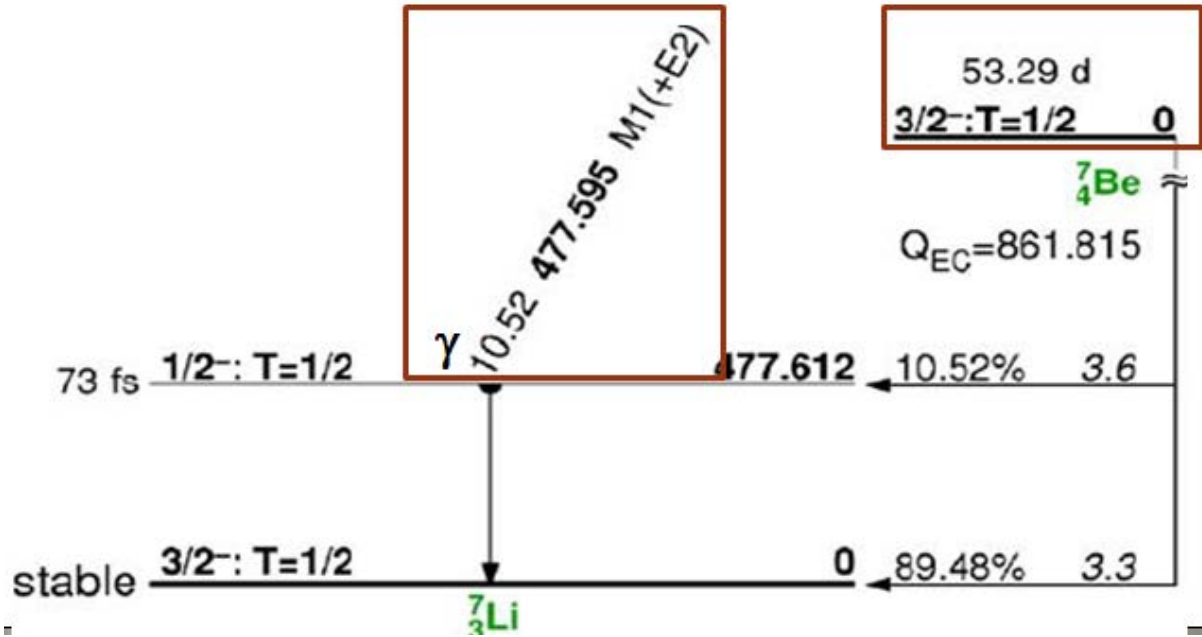


Fig. 1.6 Decay scheme of ^7Be [25].

Lead-210 ($T_{1/2} = 22.3$ y) is one of the progenies of ^{222}Rn ($T_{1/2} = 3.8$ d) generated from the earth's crust, and exists in the atmosphere attached to aerosol particles. The majority of atmospheric ^{210}Pb concentrations observed in the ground level ranges from one to several mBq/m³. As the ^{210}Pb which is one of the natural radionuclide of the ^{238}U decay series is widely used as a tracer. ^{222}Rn (half-life 3.8 d), noble gas of the ^{238}U decay series, easily diffuses out mainly from land surface to the atmosphere via a series of short-lives secondary nuclides and becomes irreversibly attached to submicron-sized aerosols and are removed both by washout and by dry deposition. ^{210}Pb depositional pattern gave us information on continental aerosols in lower troposphere [26]. Particles that sink and accumulate in the bottom of aquatic systems scavenge the ^{210}Pb present in the water column due to the decay of ^{222}Rn in the atmosphere and ulterior dry and

wet deposition and in the water. This is known as “excess ^{210}Pb ” ($^{210}\text{Pb}_{\text{xs}}$) and is added to the “supported ^{210}Pb ” ($^{210}\text{Pb}_{\text{sup}}$), which is continuously produced by the in situ decay of ^{226}Ra in bottom sediments. The accumulation of sediments over time ideally generates a decreasing distribution of ^{210}Pb specific activity as a function of depth (or cumulative mass in g/cm^2) governed by the decay of the $^{210}\text{Pb}_{\text{xs}}$, as illustrated in **Fig. 1.7** [26].

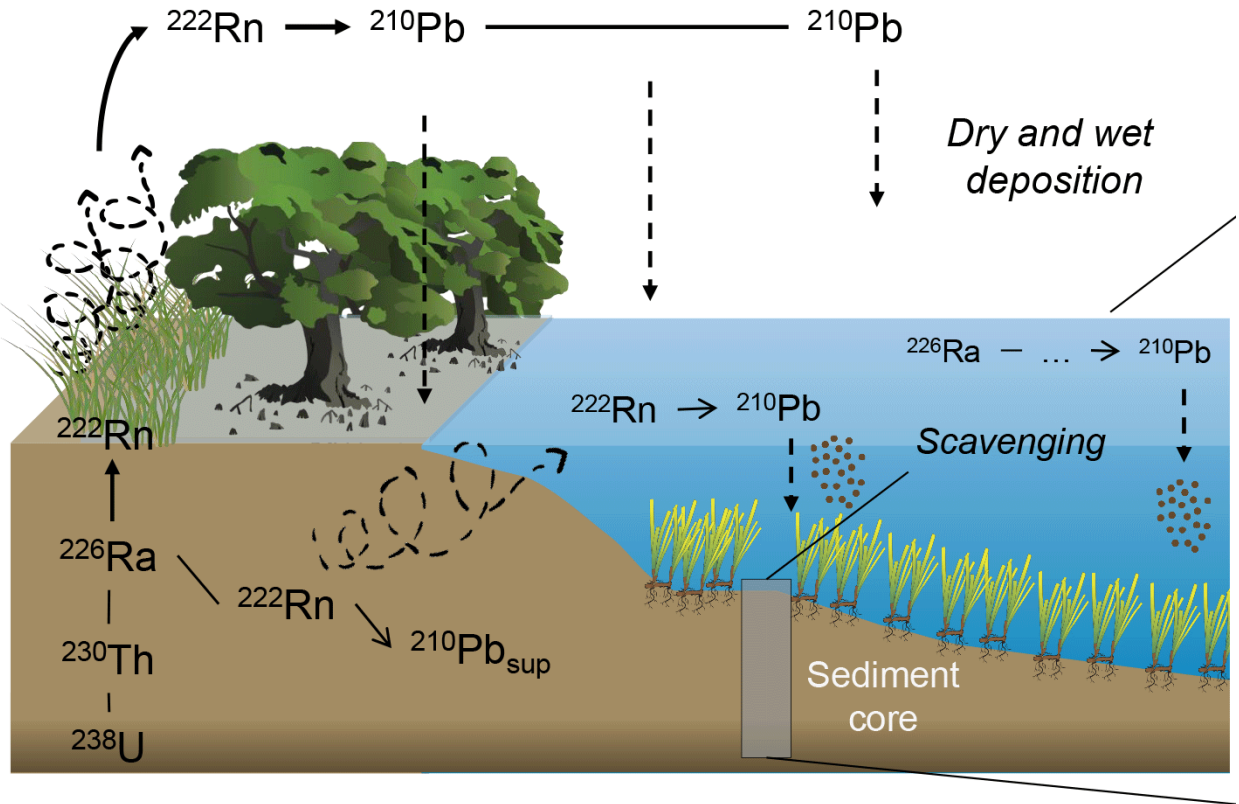


Fig. 1.7 ^{210}Pb cycle and idealized ^{210}Pb specific activity profile in environment [26].

The atmospheric ^{210}Pb is essentially the crust on the earth surface, the atmospheric concentration of ^{210}Pb over the continental areas is generally higher than that over the oceanic ones, [28] and can reflect the geological and meteorological background of the observed localities. ^{210}Pb released from the sources and stored in environmental repositories can be a potential source

for secondary pollution. ^{210}Pb has also been used for studying plant uptake of ^{210}Pb though the methodology that is based on artificially spiking the soils with ^{210}Pb and monitoring its subsequent concentrations in the plants and soils [29]. ^{210}Pb disintegrates by beta minus emission to the excited level and emits gamma energy at 46.6 keV (4.25 %) to the ground state level of ^{210}Bi . Its decay scheme shows in **Fig. 1.8**.

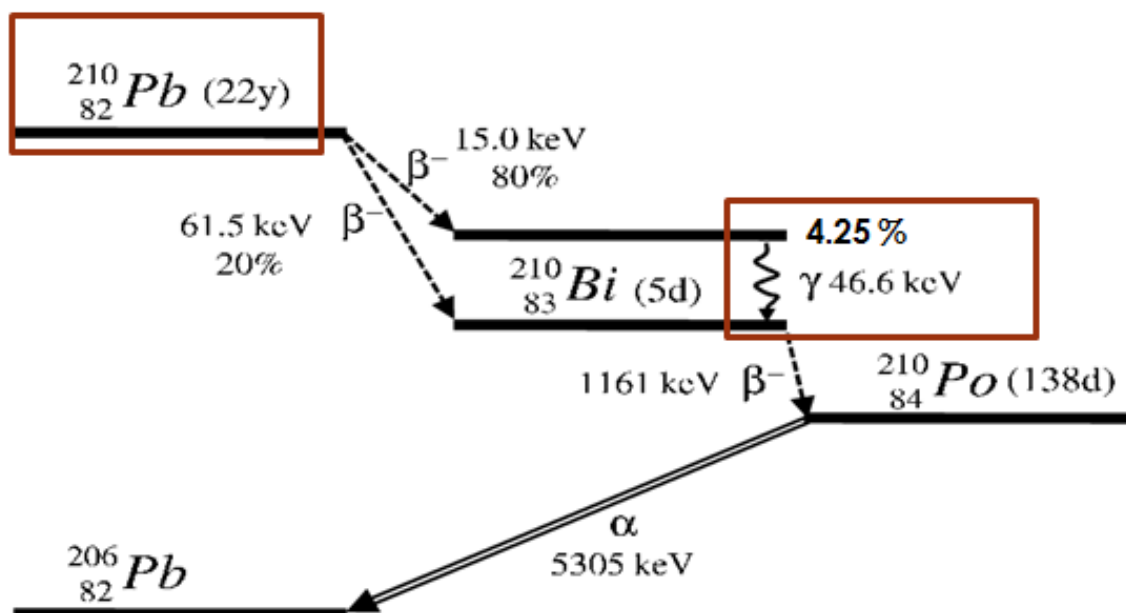


Fig. 1.8 Decay scheme of ^{210}Pb [26].

1.5 Surface air concentrations of ^7Be and ^{210}Pb

1.5.1 Surface air concentrations of ^7Be

Surface air ^7Be concentrations have been measured by a number of investigators at different locations worldwide and over different time periods. **Table 1.4** shows summaries a number of recent and historical studies. The data from the **Table 1.4** was plot in **Fig. 1.9** show low average concentrations are reported at near equator and high latitude sites, as well as at sites in the Pacific

under the intertropical convergence zone. The average concentration of this study compared with other reports at a different latitude. Our results can be comparable at the similar latitude. Higher average concentrations generally occur at middle latitudes of the Northern Hemisphere. The seasonal variations showed the effects of at least four factors: (1) stratosphere-to-troposphere exchange (STE); (2) vertical mixing within the troposphere; (3) air mass transport from middle to high latitudes; and (4) rainfall. STE is a means for highly concentrated ^7Be air from the stratosphere to enter the troposphere and is generally most intense at middle latitudes during the spring season. [30, 31, 32] reported maximum average concentrations of ^7Be in surface air to be around 1.6 times higher than minimum average concentrations over a complete sunspot cycle at Munich-Neuherberg (Germany) and Osaka (Japan), respectively. Vertical mixing of air within the troposphere can occur through convective circulation. Solar heating of earth's surface in the warmer months leads to an increase in temperature of the surface air. Cooler air sinks and displaces the warm surface air, bringing with it higher concentrations of ^7Be from the upper troposphere [30] found the effects of STE and vertical mixing within the troposphere on seasonal variations of ^7Be in surface air to be evident at middle latitudes, where surface air concentrations of this radionuclide typically show a spring- summer peak and an autumn-winter trough. Other investigators have also attributed the observed seasonality at middle latitude sites to a combination of these two factors [33, 34, 35]. A distinct peak in surface air ^7Be concentrations at Antarctica is reported to occur in the austral summer [30, 37] found that variations in ^7Be concentration at the South Pole paralleled the variations in aerosol concentration with a presumed middle latitude source. Such air mass transport within the troposphere from middle to high latitudes is possible through the polar cell of global circulation. Washout by rainfall strips the troposphere of ^7Be -bearing aerosols, decreasing the concentration of this radionuclide in the surface air. Negative correlations between surface air ^7Be concentrations and rainfall were reported by [30] for sites where a strong seasonal variation in

the rainfall was observed. Overall, the timing and magnitude of seasonal variations in surface air ^7Be concentrations can change with geographical location depending on the contribution from the individual factors that cause these variations. The solar modulation of cosmic-ray fluxes also causes low frequency variations in the concentration of ^7Be in surface air. These variations are noticeable in measurements made over extended periods and show an anti-correlation with sunspot number [32, 35, 39] reported maximum average concentrations of ^7Be in surface air to be around 1.6 times higher than minimum average concentrations over a complete sunspot cycle at Munich Neuherberg (Germany) and Osaka (Japan), respectively. They used a Fourier transform analysis to identify patterns of significant temporal variability in surface air ^7Be concentration measurements of the EML. They found that the amplitude of solar variations differed between different locations, with no apparent latitude or altitude trends. Also, highest concentrations of ^7Be in surface air at the South Pole occurred along the descending branch of the sunspot maximum, which they suggested may be the result of low-energy solar particles being able to penetrate the weaker strength magnetic field above the Poles. Synoptic-scale variations in surface air ^7Be concentrations have been investigated by Zanis et al. (1999) and Gerasopoulos et al. (2001) [40] at a number of alpine stations. They found episodes of high ^7Be concentration to be associated with upper-level ridges and episodes of low ^7Be concentration to be associated with upper-level troughs. Downward air mass transport from the upper troposphere under anti-cyclonic conditions (upper-level ridge) and wet scavenging of ^7Be -bearing aerosols under the influence of an upper-level trough were reported by these authors to be the main processes controlling short-term (day-to-day) variations in surface air ^7Be concentrations. suggested that high weekly ^7Be concentrations in the surface air at Tokyo (Japan) may be the result of downward air mass transport in the troposphere caused by travelling anticyclones formed between the ridge and trough of the Rossby waves (large-scale meanders of the jet stream).

In Japan, many studies have reported the ^7Be concentration in surface air (shown in **Table 1.4**). Most of these have been done in the districts facing the Pacific Ocean area, and similar results were obtained that indicated a seasonal variation having two peaks with a spring-autumn maximum and summer minimum, such as in Osaka, Chiba, and Tsukuba. Because in the summer, the wind blows and transporting air masses from low latitudes and it is well known that the air mass from low latitudes carries low concentration of cosmogenic radionuclides [41]. Such as a seasonal pattern of Japan is different from a seasonal pattern of Europe and the European part of Russia, the maximal concentration is measured in spring and summer due to stronger vertical mixing of tropospheric and stratospheric air, which is typical for mid-latitudes in those seasons [42]. The temporal variations in the surface ^7Be and ^{210}Pb concentration depend on the season, location, and local meteorological conditions. Several simulations were carried out in order to provide an explanation of the measured temporal variations based on the transport models [20] The Hybrid Single-Particle Lagrangian Integrated Trajectory (HYSPLIT) model is a tool that helps to explain how, when, and where air masses are atmospherically transported. This model is a useful approach to the computing of the air masses transport associated with ^7Be concentration recorded in the area of the study.

Table 1.4 Average surface air concentrations of ^7Be at different locations in the world. Reviewed by Che Doering (2007).

Location	Latitude	^7Be (mBq/m ³)	Period	Reference
Alert, Canada	82°N	1.9	1990 ~ 1992	[43]
Sodankylä, Finland	67°N	2.5	1995 ~ 1997	[44]
Grindsjön, Sweden	59°N	2.3	1972 ~ 2000	[45]
Edinburgh, United Kingdom	56°N	2.5	2002 ~ 2003	[46]
Roskilde, Denmark	55°N	1	1990 ~ 1993	[47]
Vilnius, Lithuania	54°N	3.1	1965 ~ 1969	[48]
Quillayute WA, United States	48°N	4.2	1976 ~ 1977	[49]
Bratislava, Slovakia	48°N	3.1	1978 ~ 1994	[34]
Munich, Germany	48°N	3.6	1983 ~ 1985	[31]
Zugspitze, Germany	47°N	4.6	1996 ~ 1998	[40]
Sonnblick, Austria	47°N	5.3	1996 ~ 1998	[40]
Jungfrauoch, Switzerland	46°N	7	1996 ~ 1999	[40]
Belgrade, Serbia- Montenegro	44°N	4	1991 ~ 1996	[50]
Mt. Cimone, Italy	44°N	5.7	1996 ~ 1999	[40]
Thessaloniki, Greece	40°N	5	1987 ~ 2001	[51]
Palermo, Italy	38°N	5.1	1982 ~ 2002	[40]
Granada, Spain	37°N	4.5	1993 ~ 2001	[33]
Malaga, Spain	36°N	4.6	1996 ~ 2001	[52]
Osaka, Japan	34°N	6.7	1983 ~ 1997	[32]
Osaka, Japan	34.71°N	5.04	2018 ~ 2020	<u>This study</u>
Kuwait City, Kuwait	29°N	5.2	1994 ~ 1998	[53]
El-Minia, Egypt	28°N	2	1998 ~ 1999	[54]

Location	Latitude	^7Be (mBq/m ³)	Period	Reference
Midway, North Pacific	28°N	2.9	1985	[55]
Cienfuegos, Cuba	22°N	4.1	1994 ~ 1998	[33]
Oahu HI, United States	21°N	3.1	1985	[55]
Enewetak, North Pacific	11°N	1.7	1985	[55]
Nauru, South Pacific	1°S	1.4	1985	[55]
Funafuti, South Pacific	9°S	1.6	1985	[55]
Samoa, South Pacific	14°S	2.3	1985	[55]
Fiji, South Pacific	18°S	1.6	1999 ~ 2000	[55]
Rarotonga, South Pacific	21°S	3	1985	[55]
New Caledonia, South Pacific	22°S	3.1	1985	[55]
Norfolk Island, South Pacific	29°S	2.7	1985	[55]

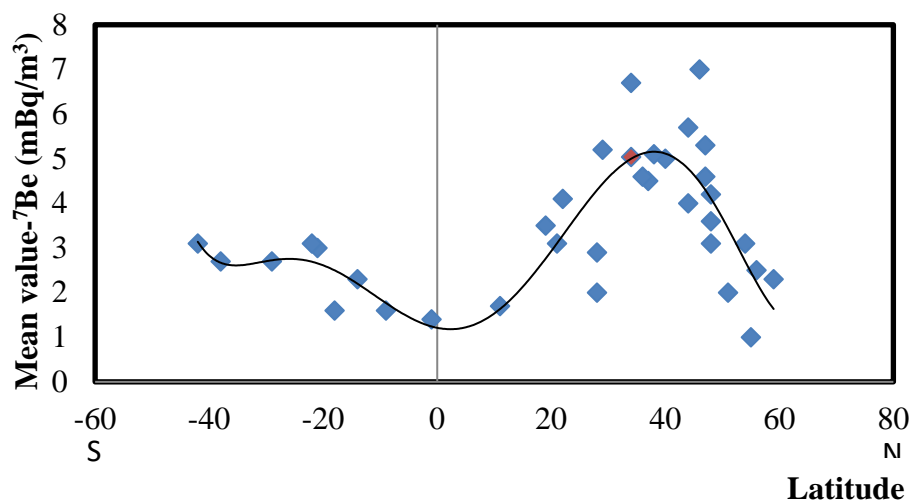


Fig. 1.9 The relationship between the mean value of ^7Be concentration and latitude. The mean of ^7Be concentration of this study shows in red square.

1.5.2 Surface air concentrations of ^{210}Pb

Surface air ^{210}Pb concentrations have been measured by a number of investigators at different locations worldwide and over different time periods. N. Preis, (1996) reported the latitudinal distribution of concentration in surface-air; it includes both the measurements over continents and oceans. In **Fig. 1.10**, when various measures have been made simultaneously, the values have been averaged and represented by a single value and our result can be comparable. **Fig. 1.11** gives the 10°S the zonal average for continents only, as oceanic measurements were not included because of the scarcity of data. It is important to remember that is solely based on published measurements and do not have some large continental areas such as Africa, Asia (except India), and the eastern part of South America. The latitudinal distribution clearly expresses the difference between the northern and southern hemispheres. Concentrations are in general higher in the northern than in the southern hemispheres, a consequence of the high asymmetry in the continent/ocean ratio and therefore in the ^{210}Pb sources. The continental sources' effect is well illustrated by the dramatic change in the latitudinal distribution of concentration at 40°S , a latitude south of which no continental source exists. A considerable asymmetry can be noted between northern and southern Polar Regions. As already discussed, the lack of continental sources south of 45°S together with the strong circumpolar circulation, leads to extremely low ^{210}Pb content in Antarctica were observed. This is a good illustration of the extent to which the Antarctic continent is isolated from the other continents' influence. [56].

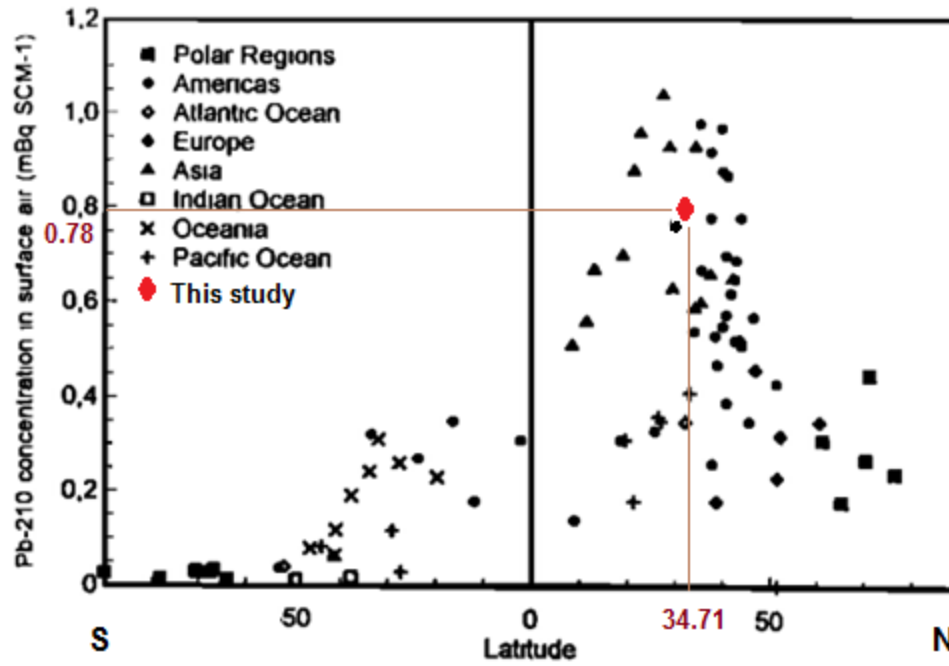


Fig. 1.10 Mean annual ^{210}Pb concentration in surface air as a function of latitude [56].

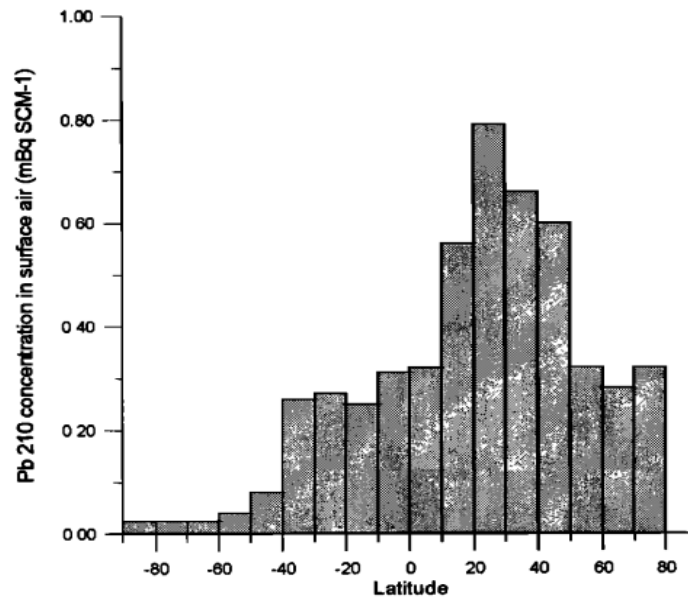


Fig. 1.11 Mean annual ^{210}Pb concentration in surface air as a function of latitude on continents only [56].

1.6 Air pollution

Air pollution is a mix of hazardous substances from both human-made and natural sources. Some dangerous substances are released into the air naturally, such as ash and gases from volcanic eruptions. Other emissions can be caused by both human and natural activity, such as smoke from wildfires, which people often start, and methane, which comes from decomposing organic matter in soils as well as animal feedlots. The primary sources of human-made air pollution are vehicle exhaust; fuel oils, and natural gas to heat homes; by-products of manufacturing and power generation, particularly coal-fueled power plants; and fumes from chemical production [57].

1.6.1 Particulate matter (PM)

Particulate matter (PM), also called particle pollution, is a general term for extremely small particles and liquid droplets in the atmosphere [57]. It made of chemicals such as sulfates, nitrates, carbon, or mineral dusts, are created during the combustion of fossil fuels and organic matter [58]. Source of PM was classified into two source based on the origin of PM: 1) primary sources: passed from the source directly into the environment such as metals, insoluble minerals, ammonium, and sea salt and 2) secondary sources made from reactions between primary pollutants and environmental constituents such as sulfates and nitrates [59]. This study focused on nitrate (NO_3^-), ammonium (NH_4^+), and sulfate (SO_4^{2-}) are significant constituents of the inorganic PM, and sea salt, the relatively large particle sizes reflecting the proximity of the measurement site to the ocean. PM should be considered to consist of two separate classes of pollutants, fine particles and coarse particles. Fine and coarse particles differ in sources, formation mechanisms, composition, atmospheric lifetimes, spatial distribution, indoor-outdoor ratios, and temporal variability, as well as size [60]. **Fig. 1.12** shows the sizes and composition of PM. Atmospheric aerosol size

distribution has 2 main classes with the particle sizes ranging from 0.005 to 2 μm for fine particles and greater than 2 μm for coarse particles. The fine particle includes 2 size ranges: 1) Aitken nuclei, having sizes ranging from 0.005 to 0.05 and 2) accumulation particles having sizes ranging from 0.05 to 2 μm . [61]. **Fig. 1.13** shows the size distribution of PM. Total suspended particulate matter (TSP) is defined by the design of the High Volume Sampler (HiVol), which collects all of the fine particles but only part of the coarse particles. The upper cut-off size of the HiVol is undefined, except by the design of the sampler, and varies with wind speed and direction. Extraordinary measures, such as were undertaken with the Wide Area Aerosol Classifier (WRAC), are required to collect the entire coarse mode. PM_{2.5} is only an approximation of fine-mode particles, and PM(2.5 ~ 10) is only an approximation of thoracic coarse-mode particles [60].

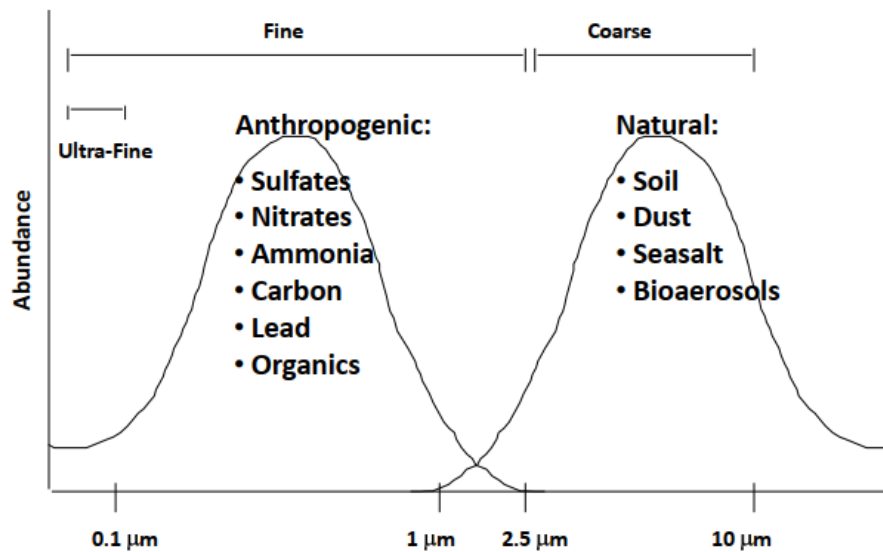


Fig. 1.12 Sizes and Composition of Particulate Matter [58].

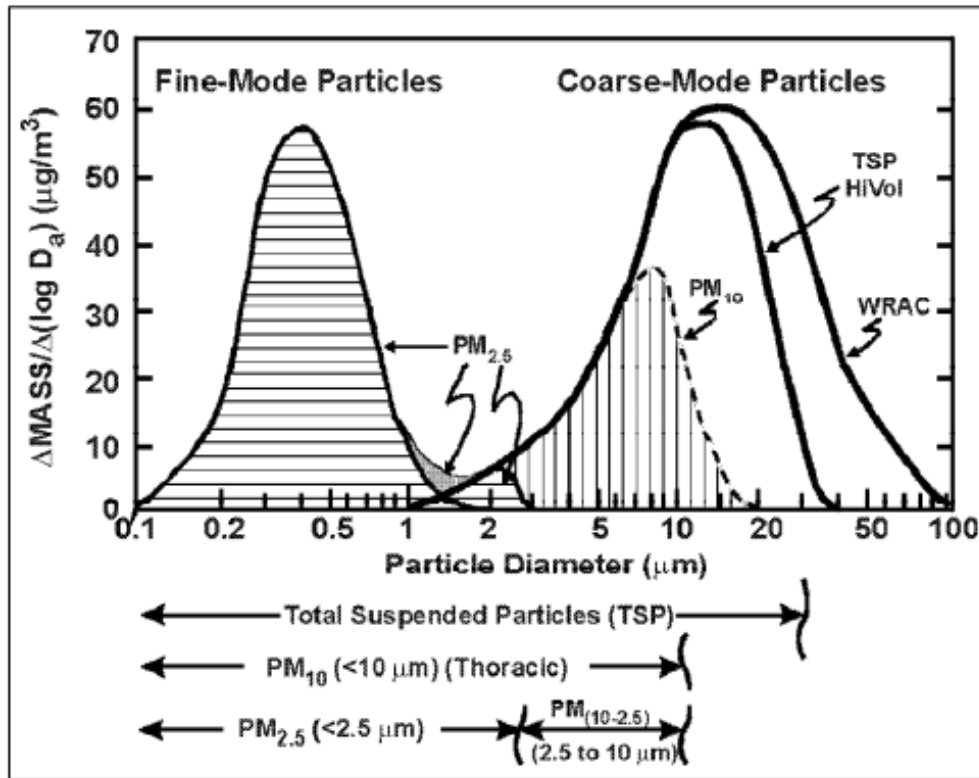


Fig. 1.13 An idealized size distribution of ambient particulate matter showing fine and coarse modes and the portions collected in various samples [60].

1.6.2 Aerosol transportation and global circulation patterns

In general, the long-range transported components are carried at lower free atmosphere (approximately over 1500 m), and the study of air motion in the atmospheric boundary layer, which is the seat of atmospheric turbulence that strongly influence the meteorology and dispersion (approximately lower 1500 m) [62, 63].

Fig. 1.14 shows the global circulation patterns. Over the major parts of the Earth's surface there are large-scale wind circulations present. The global circulation can be described as the world-wide system of winds by which the necessary transport of heat from tropical to polar

latitudes is accomplished. In each hemisphere there are three cells (Hadley cell, Ferrel cell and Polar cell) in which air circulates through the entire depth of the troposphere. The largest cells extend from the equator to between 30 and 40 degrees north and south, and are named Hadley cells, after English meteorologist George Hadley. In the middle cells, which are known as the Ferrel cells, air converges at low altitudes to ascend along the boundaries between cool polar air and the warm subtropical air that generally occurs between 60 and 70 degrees north and south. This often occurs around the latitude of the UK which gives us our unsettled weather. The circulation within the Ferrel cell is complicated by a return flow of air at high altitudes towards the tropics, where it joins sinking air from the Hadley cell. The smallest and weakest cells are the Polar cells, which extend from between 60 and 70 degrees north and south, to the poles. Air in these cells sinks over the highest latitudes and flows out towards the lower latitudes at the surface [64].

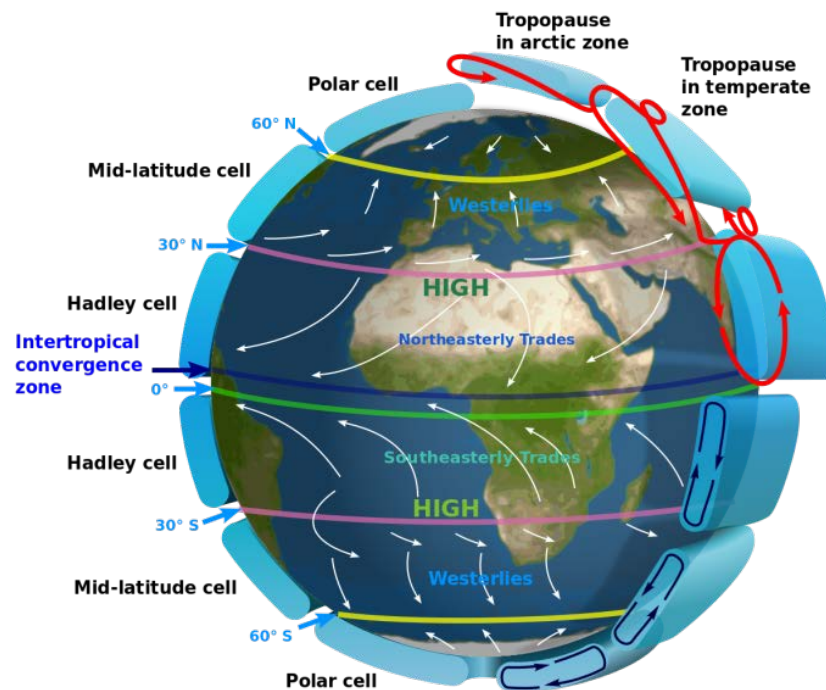


Fig. 1.14 Idealised depiction of large-scale atmospheric circulation on Earth [64].

1.7 Deposition of ^7Be and ^{210}Pb

1.7.1 Deposition of ^7Be

^7Be -bearing aerosols can reach the ground under clear sky conditions through particle sedimentation (dry deposition), but are removed more efficiently from the troposphere by precipitation scavenging (wet deposition). Experimental measurements show that around 90 % or more of total ^7Be deposition in temperate zones generally takes place through the wet deposition process [65]. Wet deposition of ^7Be occurs through both below-cloud scavenging (washout) and in-cloud scavenging (rainout) of its carrier aerosol during a precipitation event. Washout occurs during the early stages and quickly cleanses the lower troposphere of ^7Be -bearing aerosols. Rainout delivers ^7Be from within the cloud layer to Earth's surface and is active throughout the duration of a precipitation event. Serial sampling within individual storms shows the specific activity of ^7Be in precipitation to decrease sharply during the initial stages and then remains fairly constant throughout the mid-to-latter stages, reflecting a change from washout to rainout as the predominant wet deposition process [35].

Annual deposition of ^7Be worldwide ranges from around 400 to 6500 Bq/m² and appears to be dependent upon rainfall. Low annual depositions of this radionuclide have been reported for sites in the Middle East and Mediterranean regions, as well as at East Antarctica. The highest annual deposition of ^7Be to be reported (6350 Bq/m²) is for a high rainfall area on the South Island of New Zealand. Young and Silker (1980) reported an average ^7Be flux across the surface of the North Pacific and North Atlantic oceans of 270 atoms/m²/s, which corresponds to an annual deposition of approximately 1290 Bq/m². Zonal annual average ^7Be deposition has been simulated in a global climate model by Brost et al. (1991) [51]. They found deposition minima to occur in

relatively dry regions such as at high latitudes, across the deserts of northern Africa and the Middle East, and under the subtropical high pressure systems off the west coasts of the Americas, Africa and Australia. Deposition maxima were found to occur in regions of relatively high precipitation such as at middle latitudes and under the intertropical convergence zone, as well as over the oceans.

^7Be depositional fluxes (i.e. activity deposited per unit area per unit time) at different locations show a high positive correlation with rainfall, and temporal variations in the depositional flux of this radionuclide generally follow the local rainfall pattern [67]. Seasonal changes in the ^7Be budget of the troposphere may also influence the depositional flux of this radionuclide. Dibb (1989) [68] reported the bulk of ^7Be deposition during 1986 and 1987 at Solomons MD (United States) to occur during spring and early summer. This was in spite of near-drought conditions in the spring of 1986. He found the timing of the observed peak in ^7Be deposition to be in close agreement with estimates of the seasonal injection of ^7Be rich stratospheric air into the troposphere due to STE and concluded that the ^7Be depositional flux closely reflected the tropospheric inventory of this radionuclide. Investigators working at other sites across the eastern United States have also reported springtime maxima in ^7Be depositional fluxes [69]. A pronounced winter peak in the depositional flux of ^7Be has been observed at a number of sites in Japan located along the coast of the Japan Sea [70]. Yamamoto et al. (2006) [26] suggested that the flow of cold air masses containing high ^7Be concentration from high latitudes, mixing and generation of convection clouds over the Sea of Japan, and accompanying heavy winter snowfalls were responsible for this observation. The deposition velocity of ^7Be -bearing aerosols can be calculated from the ratio of the ^7Be depositional flux to its concentration in surface air. Average deposition velocities of this radionuclide at different locations, including over the Pacific and Atlantic oceans,

are reported to be in the range from 0.004 to 0.074 m/s [49]. Since certain artificial radionuclides (e.g. strontium-90 and caesium-137) are also found attached predominantly to submicron-sized aerosols and are present mainly in the stratosphere, the deposition velocity of ^7Be may be a useful parameter in estimating the long-term deposition of radioactive pollutants from remote sources [71]. This may be especially applicable to Australia and the South Pacific region, where the distance from major nuclear installations means that any radioactive pollution is likely to be mixed throughout the troposphere after it descends from the stratosphere.

In Japan, NARAZAKI, et.al, 2009 [70] study ^7Be deposition in different locations in Japan, it is reported that the maximum in winter in Japan Sea side, and in spring in Pacific Ocean side. ^7Be , stratospheric fallout, also receives local influence, and its seasonal variation can be classified into four (spring peak, double peaks, winter peak and non-peak) patterns (**Fig. 1.15**). At the spring peak and double peaks their ^7Be deposition in spring increases. And due to leak through gap in tropopause or mean meridional circulation, atmospheric ^7Be concentration increases in this period. However, ^7Be deposition in spring has got low correlation with rain amount and ^7Be concentration in rain, but stagnation in rainy season promotes washout increase of the ^7Be . At the spring peak and double peaks their ^7Be deposition in spring increases. And due to leak through gap in tropopause or mean meridional circulation, atmospheric ^7Be concentration increases in this period. However, ^7Be deposition in spring has got low correlation with rain amount and ^7Be concentration in rain, but stagnation in rainy season promotes washout increase of the ^7Be . Areas, where ^7Be deposition becomes maximum in spring, can be classified into two groups; one has peak only in spring, and the other has double peaks also in September. The former distributes in West Japan, and the latter in East Japan (**Fig. 1.16**). In September, when pressure direction turns to reverse, north-eastern air current becomes easy to enter, and autumnal rain front also stagnates in south-eastern Sea of Japan, which brings lots of rain in the

Pacific Ocean side of East Japan. This local increase of rain brings large ^7Be deposition in September, which results in double peaks there. Winter peak, at which ^7Be deposition eminently increases, is considered due to rainout by rain and is distributed in Japan Sea side such as Hokuriku district. No large seasonal variation is shown throughout a year in areas of stable atmosphere, sandwiched by Backbone Mountains running north south direction, and of a little rain (Non-peak). In August, when Pacific oceanic high air pressure, stagnating in South Ocean, covers all Japan, atmospheric ^7Be concentration and rain amount are relatively low, and then ^7Be deposition becomes minimized throughout a year all over Japan.

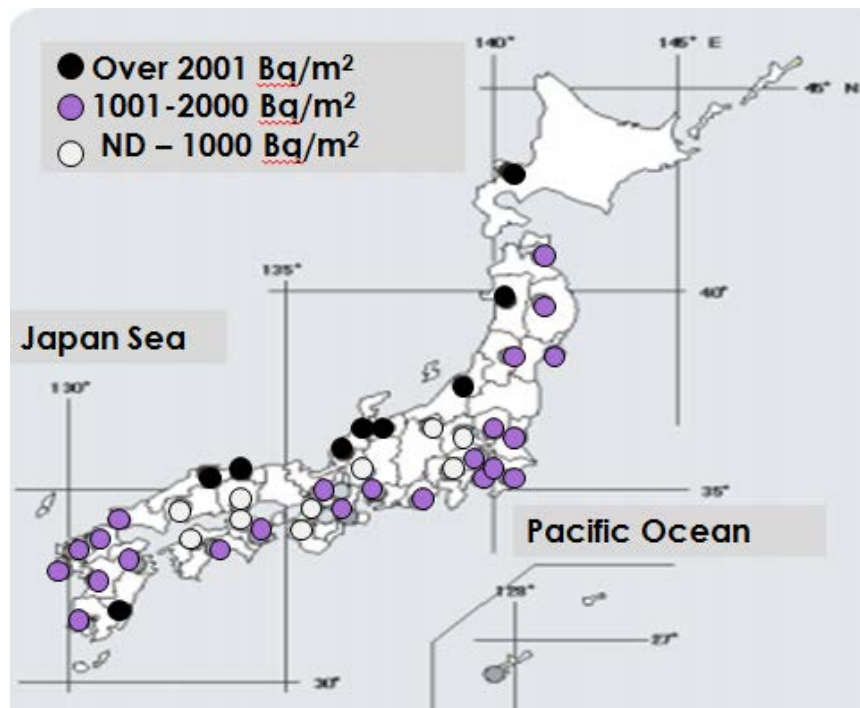


Fig. 1.15 Annual deposition of ^7Be in Japan [70].

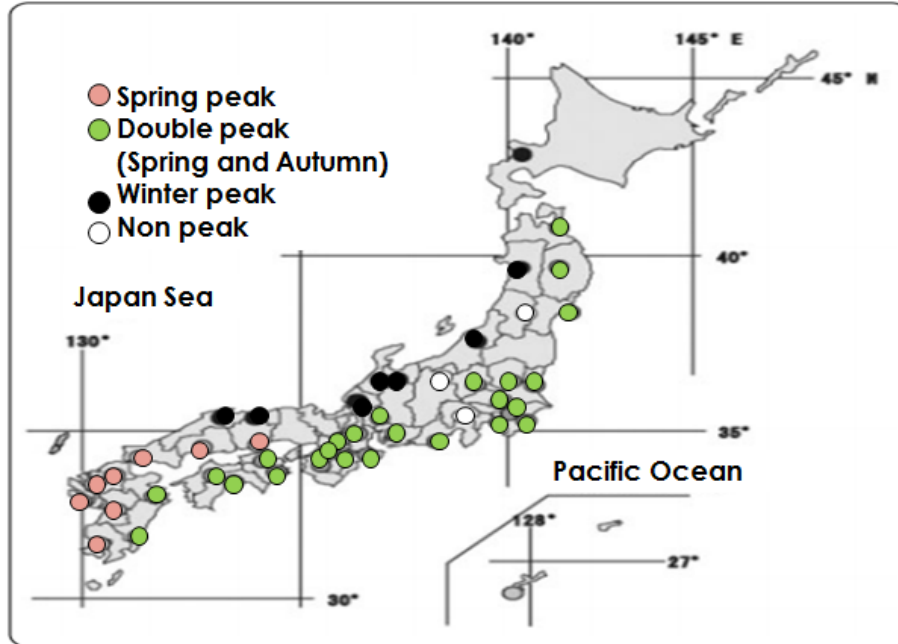


Fig. 1.16 Variation patterns for monthly deposition of ^7Be in Japan [70].

1.7.2 Deposition of ^{210}Pb

^{210}Pb deposition have been measured by a number of investigators at different locations worldwide and over different time periods reported the ^{210}Pb deposition flux data are expressed as a function of latitude and our data can be comparable in **Fig. 1.17**. It is important to remember that this latitudinal distribution results from the existing data and that large parts of continents such as South America, Africa, and Central Asia are not represented because of the lack of measurement. Distribution is similar to the latitudinal distribution of ^{210}Pb concentration in the air. The difference between the northern and southern hemispheres appears clearly, resulting from the same causes (high asymmetry in the ratio of continent/ocean surfaces). Nevertheless, some differences can be pointed out: (1) a much greater dispersion, particularly for the northern mid-latitudes, and (2) the polar zones in both hemispheres (Greenland and Antarctica) present values of the same order of

magnitude, whereas the concentration in air, is much higher in the Arctic regions than in Antarctica [56].

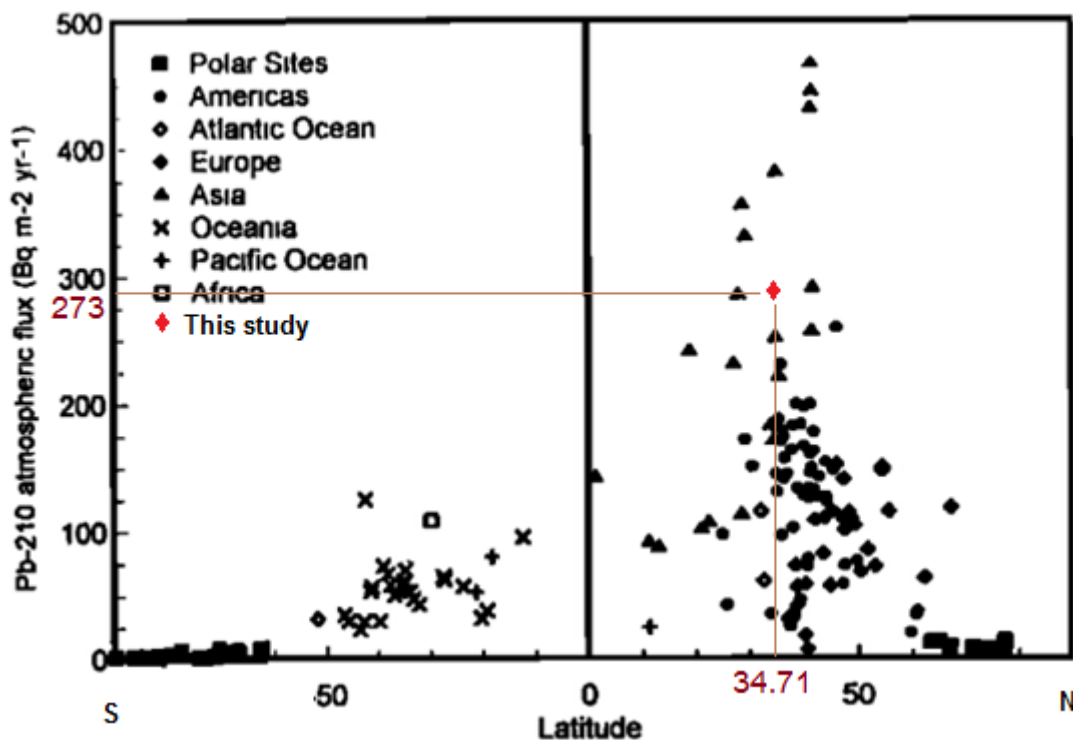


Fig. 1.17 Annual ^{210}Pb atmospheric deposition flux from the artificial collector, snow, and soil measurements as latitude function [56].

1.8 Environmental applications

^7Be is a useful radionuclide for studying atmospheric transport processes for several reasons: (1) its source is known and global in extent; (2) it has a relatively short half-life; (3) it attaches rapidly and indiscriminately to available aerosols; (4) it has a steep concentration gradient between the lower stratosphere and the surface air; (5) it is relatively simple and inexpensive to measure; and (6) there is a large amount of reliable data available for hypothesis testing. ^7Be measurements have been used by a number of investigators to test and validate the results of general circulation models of the atmosphere [72]. The potential for using ^7Be to study atmospheric

transport processes is particularly great when it is coupled with a nuclide with a contrasting source function and/or a different half-life. Raisbeck et al. (1981) and Jordan et al. (2003) demonstrated that the ratio of beryllium-10 (^{10}Be) to ^7Be can be used as a probe of atmospheric transport processes, in particular Solar-Terrestrial Environment (STE).

^7Be may be used in conjunction with lead-210 (^{210}Pb) to determine whether the source of a scavenged air mass is oceanic versus continental and/or upper versus lower tropospheric [73]. ^{210}Pb is a decay product of gaseous radon-222, which emanates primarily from the surface of continental land masses. Production rates of ^7Be in the atmosphere increase with altitude and are independent of geography. Both radionuclides attach primarily to submicron-sized aerosols and are removed from the atmosphere through similar processes.

References

- [1] Bertil R.R. Persson, and Elis Holm, 2014, ^7Be , ^{210}Pb , and ^{210}Po in the surface air from the Arctic to Antarctica, Journal of Environmental Radioactivity xxx, 1-11.
- [2] Andrey S. Neroda et al., 2016, Long-range atmospheric transport Beryllium-7 to region the Sea of Japan, Journal of Environmental Radioactivity, 160, 102.
- [3] C. Duenas et al., 2015, Study of the cosmogenic factors influence on temporal variation of ^7Be air concentration during the 23rd solar cycle in Malaga (South Spain), J Radioanal Nucl Chem, 303, 2151.
- [4] J.H. Chao et al., 2014, Monitoring of ^7Be in surface air of varying PM10 concentrations, Applied Radiation and Isotopes, 89, 95.
- [5] P Noithong, A Rittirong, and R Hazama, 2019, Study of the factors influence on variation of Be-7 concentration in surface air at Osaka, Japan, IOP Conf. Series: Journal of Physics, 1285.

- [6] M. A. Leiva G., R. Toro, R. G. E. Morales, M. A. Ríos, and M. R. Gonzalez, 2014, A study of water-soluble inorganic ions in size-segregated aerosols in atmospheric pollution episode, *Int. J. Environ. Sci. Technol.*, 11, 437.
- [7] David A. Atwood, 2010, *Radionuclides in the Environment*, University of Kentucky, Lexington, KY, USA.
- [8] National Council on Radiation Protection and Measurements, 1987, *Exposure of the Population in the United States and Canada from Natural Background Radiation*; NCRP-94; Bethesda, MD (USA), 217.
- [9] J. N. Goswami, R. E. McGuire, R. C. Reedy, D. Lal, and R. Jha, 1988, Solar flare protons and alpha particles during the last three solar, cycles *J. Geophys. Res.-Space Phys.*, 93(A7), 7195.
- [10] D. Lal and B. Peters, 1967, Cosmic Ray Produced Radioactivity on the Earth, in *'Encyclopaedia of Physics'*, ed. Flugge, S., Springer Verlag, Berlin, 551.
- [11] D. Lal, Annu, 1988, *Seismic Stratigraphy*, *Rev. Earth Planet. Sci.*, 16, 355.
- [12] United Nations Scientific Committee on the Effect of Atomic Radiation, 1988, *'Sources, Effects and Risks of Ionizing Radiation'*, United Nations Scientific Committee on the Effect of Atomic Radiation, New York,
- [13] K. Rozanski, Mesoscale, 1979, transport of ^{85}Kr originating from European sources, *'Environ. Int.*, 2(3), 139
- [14] D. Lal and B. Peters, 1967, Cosmic Ray Produced Radioactivity on the Earth, in *'Encyclopaedia of Physics'*, ed. Flugge, S., SpringerVerlag, Berlin, 551.
- [15] Michael F. L'Annunziata, 2007, *Radioactivity Introduction and History, From the Quantum to Quarks*, 2ed The Boulevard, Langford Lane, Kidlington, Oxford OX5 1GB, UK
- [16] T F Gesell, H M Prichard, 1975, The technologically enhanced natural radiation environment, *J. Health Phys.*, 28(4).
- [17] Pittauerová, Daniela; Kolb, William M.; Rosenstiel, Jon C.; Fischer, Helmut W., 2014, *Radioactivity in Trinitite - a review and new measurements*, *Radiation in the environment – Poster presentations*,
- [18] Koch, D.M., Jacob, D.J., Graustein, W.C., 1996, Vertical transport of tropospheric aerosols as indicated by ^7Be and ^{210}Pb in a chemical tracer model. *Journal of Geophysical Research* 101(D13), 18651–18666.
- [19] Rehfeld, S., Heimann, M., 1995, Three dimensional atmospheric transport simulation of the radioactive tracers

- ^{210}Pb , ^7Be , ^{10}Be , and ^{90}Sr . *Journal of Geophysical Research* 100(D12), 26141–26161.
- [20] F. Piñero García et al., 2012, ^7Be behaviour in the atmosphere of the city of Granada January 2005 to December 2009, *Atmospheric Environment*, 47, 84.
- [21] C. Papastefanou, and A. Ioannidou, 1995, Aerodynamic size association of ^7Be in ambient aerosols, *Journal of Environmental Radioactivity*, 26(3), 273–282.
- [22] Ioannidou, A., Papastefanou, C., 2006, Precipitation scavenging of ^7Be and ^{137}Cs radionuclides in air. *Journal of Environmental Radioactivity* 85, 121–136.
- [23] Andrey S. Neroda, Anna A. Goncharova, Vladimir A. Goryachev, Vasily F. Mishukov, Natalia V. Shlyk, 2016, Long-range atmospheric transport Beryllium-7 to region the Sea of Japan, *Journal of Environmental Radioactivity* 160, 102–111.
- [24] Hötzl, H., Rosner, G., Winkler, R., 1991, Correlation of ^7Be concentrations in surface air and precipitation with the solar cycle. *Naturwissenschaften* 78, 215–217.
- [25] C.M. Lederer, V.S. Shirley, 1978, *Table of Isotopes*, Wiley, New York.
- [26] M. Yamamoto, H. Kofugi, K. Shiraishi, and Y. Igarashi, 1998, An attempt to evaluate dry deposition velocity of airborne Pb-210 in a forest ecosystem, *Journal of Radioanalytical and Nuclear Chemistry*, 227, 81–87.
- [27] Ariane Arias-Ortiz, Pere Masqué, Jordi Garcia-Orellana, Oscar Serrano, Inés Mazarrasa, Núria Marbà, Catherine E. Lovelock, Paul S. Lavery, and Carlos M. Duarte, 2018, Reviews and syntheses: ^{210}Pb -derived sediment and carbon accumulation rates in vegetated coastal ecosystems – setting the record straight, *Biogeosciences*, 15, 6791–6818.
- [28] S. Sato, Y. Koike, T. Saito, and J. Sato, 2003, Atmospheric concentration of ^{210}Pb and ^7Be at Sarufutsu, Hokkaido, Japan, *Journal of Radioanalytical and Nuclear Chemistry*, 255(2) 351–353.
- [29] Handong Yang, and Peter G. Appleby, 2016, Use of lead-210 as a novel tracer for lead (Pb) sources in plants, *Scientific Reports* | 6:21707 | DOI: 10.1038/srep21707.
- [30] Feely, H.W., Larsen, R.J., Sanderson, C.G., 1989, Factors that cause seasonal variations in beryllium-7 concentrations in surface air. *Journal of Environmental Radioactivity* 9, 223–249.
- [31] Hötzl, H., Winkler, R., 1987, Activity concentrations of ^{226}Ra , ^{228}Ra , ^{210}Pb , ^{40}K and ^7Be and their temporal variations in surface air. *Journal of Environmental Radioactivity* 5, 445–458.
- [32] Megumi, K., Matsunami, T., Ito, N., Kiyoda, S., Mizohata, A., Asano, T., 2000, Factors, especially sunspot

- number, causing variations in surface air concentrations and depositions of ^7Be in Osaka, Japan. *Geophysical Research Letters* 27(3), 361–364.
- [33] Azahra, M., Camacho-Garcia, A., Gonzalez-Gomez, C., Lopez-Peñalver, J.J., El Bardouni, T., 2003, Seasonal ^7Be concentrations in near-surface air of Granada (Spain) in the period 1993–2001, *Applied Radiation and Isotopes* 59, 159–164.
- [34] Ďurana, L., Chudý, M., Masarik, J., 1996, Investigation of ^7Be in the Bratislava atmosphere. *Journal of Radioanalytical and Nuclear Chemistry* 207(2), 345–356.
- [35] Ioannidou, A., Papastefanou, C., 2006, Precipitation scavenging of ^7Be and ^{137}Cs radionuclides in air. *Journal of Environmental Radioactivity* 85, 121–136.
- [37] Lambert, G., Ardouin, B., Sanak, J., 1990, Atmospheric transport of trace elements toward Antarctica. *Tellus* 42(B), 76–82.
- [38] Aldahan, A., Possnert, G., Vintersved, I., 2001, Atmospheric interactions at northern high latitudes from weekly Be-isotopes in surface air. *Applied Radiation and Isotopes* 54, 345–353.
- [39] Cannizzaro, F., Greco, G., Raneli, M., Spitale, M.C., Tomarchio, E., 2004, Concentration measurements of ^7Be at ground level air at Palermo, Italy—comparison with solar activity over a period of 21 years. *Journal of Environmental Radioactivity* 72, 259–271.
- [40] Gerasopoulos, E., Zerefos, C.S., Papastefanou, C., Zanis, P., O'Brien, K., 2003, Low- frequency variability of beryllium-7 surface concentrations over the Eastern Mediterranean. *Atmospheric Environment* 37, 1745–1756.
- [41] H. Muramatsu, S. Yoshizawa, T. Abe, T. Ishii, M. Wada, Y. Horiuchi, and R. Kanekatsu, 2008, Variation of ^7Be concentration in surface air at Nagano, Japan, *Journal of Radioanalytical and Nuclear Chemistry* 275(2) 299–307.
- [42] Andrey S. Neroda, Anna A. Goncharova, Vladimir A. Goryachev, Vasily F. Mishukov, Natalia V. Shlyk, 2016, Long-range atmospheric transport Beryllium-7 to region the Sea of Japan, *Journal of Environmental Radioactivity* 160, 102–111.
- [43] Dibb, J.E., Meeker, D.L., Finkel, R.C., Southon, J.R., Caffee, M.W., Barrie, L.A., 1994, Estimation of stratospheric input to the Arctic troposphere: ^7Be and ^{10}Be in aerosols at Alert, Canada. *Journal of Geophysical Research* 99(D6), 12855–12864.
- [44] Paatero, J., Hatakka, J., 2000, Source area of airborne ^7Be and ^{210}Pb measured in northern Finland. *Health Physics*

- 79(6), 691–696.
- [45] Kulan, A., 2006, Seasonal ^7Be and ^{137}Cs activities in surface air before and after the Chernobyl event. *Journal of Environmental Radioactivity* 90, 140–150.
- [46] Likuku, A.S., 2006, Factors influencing ambient concentrations of ^{210}Pb and ^7Be over the city of Edinburgh (55.9°N, 03.2°W). *Journal of Environmental Radioactivity* 87, 289–304.
- [47] Fogh, C.L., Roed, J., Andersson, K.G., 1999, Radionuclide resuspension and mixed deposition at different heights. *Journal of Environmental Radioactivity* 46, 67–75.
- [48] Luyanas, V.Y., Yasyulyonis, R.Y., Shopauskiene, D.A., Styra, B.I., 1970, Cosmogenic ^{22}Na , ^7Be , ^{32}P , and ^{33}P in atmospheric dynamics research. *Journal of Geophysical Research* 75(18), 3665–3667.
- [49] Crecelius, E.A., 1981, Prediction of marine atmospheric deposition rates using total ^7Be deposition velocities. *Atmospheric Environment* 15, 579–582.
- [50] Todorovic, D., Popovic, D., Djuric, G., 1999, Concentration measurements of ^7Be and ^{137}Cs in ground level air in the Belgrade city area. *Environment International* 25(1), 59– 66.
- [51] Papastefanou, C., Ioannidou, A., 2004, Beryllium-7 and solar activity. *Applied Radiation and Isotopes* 61, 1493–1495.
- [52] Dueñas, C., Fernandez, M.C., Carretero, J., Liger, E., Cañete, S., 2004, Long-term variation of the concentrations of long-lived Rn descendants and Cosogenic ^7Be and determination of the MRT of aerosols. *Atmospheric Environment* 38, 1291–1301.
- [53] Al-Azmi, D., Sayed, A.M., Yatim, H.A., 2001, Variations in ^7Be concentrations in the atmosphere of Kuwait during the period 1994 to 1998. *Applied Radiation and Isotopes* 55, 413–417.
- [54] El-Hussein, A., Mohamemed, A., Abd El-Hady, M., Ahmed, A.A., Ali, A.E., Barakat, A., 2001, Diurnal and seasonal variation of short-lived radon progeny concentration and atmospheric temporal variations of ^{210}Pb and ^7Be in Egypt. *Atmospheric Environment* 35, 4305–4313.
- [55] Uematsu, M., Duce, R.A., Prospero, J.M., 1994, Atmosphere beryllium-7 concentrations over the Pacific Ocean. *Geophysical Research Letters* 21(7), 561–564.
- [56] Nicolas Preiss, Marie-Antoinette M61ires, and Michel Pourchet, 1996, A compilation of data on lead 210 concentration in surface air and fluxes at the air-surface and water-sediment interfaces, *JOURNAL OF GEOPHYSICAL RESEARCH*, VOL. 101(D22), 28,847-28,862.
- [57] National Institutes of Health U.S. Department of Health and Human Services, Air Pollution and Your Health,

- August 2020, <https://niehs.nih.gov>.
- [58] San Salvador, El Salvador, April 16-17, 2012, Air Quality Communication Workshop, Air Quality Communication Workshop.
- [59] Atmospheric Aerosols :Summary, 2020/12/12, source: <https://www.ucc.ie/en/media/research/crac/Brice2.pdf>.
- [60] William E. Wilson & Helen H. Suh, Fine Particles and Coarse Particles: Concentration Relationships Relevant to Epidemiologic Studies, ISSN 1047-3289 J. Air & Waste Manage. Assoc. 47:1238-1249.
- [61] W. C. Hinds, 1999. Aerosol Technology. Properties, Behavior, and Measurement of Airborne Particles, 2nd ed. Wiley-VCH Verlag GmbH & Co., Weinheim.
- [62] N. Akata, H. Kawabata, H. Hasegawa, K. Kondo, T. Sato, Y. Chikuchi, S. Hisamatsu, J. Inaba, 2009, Air mass origins by back trajectory analysis for evaluating atmospheric ²¹⁰Pb concentrations at Rokkasho, Aomori, Japan, Journal of Radioanalytical and Nuclear Chemistry, 279(2), 493–498.
- [63] B. KORGU, J. C. ROGER AND J. BATHIEBO, 2013, CLIMATOLOGY OF AIR MASS TRAJECTORIES AND AEROSOL OPTICAL THICKNESS OVER OUAGADOUGOU, GLOBAL JOURNAL OF PURE AND APPLIED SCIENCES VOL. 19, 169-181
- [64] Global circulation patterns, 2021/01/15, source: <https://www.metoffice.gov.uk/weather/learn-about/weather/atmosphere/global-circulation-patterns#:~:text=The global circulation can be entire dep>.
- [65] Benitez-Nelson, C.R., Buesseler, K.O., 1999, Phosphorus-32, phosphorus-37, beryllium-7, and lead-210: atmospheric fluxes and utility in tracing stratosphere/troposphere exchange. Journal of Geophysical Research 104 (D9), 11745–11754.
- [67] Bachhuber, H., Bunzl, K., 1992, Background levels of atmospheric deposition to ground and temporal variation of ¹²⁹I, ¹²⁷I, ¹³⁷Cs and ⁷Be in a rural area of Germany. Journal of Environmental Radioactivity 16, 77–89.
- [68] Dibb, J.E., 1989, Atmospheric deposition of beryllium-7 in the Chesapeake Bay region. Journal of Geophysical Research 94(D2), 2261–2265.
- [69] Olsen, C.R., Larsen, I.L., Lowry, P.D., Cutshall, N.H., Todd, J.F., Wong, G.T.F., Casey, W.H., 1985, Atmospheric fluxes and marsh-soil inventories of ⁷Be and ²¹⁰Pb. Journal of Geophysical Research 90(D6), 10487–10495.
- [70] Narazaki, Y., Fujitaka, K., Igarashi, S., Ishikawa, Y., Fujinami, N., 2003, Seasonal variation of ⁷Be deposition in Japan. Journal of Radioanalytical and Nuclear Chemistry 256(3), 489–496.
- [71] Harvey, M.J., Matthews, K.M., 1989, ⁷Be deposition in a high-rainfall area of New Zealand. Journal of

- Atmospheric Chemistry 8, 299–306.
- [72] Koch, D.M., Mann, M.E., 1996, Spatial and temporal variability of ^7Be surface concentrations. *Tellus* 48(B), 387–396.
- [73] Baskaran, M., Coleman, C.H., Santschi, P.H., 1993, Atmospheric depositional fluxes of ^7Be and ^{210}Pb at Galveston and College Station, Texas. *Journal of Geophysical Research* 98(D11), 20555–20571.

CHAPTER TWO

MATERIAL AND METHOD

2.1 Sampling site

The sampling site for the methods of sampling atmospheric aerosol and deposition were on a building roof of the building No. 16 located at Osaka Sangyo University, Daito, Osaka Prefecture, Japan (34.71 °N, 135.64 °E), and approximately 31 m above ground level. The sampling location is shown in **Fig. 2.1**.



Fig. 2.1 Location of the sampling site.

2.2 Radioactivity measurement

All filters were measured by an HPGe detector (GX2018, Canberra) that was shielded with a 10-cm-thick layer of lead in order to reduce the background radiation. The detector was connected to a data acquisition (DAQ) system to record the gamma ray signals of 477 keV for ^7Be and 46.5 keV for ^{210}Pb . At 46.5 keV, the spectrum show in **Fig. 2.2**. In order to achieve maximum efficiency the HPGe detectors must operate at the very low temperatures of liquid nitrogen

(-196°C), because at room temperatures the noise caused by thermal excitation is very high. The major drawback of germanium detectors is that they must be cooled to liquid nitrogen temperatures because germanium has relatively low band gap, these detectors must be cooled in order to reduce the thermal generation of charge carriers to an acceptable level. Otherwise, leakage current induced noise destroys the energy resolution of the detector. Cooling to liquid nitrogen temperature (-195.8°C ; -320°F) reduces thermal excitations of valence electrons so that only a gamma ray interaction can give an electron the energy necessary to cross the band gap and reach the conduction band. (What is LN₂ Cryostat – Cooling of HPGe Detectors – Definition) The HPGe detector in our lab was surrounding with 10 cm of lead shield since the detector was installed at our lab in order to reduce the background radiation. After July 9, 2020, we replace the new lead shield system for our detector, the lead thickness is 5 cm but this system is easily to change the sample, show in Fig. 2.3.

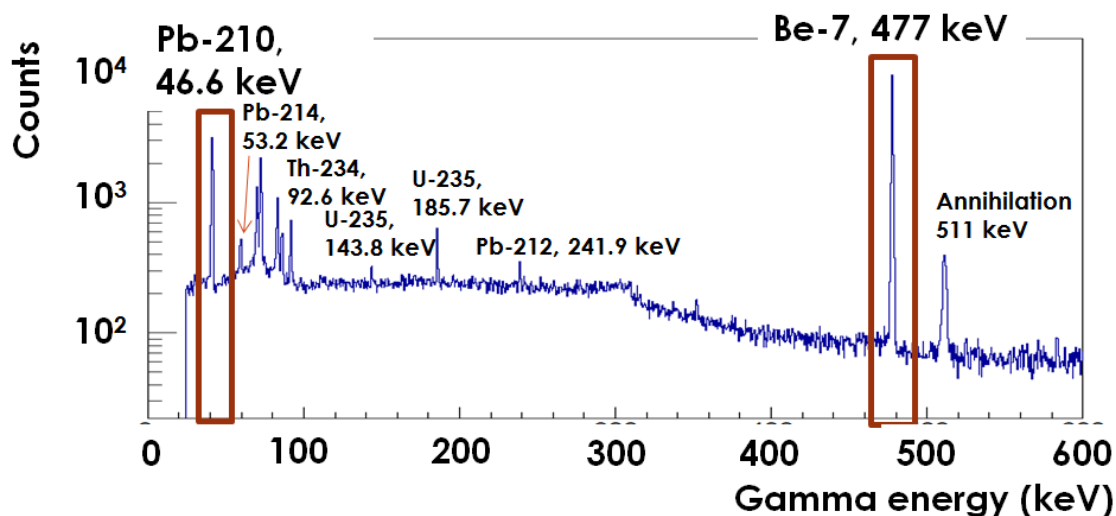


Fig. 2.2 The spectrum of the filter sample after measured by the HPGe detector showed the photopeak of ^{210}Pb at 46.5 keV and ^7Be at 477 keV.



Fig. 2.3 The HPGe detector with liquid nitrogen and (a) the period lead shield system and (b) new lead shield system.

Extended Range Coaxial Ge Detector (XtRa) (GX2018, CANBERRA), diameter of 61.80 mm, and length of 30.00 mm at out lab is a special type of detector that can measure the low energy, 3 keV is a lowest energy that this HPGe detector can detect **Fig. 2.4** shows the typical efficiency curves comparing XtRa with Be window (our detector type) and Coax Detector with detector-source spacing of 2.5 cm and the cross cession of the detector. **Fig. 2.5** shows the geometry of the detector and its Liquid Nitrogen (LN₂) Dewar.

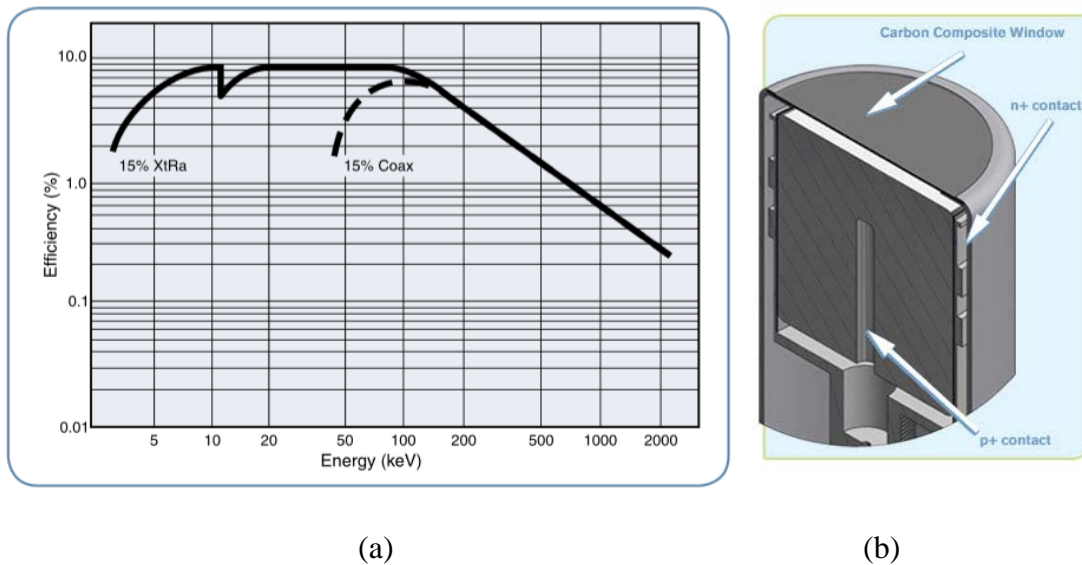


Fig. 2.4 (a) The typical efficiency curves comparing XtRa with Be window and Coax Detector with detector-source spacing of 2.5 cm and (b) the cross cession of the detector.(CANBERRA, 2016).

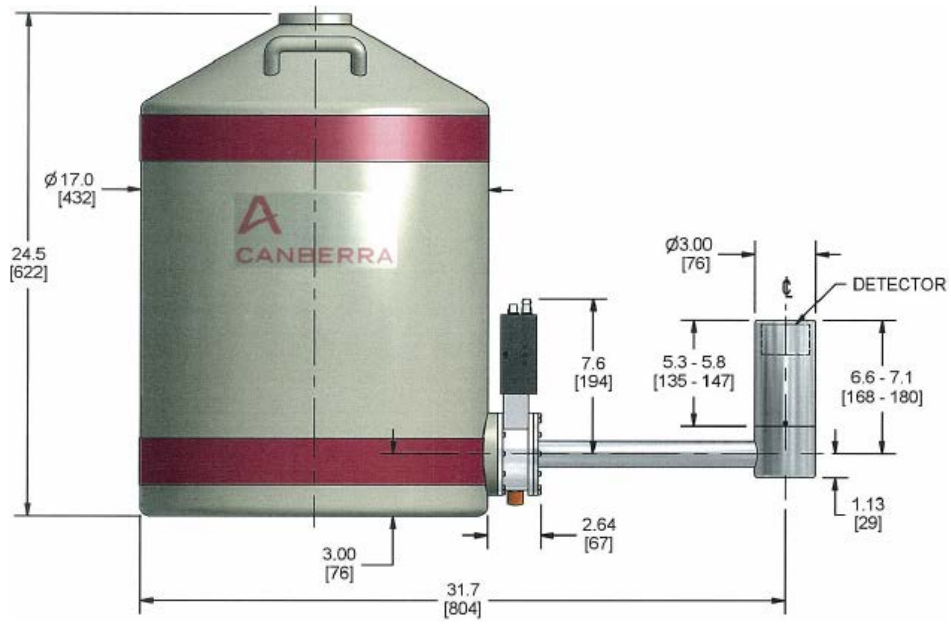


Fig. 2.5 The geometry of the detector and its Liquid Nitrogen (LN₂) Dewar.(CANBERRA, 2016).

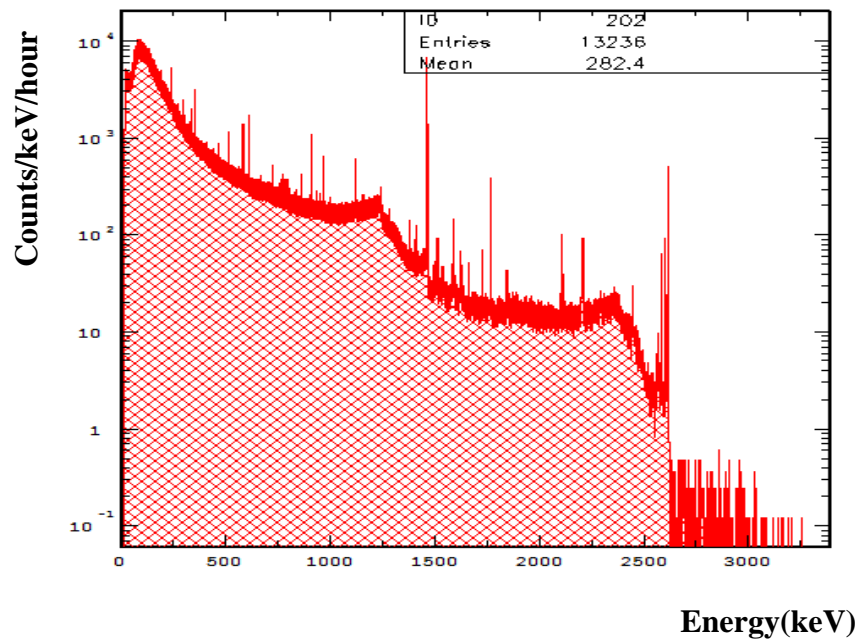


Fig. 2.6 The background measurement from on shield.

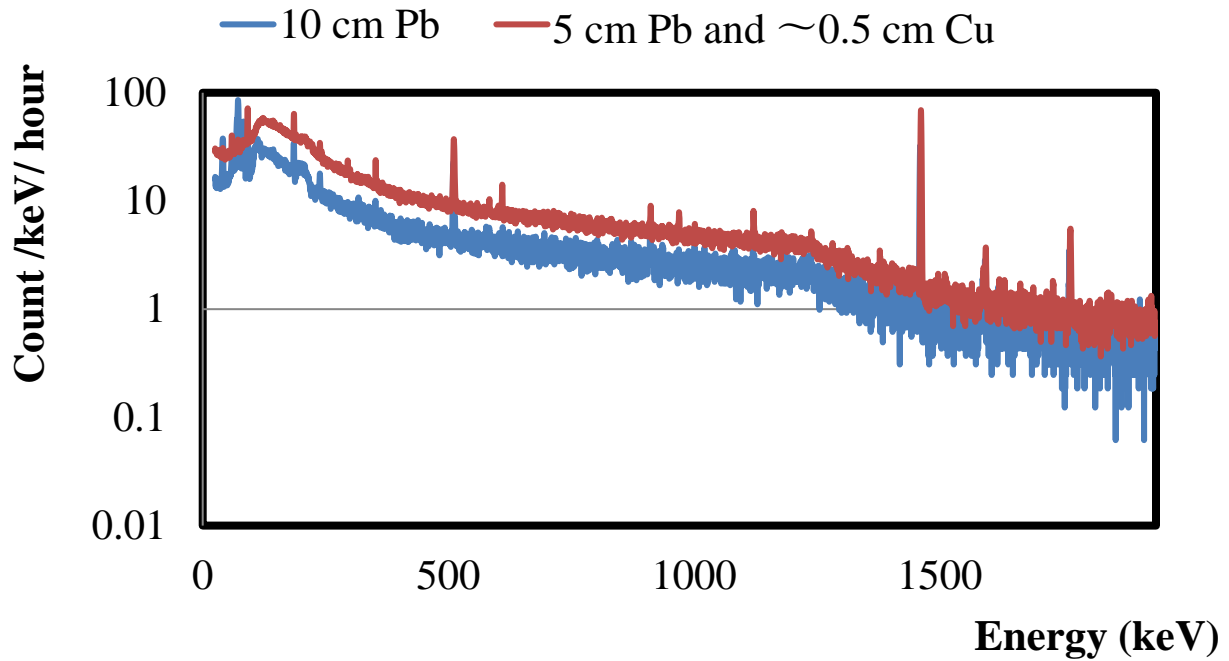


Fig. 2.7 The background measurement after surrounding by 10 cm of lead shield (before July 9, 2020) and 5 cm of lead shield + ~ 0.5 cm of copper (after July 9, 2020).

As I mention before our detector needs to be surrounded by the lead shield to decrease the background radiation. **Fig. 2.6** showed the background measurement from on shield, and **Fig. 2.7** showed the background measurement after surrounding by 10 cm of lead shield (before July 9, 2020) and 5 cm of lead shield and ~ 0.5 cm of copper (after July 9, 2020).

Due to the gamma energy of ^{210}Pb is very low (46 keV) and difficult to measure. We need to confirm that the background radiation at our lab is low enough to measure the low gamma energy. A comparison between our background measurements with background measurements around the world was required. **Fig. 2.8**, and **Table 2.1** shows the comparison between our background measurement and other labs. It shows that our shielding system can decrease background radiation and is comparable with other labs. It means our shielding system is enough for the measurement at low gamma energy.

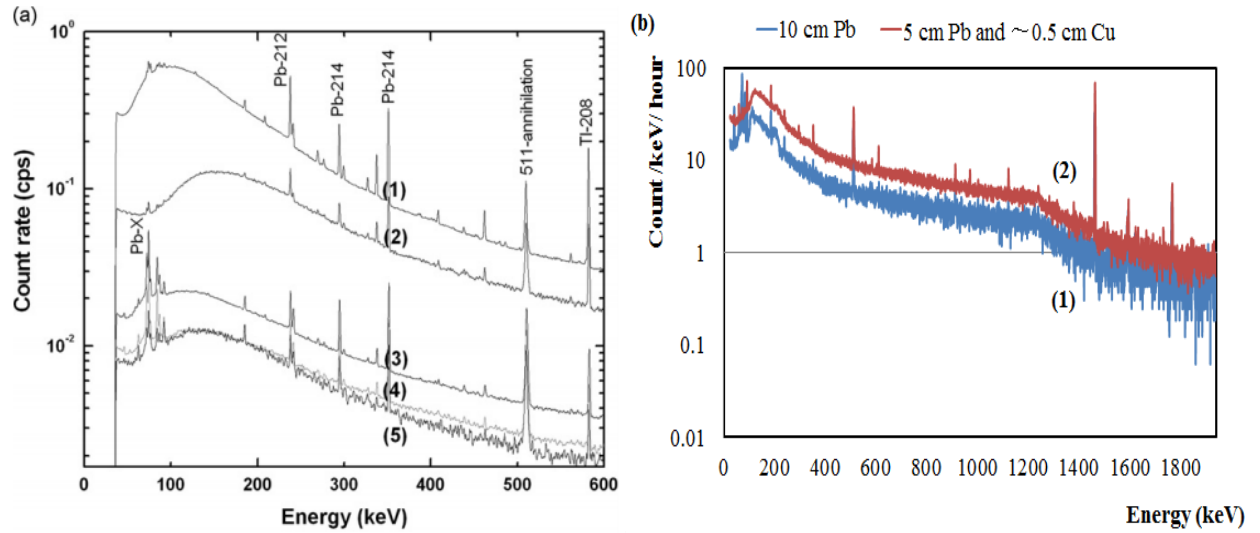
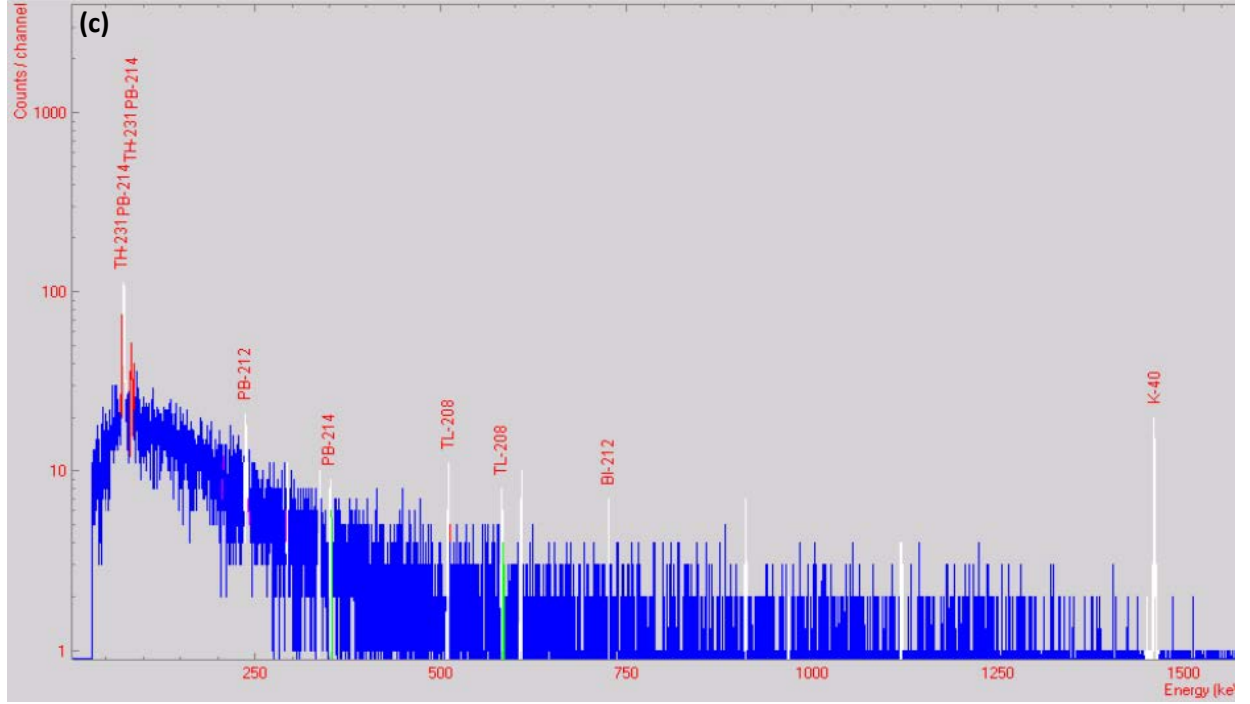


Fig. 2.8 (a) The spectrum background radiation at the Life and Environmental Physics Department at IFIN-HH [1], Romania ((1), (2), (3), (4), and (5) see the detail in **Table 2.1**), (b) the spectrum background radiation at our lab, Osaka, Japan ((1), and (2) see the detail in **Table 2.1**), and (c) the spectrum background radiation at Department of Physics, Karnatak University, India [2].

Table 2.1 The detail of the detectors, sheilding system, and the count.

Detector type	Shielding system	Energy range (keV)	Count (cps)	Error
^(a) a coaxial p-type HPGe detector (model GEM 25P4, Ortec Inc., Easley, SC, USA), a diameter of 59.1 mm and a length of 54.3 mm	1) no shield	0 - 1600	75.15	0.11
	2) 2 cm Cu	0 - 1600	57.88	0.04
	3) 10 cm unpolished Pb	0 - 1600	11.13	0.03
	4) 10 cm polished Pb	0 - 1600	6.88	0.02
	5) 10 cm polished Pb + 2 cm Cu.	0 - 1600	5.85	0.02
^(b) Extended Range Coaxial Ge Detector (XtRa) diameter of 61.80 mm, and length of 30.00 mm	1) 10 cm polished Pb	30 - 2000	1.69	0.001
	2) 5 cm polished Pb + 0.5 cm Cu	30 - 2000	2.95	0.01
^(c) a germanium p-type coaxial, 50 μ m external diameter, 37.1 mm length	11.75 cm polished Pb + 0.15 cm Cu + 0.10 cm Al	50 - 2000	6.65	0.333

^(a) The detail of the detector from Fig 2.8 (a).

^(b) The detail of the detector from Fig 2.8 (b).

^(c) The detail of the detector from Fig 2.8 (c).

2.3 Detection Efficiency

The detection efficiency is a measure of the percentage of radiation that a given detector detects from the overall yield emitted from the source. It can vary with the volume and shape of the detector material, absorption cross-section in the material, attenuation layers in front of the detector, and distance and position from the source to the detector [3].

The detection efficiency for the deposition sample in U8 container used the standard source is MX033U8PP, 4132-5cm (Show in **Fig. 2.10**) that have the same geometry with our sample. The detail of standard source showed in **Table 2.2** and the detection efficiency curve shows in **Fig 2.9**. From the efficiency equation from the curve, we calculate the detection efficiency at 46 keV of ²¹⁰Pb is 5.35 \pm 0.18 % and 477 keV of ⁷Be is 1.89 \pm 0.37 %.

Table 2.2 The detail of standard source MX033U8PP, No. 4132-5cm, the source thickness is 5 cm.

Reference date is July 7, 2016.

Gamma Energy (keV)	Nuclide	Half-Life (days)	Yield per decay (Pr)
88.03	Cd-109	461.40	0.04
122.06	Co-57	271.74	0.86
136.47	Co-57	271.74	0.11
165.86	Ce-139	137.64	0.80
320.08	Cr-51	27.70	0.10
514.00	Sr-85	64.85	0.96
661.66	Cs-137	10979.20	0.85
834.85	Mn-54	312.20	1.00
898.04	Y-88	106.63	0.94
1173.23	Co-60	1925.28	1.00
1332.49	Co-60	1925.28	1.00
1836.06	Y-88	106.63	0.99

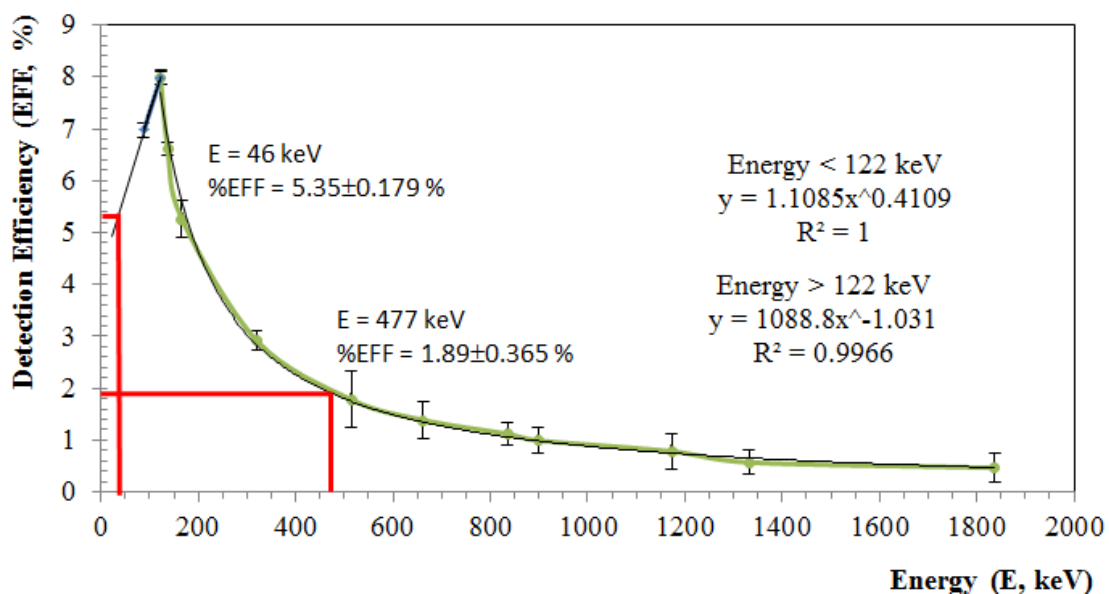


Fig 2.9 Curve of detection efficiency of the standard source MX033U8PP, 4132-5cm.

Measurement date is March 23, 2017, and measurement time is 16.73 h.



Fig. 2.10 The standard source is MX033U8PP set, the cross section of standard source No. 4132-5cm.

Fig. 2.11 shows the detection efficiency for the air dust from the air high volume air sample and the cascade impactor the diameter. We used the standard source is Eu-152 (Show in **Fig. 2.12**) that have the same geometry with our sample. The detail of standard source showed in **Table 2.3**. From the efficiency equation from the curve, we calculate the detection efficiency at 46 keV of ^{210}Pb is $9.23 \pm 0.11 \%$ and 477 keV of ^7Be is $2.78 \pm 0.06 \%$.

Table 2.3 The detail of standard source Eu-152, the diameter is 20mm, 2mm thickness, and reference date December 14, 1987.

Gamma Energy (keV)	Yield per decay (Pr)	Activity (Bq)
39.91	0.591	8.20
45.7	0.149	2.07
121.78	0.2858	3.96
244.7	0.0758	1.05
411.12	0.02234	0.31
443.96	0.03148	0.44
778.9	0.1294	1.80
867.37	0.04245	0.59
964.08	0.146	2.03
1085.9	0.1021	1.42

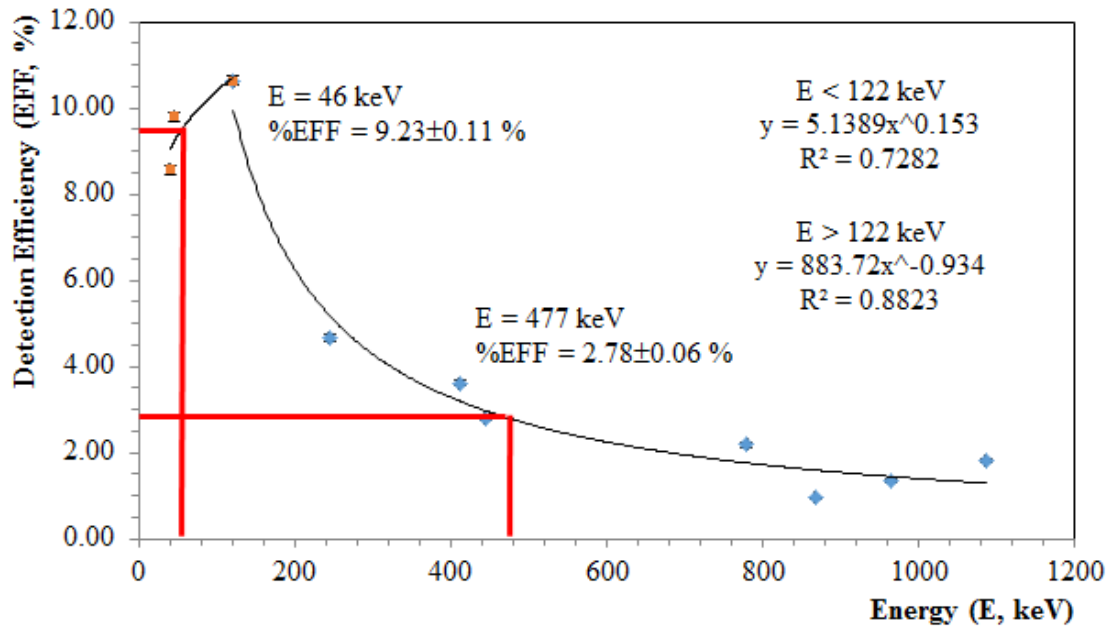


Fig. 2.11 Curve of detection efficiency of the standard source Eu-152. Reference date is December 14, 1987, measurement date is April 17, 2020, and measurement time is 50 h.



Fig. 3.12 The standard source Eu-152 0.8601 g , 20mm diameter and around 2mm thickness activity is 41.75 Bq.

2.4 Air dust

2.4.1 Samples collation and preparation

Weekly air dust samples had been collected to analyze the ^7Be concentration from January 8, 2018, to December 31, 2021, using a high volume air sampler (HV-1000R, Sibata) is shown in

Fig. 2.13 (a) with a constant flow rate of 1,000 L/min and a filtered air volume of approximately 10,080 m³ and were then passed through the glass filter (GB-100R, 203×254 mm²) with 0.3 μm pore size and 99.99% gas collection efficiency. After the samples collected, the glass filter was pack in the plastic bag (shown in **Fig. 2.13** (b)) to avoid the HPGe detector was contaminating the air sample. Before collect the sample the glass filter need to be weight and the glass filters before and after collected the air dust sample is shown in **Fig. 2.14**. HV-1000R can collect airborne dust by attaching the through a pipe. Similarly, it can also be used to collect dioxins by attaching the shuttle tube (tube for polyurethane foam attachment). It provides a high accuracy flow rate, which is calculated automatically with temperature and atmospheric pressure correction.

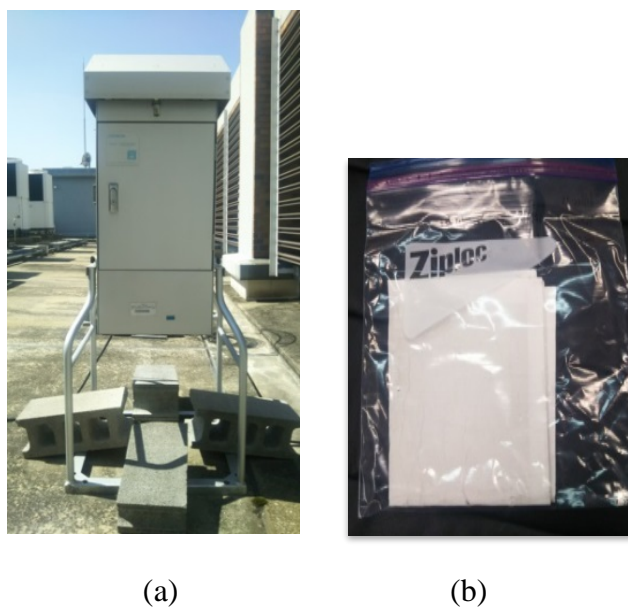


Fig. 2.13 (a) The high volume air sample (HV-1000R, Sibata) and (b) glass filter after collected the air dust sample was pack in a plastic bag.

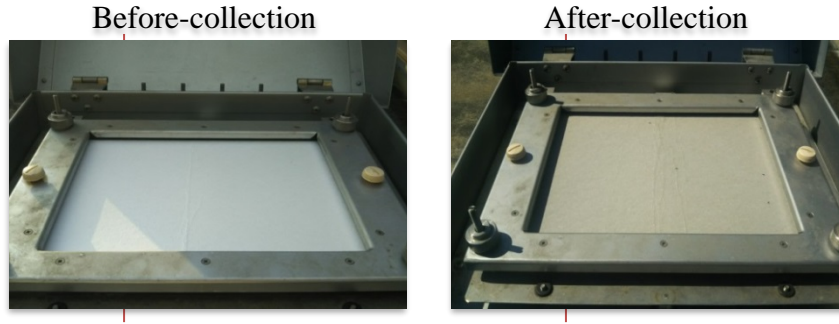


Fig. 2.14 The glass filters before and after collected the air dust sample.

2.4.2 Atmospheric concentration (Bq/m³)

The ⁷Be and ²¹⁰Pb concentration can be calculated by following the equation below.

Activity in becquerel (Bq)

$$= \frac{\text{Count in count per seacond (cps)}}{\text{Measurement time (s)} \times \text{Branching ratio} \times \text{Detection efficiency}}$$

$$\text{Concentration in Bq/m}^3 = \frac{\text{Activity in Bq}}{\text{Total air flow from HV} - 1000R}$$

The count was provided fitting the photo peak of 477 keV for ⁷Be and 46.5 keV for ²¹⁰Pb by using PAW (Physics Analysis Workstation). PAW is an interactive utility for visualizing experimental data on a computer graphics display, this software tool was developed by CERN (The European Organization for Nuclear Research). Gaussian (3 parameter) fitting with an Exponential (2 parameter) background at the photopeak was used to provide the required values to calculate the peak area represent the count. The example of photopeak fitting shows in **Fig. 2.15**.

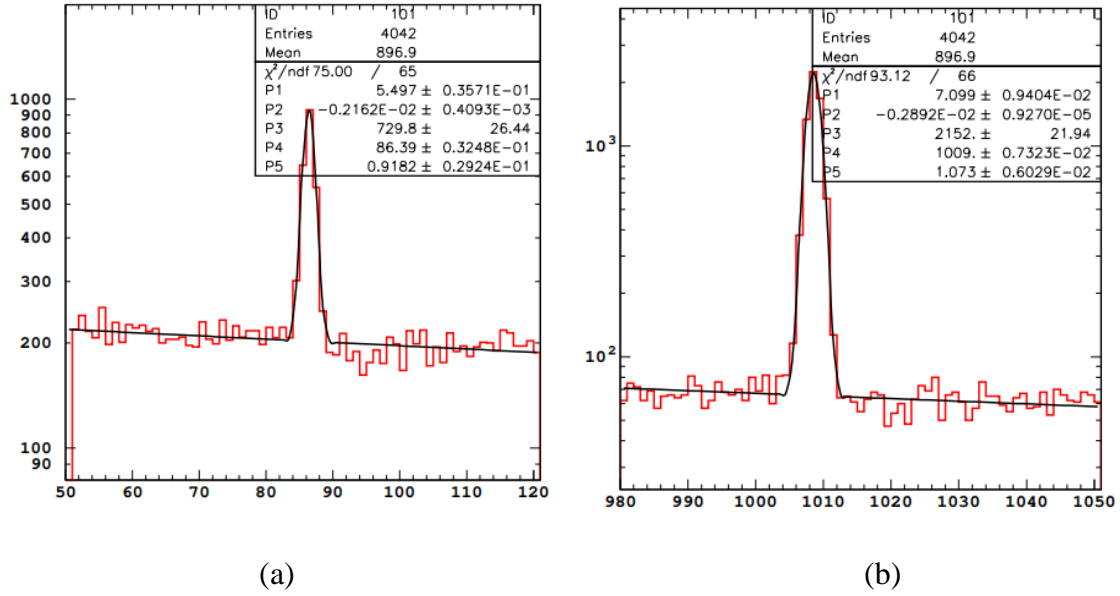


Fig. 2.15 (a) Gaussian (3 parameter) fitting with an Exponential (2 parameter) background at the photopeak of (a) 46.6 keV and (b) 477 keV, X axis is channel and Y axis is count.

The peak area or count and statistical error can be calculated by following the equation below.

$$\text{The peak area or count} = P3 \times P5 \times \sqrt{2\pi}$$

$$\text{Statistical error} = \frac{1}{\sqrt{\text{area}}}$$

When P1 and P2 is constant and slope value from Exponential function, and

P3 is high, P4 is the center of the peak, and P5 is sigma value from Gaussian function.

2.4.3 Factors causing variation

Weekly variations of ^7Be concentrations were used to calculate the monthly concentration and were compared with variations of sunspot number, which were provided by NOAA, USA [4], cosmic ray, which were provided by Cosmic Ray Station of the University of Oulu, Finland [5],

PM_{2.5} (Particulate Matter), which were measured at Daito City Hall (34.71 N, 135.62 E) via Osaka Prefectural Government, Air Pollution constant monitoring data file [6], precipitation, pressure, wind speed, and relative humidity, which were provided by our weather station at the Research Center building located in Osaka Sangyo University, Daito, Osaka (34.71 N, 135.64 E) were analyzed.

For the total suspended particle (TSP) in g/m³, the glass filter after collect the sample was dried in electric oven at 80°C for 48 hours and was re-weighted to provide the aerosol mass concentration. TSP was calculated using the difference in filter weight divided by the total flow rate.

2.4.4 The back trajectory simulation

We analyzed the back trajectory of air mass motion using HYSPLIT [7]. In this simulation, the meteorological data set GDAS1 (Global Data Assimilation System) was provide by the NOAA's Air resources Laboratory (ARL). The 72 hours duration back trajectories were calculated for every 24 hours during the sampling period for each weekly sample. The endpoint of trajectories was set at the sampling site, with the height of 2,000 m, 6,000 m, and 20,000 m above mean sea-level (MSL) for ⁷Be, and 200 to 500, m 1,000 m, and 1,500 m MSL for ²¹⁰Pb. These heights are chosen because they allow the study of air motion in the atmospheric boundary layer is which is the atmospheric turbulence that strongly influences the meteorology and dispersion (approximately lower 1500 m) and the troposphere where occurs the long-range transport of aerosols (2,000 m and 6,000 m) and the border between the troposphere and the stratosphere, which is the level of ⁷Be production (20,000 m). The detail of the back trajectory simulation by using HYSPLIT model follows the process below.

1) The back trajectory simulation, we can use the online simulation by going to the webpage: <https://ready.arl.noaa.gov/HYSPLIT.php>. And then click Run HYSPLIT Trajectory Model.

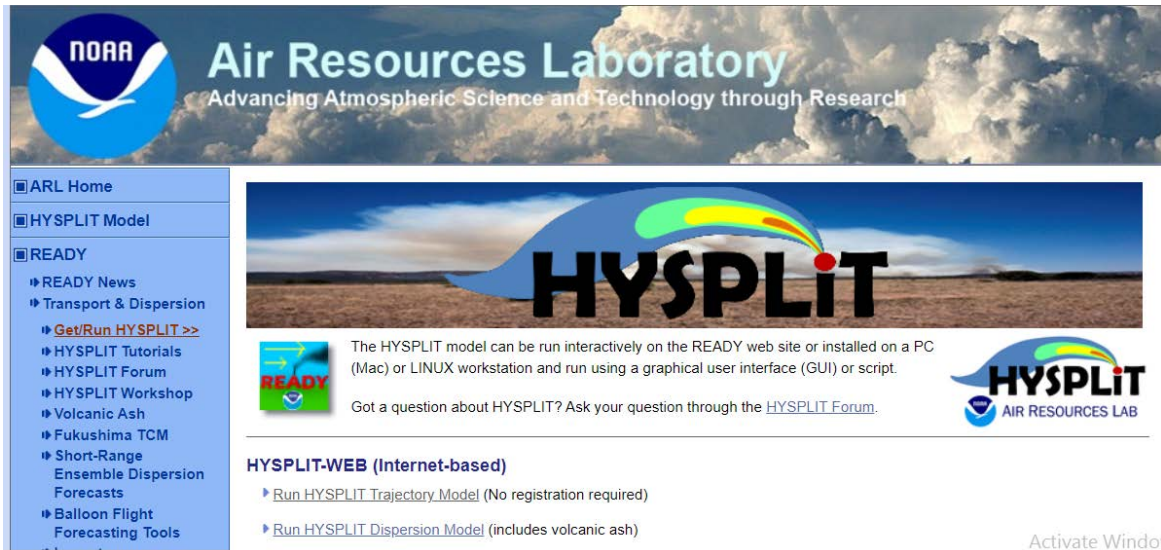


Fig. 2.16 HYSPLIT model's webpage.

2) click Compute archive trajectories

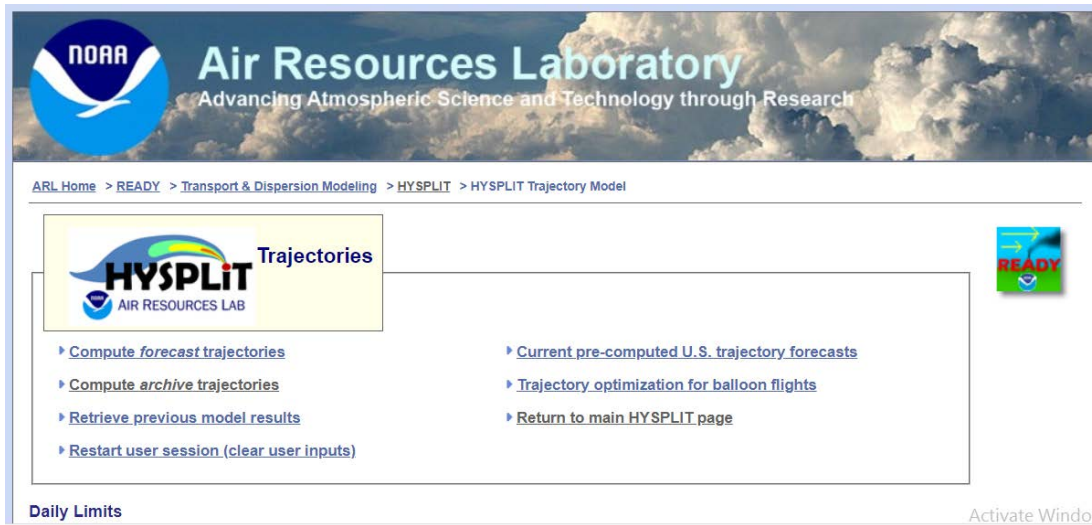



Fig. 2.17 HYSPLIT Trajectories's page.

3) Number of Trajectory Starting Locations choose No. 1 and Type of Trajectory choose normal and Next.



Air Resources Laboratory
Advancing Atmospheric Science and Technology through Research

ARL Home > READY > Transport & Dispersion Modeling > HYSPLIT > HYSPLIT Trajectory Model



READY users produced 5742 un-registered HYSPLIT simulations since 00 UTC today!

Type of Trajectory(ies)

Number of Trajectory Starting Locations

☒ 1 Note: By choosing just one source location, more options for selecting the location will be presented on the next page, such as choosing by latitude/longitude, by WMO ID, or by plant location. Multiple source locations limit the input to just latitude/longitude positions. This option is ignored for trajectory ensemble and frequency.

☐ 2

☐ 3

Type of Trajectory

☒ Normal ☐ Matrix ☐ Ensemble ☐ Frequency

Next>>

Activate Windows

Fig. 2.18 Type of Trajectory's page.


4) Select the Meteorological Datasets GDAS - 1°, the detail of Meteorological Datasets show in **Table 2.3**. Identify the location by putting latitude and longitude. In the study, the location is 34.71 N, 135.64 E and then Next (show in **Fig. 2.19**).

Meteorology & Starting Location(s)

Trajectory Calculation

Meteorology: GDAS (1 degree, global, 2008-present) [More info](#)

Source Location (enter using one of the following methods):



Click a location on the map or select from below:

☒ Decimal Degrees Latitude: 34.71 N Longitude: 135.64 E

☐ DDD/MM/SS Latitude: Deg. Min. Sec. N Longitude: Deg. Min. Sec. W

☐ City (Country or State; name: lat: lon):

☐ Airport or WMO ID (i.e., dca): ID Lookup

Reset Form Next>>

Fig. 2.19 Meteorology & Starting Location's page.

Table 2.3 Meteorological Datasets Available from NOAA ARL Archives.

	Dataset	Horizontal Resolution (km-approx.)	Full-grid dimensions	Temporal resolution (hrs)	Vertical Levels	Period of each file	Size of each file (GB)	Total size for one month of data (GB)	Availability
North American**	HRRR-3km	3	1799 x 1059	1	37	¼ day	3.2	390	Jun 2015 -> present
	NAMS-12km Hybrid	12 km: Conus 12 km: Alaska 2 km: Hawaii		1	40	1 day	1.0 0.64 0.71	30 19 21	2010 -> present
	NAM-12km	12	614 x 428	3	27	1 day	0.395	12	May 2007 -> present
	WRF-ARW-27km	27	216 x 174	1	35	1 day	0.210	6.4	1980-2017***
	NARR-32km	32	309 x 237	3	24	1 month	2.8	2.8	1979 -> present
	EDAS-40km	40	185 x 129	3	27	½ month	0.6	1.2	2004 -> 2018
Global	GFS - 0.25°	27	1440 x 721	3	56	1 day	2.7	82	Jun 2019 -> present
	GDAS - 0.5°	55	720 x 361	3	56	1 day	0.468	14	Sep 2007 -> Jun 2019
	GDAS - 1°	111	360 x 181	3	24	1 week	0.571	2.5	Dec 2004 -> present
	Global Reanalysis - 2.5°	278	144 x 73	6	18	1 month	0.11	0.11	1948 -> present

* These are the most commonly used datasets, but there are other datasets available in the archive,

** All North American datasets cover the Continental United States, but have varying coverage of Canada, Mexico, and adjacent oceanic regions.

*** WRF-27km data will most likely continue to be updated.

5) Choose an archived meteorological file to correspond to the analysis period.

Meteorology File

Meteorology: Archived GDAS1
Source Location: Lat: 34.710000 Lon: 135.640000

Choose an archived meteorological file
Archive File: gdas1_dec04.w3 ▾

Next>>

Fig. 2.20 Archived meteorological file's page.

6) Specify the parameter to run the simulation model, following the list below.

The screenshot shows the 'Model Run Details' page. At the top right is a 'Request trajectory' button. Below the title, a message states: 'The archived data file (GDAS1) has data beginning at 11/29/20 0000 UTC.' The main section is titled 'Model Parameters' and contains several groups of settings:

- Trajectory direction:** Radio buttons for 'Forward' and 'Backward (Change the default start time!)'. The 'Backward' option is selected.
- Vertical Motion:** Radio buttons for 'Model vertical velocity', 'Isobaric', and 'Isentropic'. 'Model vertical velocity' is selected.
- Start time (UTC):** A note says 'Current time: 17:50'. Below are pull-down menus for year (20), month (11), day (29), and hour (00).
- Total run time (hours):** A text input field containing '312'.
- Start a new trajectory every:** A text input field containing '0' followed by 'hrs'.
- Maximum number of trajectories:** A text input field containing '13'.
- Start 1 latitude (degrees):** A text input field containing '34.710000'.
- Start 1 longitude (degrees):** A text input field containing '135.640000'.
- Start 2 latitude (degrees):** An empty text input field.
- Start 2 longitude (degrees):** An empty text input field.
- Start 3 latitude (degrees):** An empty text input field.
- Start 3 longitude (degrees):** An empty text input field.
- Automatic mid-boundary layer height?** Radio buttons for 'Yes' and 'No'. 'No' is selected.
- Will override selections below.** A label for the following height settings.
- Level 1 height:** A text input field containing '2000'.
- Level 2 height:** A text input field containing '6000'.
- Level 3 height:** A text input field containing '20000'.
- Units:** Radio buttons for 'meters AGL' and 'meters AMSL'. 'meters AMSL' is selected.

Each major parameter group has a 'More info' link with a right-pointing arrow.

Fig. 2.21 Model Parameter's page.

6.1) Trajectory direction: Backward: This is the direction of the trajectory calculation. Note that you must change the default starting time when computing FORECAST backward trajectories because the default time is the start of the meteorological forecast, and thus the model cannot calculate backward prior to the initial forecast time.

6.2) Start time (UTC): year/month/day/hour: Enter the start time of the pollutant release using the pull down menus. The time MUST be entered as UTC time. The default time is the current time.

6.3) Total run time (hours): 312, we specify the backward trajectory for 13 days: Specify the duration of the calculation in hours. The default number in the case of forecast

trajectories corresponds to the maximum length of the forecast dataset. A maximum of 315 hours can be specified for archive datasets on the web.

6.4) Start a new trajectory every: 0 h, Maximum number of trajectories: 13: Specify how often (every X hours) a new trajectory is started from the source location.

6.5) Specify the latitude and longitude: 34.71, 135.64: The source latitude that was previously entered is shown in decimal degrees (XX.XX). If this number is changed, the entry must be in decimal degrees. South latitudes are indicated as negative latitude.

The source longitude that was previously entered is shown in decimal degrees (XXX.XX). If this number is changed, the entry must be in decimal degrees. Western hemisphere longitudes are indicated as a negative longitude.

6.6) Automatic mid-boundary layer height.

6.7) height had 3 level meters above mean sea-level (AMSL).

7) Specify the Display Options

7.1) Plot resolution (dpi): 96: Choose the resolution (size) of the final graphic images in dots-per-inch (dpi), which is what is calculated for creating the Postscript graphics.

7.2) Zoom factor: 70: The zoom factor allows the user to "zoom in" on the trajectories with 0 being the least zoomed and 100 being the most zoomed in on the trajectories.

7.3) Plot projection: Default: The output graphic can be plotted on a polar stereographic, lambert conformal, or Mercator projection. The Default will depend on the source location latitude.

7.4) Vertical plot height units: Meters AGL

7.5) Label Interval: 24 hours: The trajectories can be labelled every x hours with a symbol.

7.6) Plot color trajectories: Yes

- 7.7) Use same colors for each source location: Yes
- 7.8) Plot source location symbol: Yes
- 7.9) Distance circle overlay: None
- 7.9) U.S. county borders: No
- 7.10) Postscript file: No
- 7.11) PDF file: Yes
- 7.12) Plot meteorological field along trajectory: No
- 7.13) Dump meteorological data along trajectory: Terrain Height (m)
- 7.14) Click: Request trajectory, the display of the backward trajectory file will show after a few minute. We can choose GIF file or PDF file.

Display Options

GIS output of contours?
☒ None
☐ Google Earth (kmz)
☐ GIS Shapefile
[More info](#)

The following options apply only to the GIF, PDF, and PS results (not Google Earth)

Plot resolution (dpi):
[More info](#)

Zoom factor:
[More info](#)

Plot projection:
☒ Default
☐ Polar
☐ Lambert
☐ Mercator
[More info](#)

Vertical plot height units:
☐ Pressure
☒ Meters AGL
☐ Theta
[More info](#)

Label Interval:
☐ No labels
☐ 1 hour
☐ 6 hours
☐ 12 hours
☒ 24 hours
[More info](#)

Plot color trajectories?
☒ Yes
☐ No
[More info](#)

Use same colors for each source location?
☒ Yes
☐ No
[More info](#)

Plot source location symbol?
☒ Yes
☐ No
[More info](#)

Distance circle overlay:
☒ None
☐ Auto
[More info](#)

U.S. county borders?
☐ Yes
☒ No
[More info](#)

Postscript file?
☐ Yes
☒ No
[More info](#)

PDF file?
☒ Yes
☐ No
[More info](#)

Plot meteorological field along trajectory?
☐ Yes
☒ No

Note: Only choose one meteorological variable from below to plot
[More info](#)

Dump meteorological data along trajectory:
☒ Terrain Height (m)
☐ Potential Temperature (K)
☐ Ambient Temperature (K)
☐ Rainfall (mm per hr)
☐ Mixed Layer Depth (m)
☐ Relative Humidity (%)
☐ Downward Solar Radiation Flux (W/m**2)
[More info](#)

Fig. 2.22 Display Options's page.

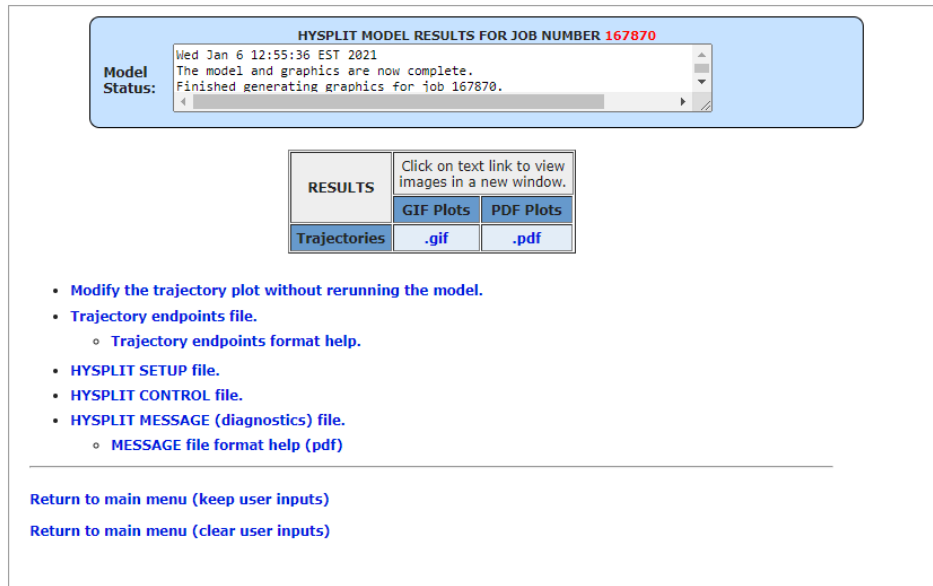


Fig. 2.23 The display of the backward trajectory simulation result.

2.5 Fallout density

2.5.1 Samples collation and preparation

Bulk atmospheric deposition sample which mixed wet and dry depositions were collected monthly from November 2019 to October 2020 using a small basin with an open surface area of 0.14 m² deposition. Deionized water was poured into the collector to ensure the capture of dry deposition, and dust fall sample the collection area of 0.07 m² (shown in **Fig. 2.24**) was used for wet deposition. Collected samples were passed through a POWDEX-PCH and POWDEX-PAO in the column for collecting the various radioactive species. The homogenized resin was dried in an electric oven at 80°C for over 48 hours, followed by packing into plastic containers (U8). This sample resin was measured the activity by using HPGe detector. The Powdex resin (Ecodyne Co., USA) and the resin sample shown in **Fig. 2.25** and **2.26** respectively.



Fig. 2.24 A small basin with an open with an open surface area of 0.14 m^2 (left side) for total deposition dust fall sample the collection area of 0.07 m^2 for wet deposition (right side).



Fig. 2.25 PAO resin (OH^- form): Powdered hydroxide form anion exchange resin PCH resin (H^+ form)): Powdered hydrogen form cation exchange resin.



Fig 2.26 The resin sample in U8 container.

The detail of this process follows the process below.

1. Weight the resin 40 g of each (POWDEX-PCH 40 g and POWDEX-PAO).

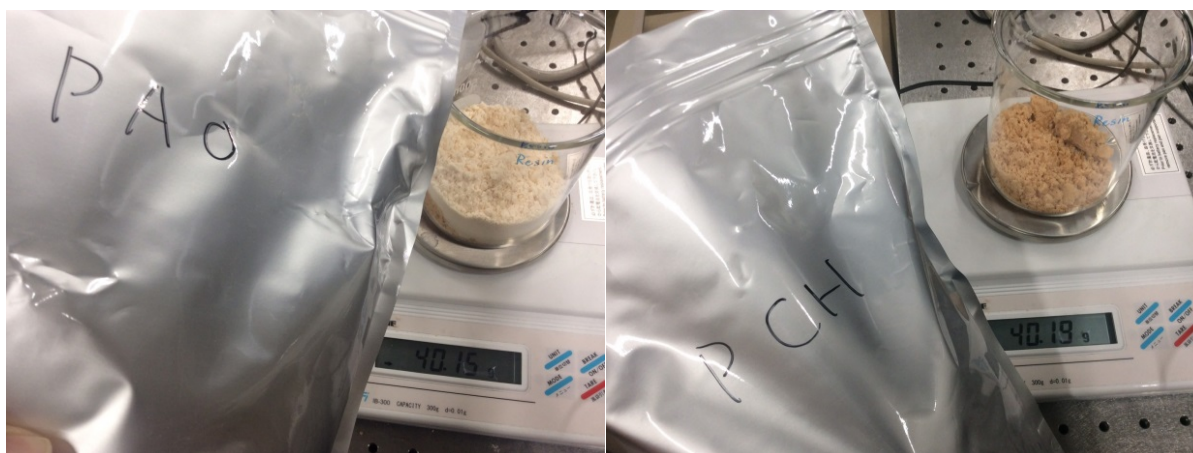


Fig. 2.27 Weight the resin 40 g of each.

2. Pour 1.5 L of pure water into the resin and mix the resin together, wait a few minutes and then pour the pure water out of the resin as must as possible.



Fig 2.28 Mix the resin in pure water and pour the water out of the resin.

3. Pour 1.5 L in the resin and mix them by 30 minutes stirrer.



Fig 2.29 Mix the resin with 30 minutes stirrer.

4. During 30 minutes stirrer, we should make the column in this time.

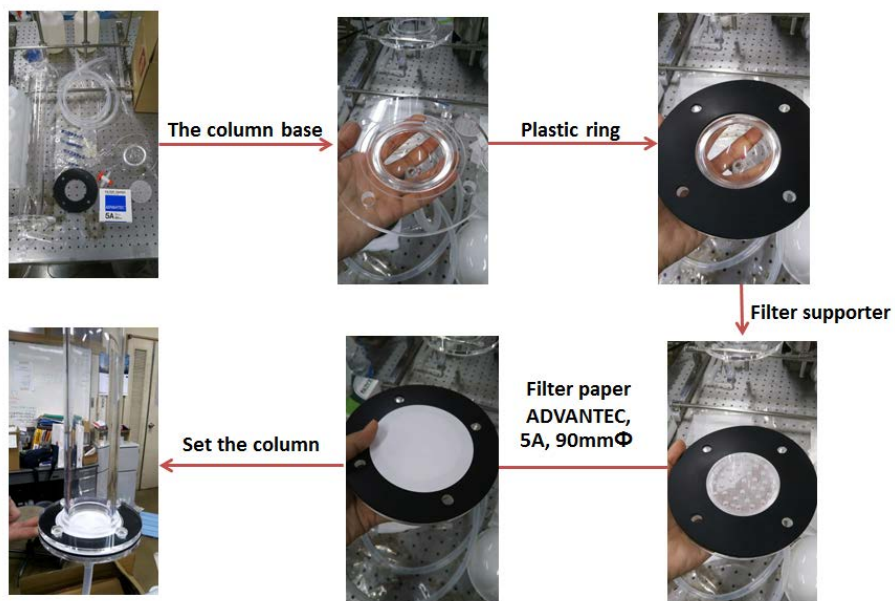


Fig 2.30 How to make the column.

5. After 30 minute stirrer we pour pure water out of the resin as must as possible and the pour the resin into the column.



Fig 2.31 Pour resin into the column.

6. This process the sample will pass through the resin and ^7Be , and ^{210}Pb will be absorbed into the resin and we check the absorbing of soluble fraction to resin by EC meter at the water outlet. The EC meter should be 0 mS/m. S/m (siemens per meter) is the SI (International System) unit of electrical conductivity. Conductance is the reciprocal of resistance, and one siemens is equal to the reciprocal of one ohm. The name siemens for the unit of conductance was adopted by the 14th General Conference on Weights and Measures as an SI-derived unit in 1971. It was named after Ernst Werner von Siemens [8].

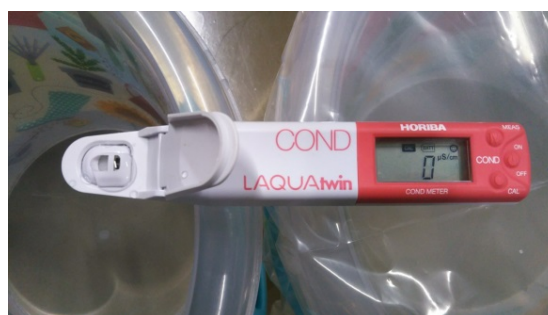


Fig. 2.32 Check the absorbing of soluble fraction to resin by EC meter at the water outlet.

The EC meter should be 0 mS/m.

7. After the sample pass through the resin wait for 20 minutes to release the water out of resin as must as possible.



Fig. 2.33 Wait for 20 minutes after all sample pass through the resin.

8. Pour the homogenous resin into the evaporating dish and dry it in electric oven at 80°C for over 48 hours and then leave it cool in desiccator around 1 hour. We will get the dried homogenous resin that contains ^7Be and ^{210}Pb .



Fig. 2.34 The dried homogenous resin that contain ^7Be and ^{210}Pb .

9. Must the resin to be a powder and then pack it in to the U8 container and fit the geometry by acrylics plate. Before and after pack the resin into the U8 container we need to wait it to know the mass of the resin sample. We will use the resin sample to measure the ^7Be and ^{210}Pb by HPGe detector.

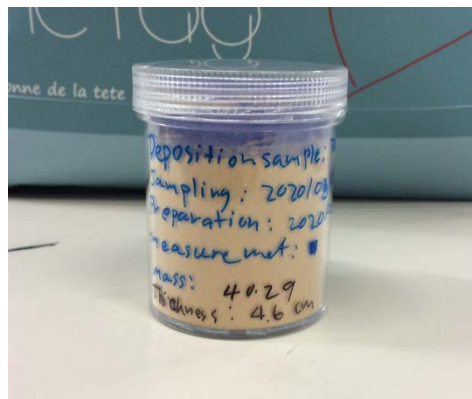


Fig. 2.35 The resin sample in U8 container.

2.5.2 Atmospheric deposition (Bq/m²)

$$\text{Concentration in Bq/m}^2 = \frac{\text{Activity in Bq}}{\text{Collection area (m}^2\text{)}}$$

2.6 Aerosol size and Chemical form

The air dust sample was classified into 12 states during the summer of 2020 by using a low-pressure cascade impactor shown in **Fig. 2.36** (12 stages with backup filter, Tokyo Dylec Corp., Japan, model LP-20) with a constant flow rate of 20 L/min. By using the cascade impactor with 12 multi-jet stages, it can classify aerosols into 12 sizes with the cut-off values for the impactor at 50% collection efficiency of 12.10, 8.50, 5.70, 3.90, 2.50, 1.25, 0.76, 0.52, 0.33, 0.22, 0.13, and 0.06 μm in aerodynamic diameters. The samples for radioactivity measurement were prepared by filtration of $\text{Be}(\text{OH})_2$ form and we measured its activity at gamma-ray energy with 477 keV by using a HPGe detector (GX2018, Canberra). For water-soluble inorganic ions, focused on the significant constituents of the PM are nitrate (NO_3^-), ammonium (NH_4^+), sulfate (SO_4^{2-}) and sea salt representing a 1:1 ratio of sodium ion (Na^+) and chloride ion (Cl^-) were measured by ion chromatography (DIONEX, ICS-1100) shown in **Fig 2.36**.



Fig. 2.36 Low-pressure cascade impactor (left side) and ion chromatography (right side).

Pour 25 ml of the super pure water into the glass plate and then extract the air dust from in ultrasonic cleaner for 15 minutes. We used 3 ml for measure the chemical form by using ion chromatography (DIONEX, ICS-1100) with a conductivity detector. The guard and the analytical column used for anion were Dionex IonPac AG14A and Dionex IonPac AS14A, respectively, and measured the sample at 35°C. The guard and the analytical column used for cation were Dionex IonPac CG12A and Dionex IonPac CS12A, respectively, and measured the sample at 40°C. The anion mixed standard solution IV and the cation mixed standard solution II (Kanto Chemical Co., INC) were used to make the calibration curve of the inorganic ions concentration. 22 ml for filtration of $\text{Be}(\text{OH})_2$ form to measure the ^7Be activity. The Millipore filter paper samples were used to measure the activity concentration of ^7Be by an HPGe detector (GX2018, Canberra). The detector was connected to a data acquisition (DAQ) system to record the gamma ray signals of 477 keV. The detail of filtration of $\text{Be}(\text{OH})_2$ form following the process below.

1. Add 0.2mL of BeSO_4 (Beryllium sulfate) solution (1.1mol/L) to the sample solution (22 mL).

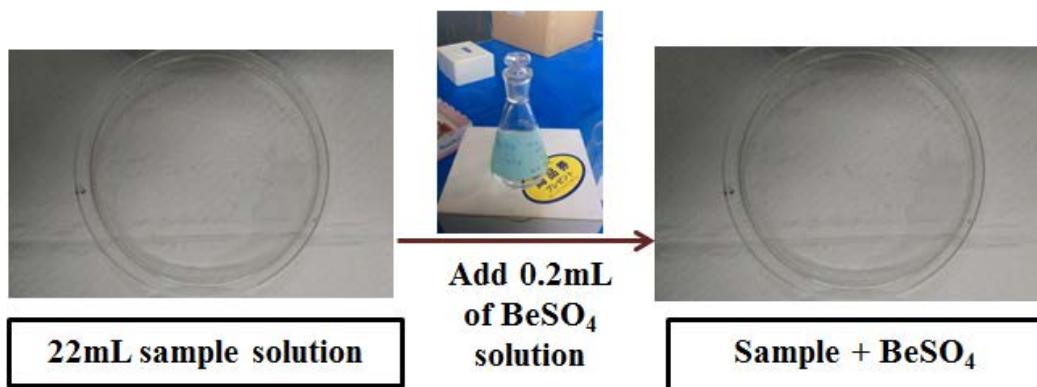


Fig. 2.37 22 ml sample solution before and after add 0.2 ml of BeSO_4 .

2. Add several drops of pH indicator (phenolphthalein)

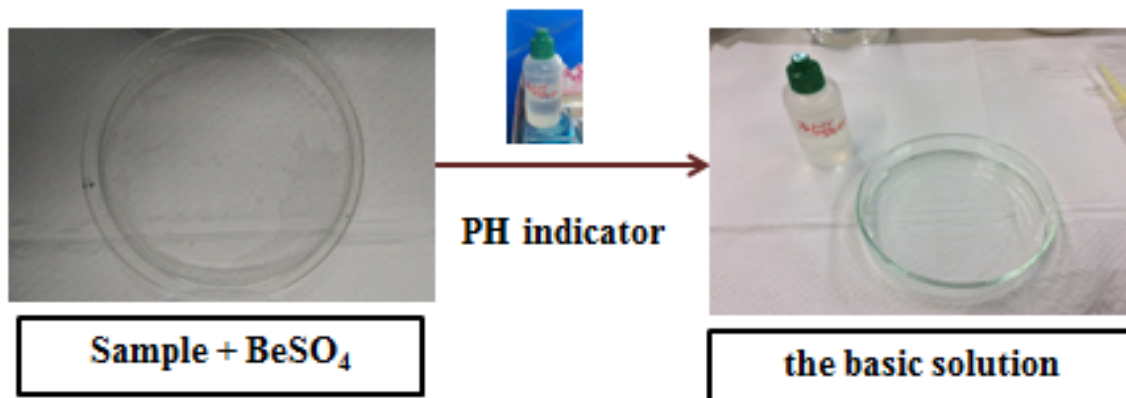


Fig. 2.38 Add several drops of pH indicator (phenolphthalein) to prepare the basic solution

3. Add ammonia water until the solution gives the familiar pink color. At this moment, Be(OH)₂ will be formed and radioactive ⁷Be will co-precipitate with non-radioactive Be²⁺.

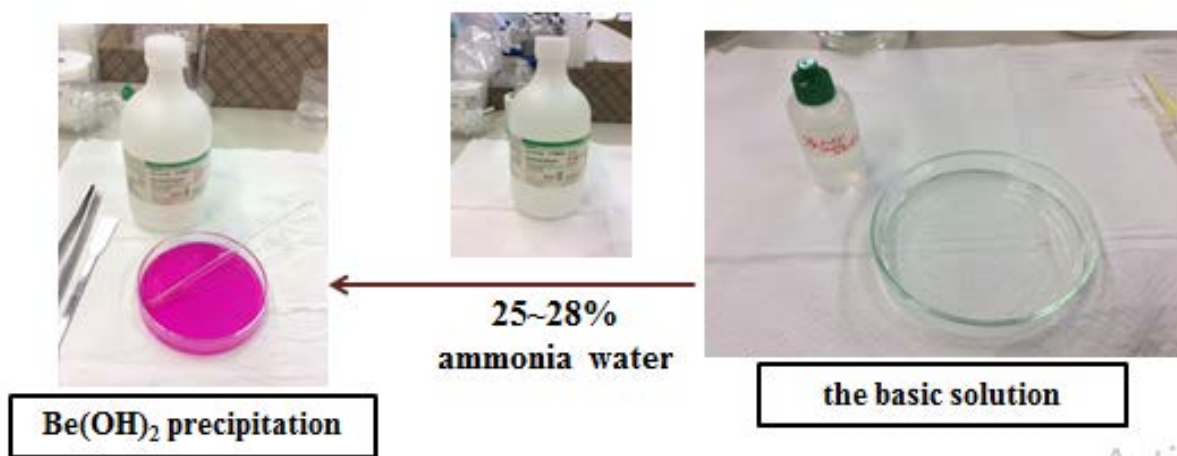


Fig. 2.39 The basic solution sample turn pick color after add ammonia water.

4. Filtrate whole Be(OH)₂ (Beryllium hydroxide)(white color precipitation) with a filter paper, washing with a small volume of distilled water several times by using a policeman.

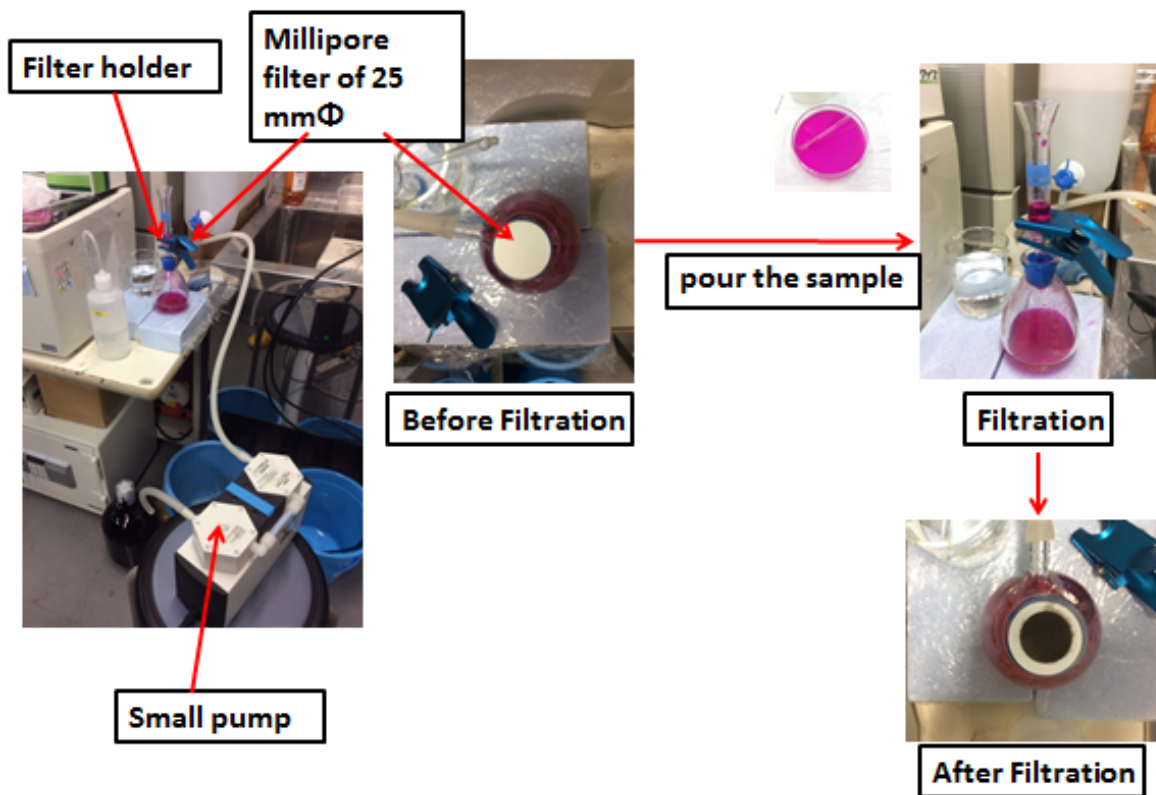


Fig. 2.40 Filtrate the $\text{Be}(\text{OH})_2$ precipitation by vacuum filtration.

5. Make ^7Be -sample for radioactivity measurement by covering filtrated $\text{Be}(\text{OH})_2$ precipitation with an adhesive tape to prevent the precipitate losing shape, and sealed into a plastic bag to prevent the detector from radioactive contamination.



Fig. 2.41 The filter sample the contain ^7Be .

After the measurement of inorganic species concentration and ^7Be concentration, the concentration of the size distribution was calculated the mass median aerodynamic diameter (MMAD) for inorganic species and the activity median aerodynamic diameter (AMAD) for ^7Be , and the Geometric Standard Deviation (GSD), following the equation below.

The MMAD and AMAD divide the aerosol size distribution in half. It is the diameter at which 50% of the particles of an aerosol by mass are larger and 50% are smaller. MMAD and AMAD were calculated from the 2-point interpolation of the data points representing the cumulative mass/activity percent above and below 50%.

The GSD measures the dispersion of particle diameter and is defined as the ratio of the median diameter to the diameter at $\pm 1\text{sd}$ (σ) from the median diameter. In a cumulative distribution plot of the aerodynamic diameter and mass of particles, the GSD is calculated as the ratio of the median diameter to the diameter (d) at 16% of the probability scale, or the ratio of the diameter at 84.1% on the probability scale to the median diameter [9].

$$\text{GSD} = \sqrt{\frac{d_{84\%}}{d_{16\%}}}$$

The percentage of mass with a diameter (dp) less than that indicated by each stage is calculated as follow [10]:

$$\% < dp \text{ (stage } i) = 100 - \sum_{j=1}^i \% \text{mass in stage}$$

The percentage of mass at each stage is calculating by dividing the mass collected in each stage (W_i) by the total mass (W_{tot}), which is the sum of particle masses for all stages including the back-up filter, calculated as follow [10]:

$$\% \text{ mass or activity in each stage (mg or Bq)} = \frac{W_i}{W_{\text{tot}}} \times 100$$

Reference

- [1] I. Radulescu, A.M. Blebea-Apostu, R.M. Margineanu, N. Mocanu, 2013, Background radiation reduction for a high-resolution gamma-ray spectrometer used for environmental radioactivity measurements, Nuclear Instruments and Methods in Physics Research A 715, 112–118.
- [2] D.D. Veerendra, et al. 2011, Background Minimization of HPGe Detector by Passive Graded Shielding, Int. J. Low Radiation 8(4).
- [3] K. Debertin and R. G. 1988, Helmer, *Gamma- and X-Ray Spectrometry with Semiconductor Detectors*, North-Holland.
- [4] NOAA Sunspot Number, <http://www2.nict.go.jp/aeri/swe/swx/swcenter/sunspot.html> (obtained on 2021/01/02).
- [5] Cosmic Ray Station of the University of Oulu, Finland, <http://cosmicrays.oulu.fi/> (obtained on 2021/01/02).
- [6] Daito city hall 大阪府地域大気汚染常時監視測定データファイ <http://taiki.kankyo.pref.osaka.jp/taikikanshi/> (obtained on 2021/1/25).
- [7] National Oceanic and Atmospheric Administration’s Air resources Laboratory (NOAA’s ARL), 2020, U.S. Department of Commerce <https://ready.arl.noaa.gov/HYSPLIT.php> (obtained on 2021/1/29).
- [8] Electronic notes, Electrical Conductivity: mho, siemens, https://www.electronics-notes.com/articles/basic_concepts/resistance/electrical-conductivity-conductance.php#:~:text=The%20electrical%20conductivity%20units%20are,the%20reciprocal%20of%20one%20ohm., (obtained on 2020/11/30).
- [9] William C. Hinds, 2012, 2nd Edition, *Aerosol Technology: Properties, Behavior, and Measurement of Airborne Particles*, ISBN: 9781118591970.
- [10] Araceli Sánchez Jiménez, Karen S Galea, Robert J Aitken, June 2011, Guidance for collection of relevant particle size distribution data of work place aerosols Cascade Impactor Measurements, IOM’s report: TM/09/04.

CHAPTER THREE

RESULTS AND DISCUSSION

3.1 Air dust

3.1.1 Ruthenium-106 (^{106}Ru) measurement

Ruthenium-106 (^{106}Ru) is a pure beta-minus emitter with a half-life of 371.5 days. It decays to the ground state of rhodium-106 (^{106}Rh). The half-life of ^{106}Rh is only 30.1 seconds so in any sample measured in a laboratory; there should be secular equilibrium between ^{106}Ru and ^{106}Rh after only a few minutes. This means that they decay at the same rate and have the same activity¹. Rhodium-106 (^{106}Rh) is also a pure beta-minus emitter, but in contrast to its parent, its decay is followed by emission of gamma-rays from de-excitations of its daughter-nucleus ^{106}Pd . These gamma-rays can be used for detecting ^{106}Rh , and consequently also indirectly ^{106}Ru , using gamma-ray spectrometry [1]. The decay scheme of ^{106}Rh shows in **Fig. 3.1**. ^{106}Rh emit many gamma energy but the of them have very low grammar emission probabilities There are have only 511.84 and 621.9 keV have high probabilities is 20% and 9.93%, respectively But at 511.84 keV very close to Annihilation energy so we can use only 621.9 keV [2].

In term of monitoring, ^{106}Ru measured is an example in this study due to during late September to early October, 2017; several European countries reported that Ruthenium-106 has been detected. Based on the meteorological conditions provided by Météo France and the measurement results, IRSN carried out simulations to locate the release zone. **Fig. 3.2** show the results obtained and confirms that the most possible release zone of ^{106}Ru lies between the Volga liver and the Urals mountains [1].

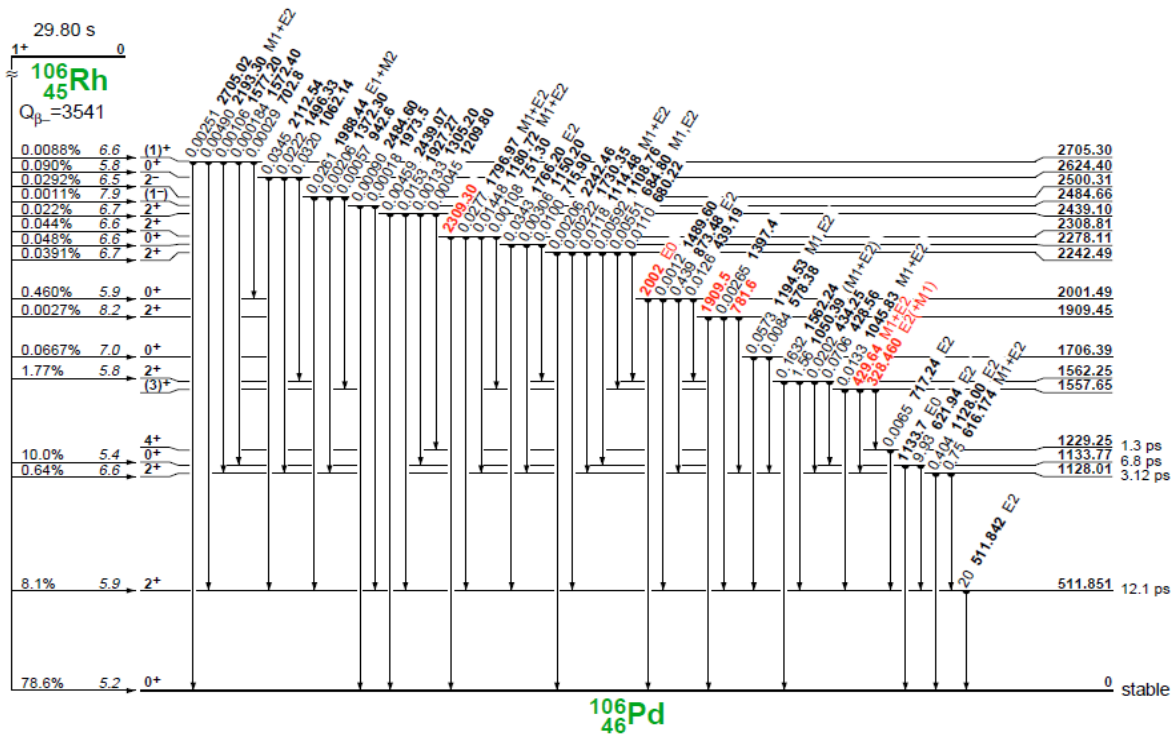


Fig. 3.1 The decay scheme of ^{106}Rh [2].

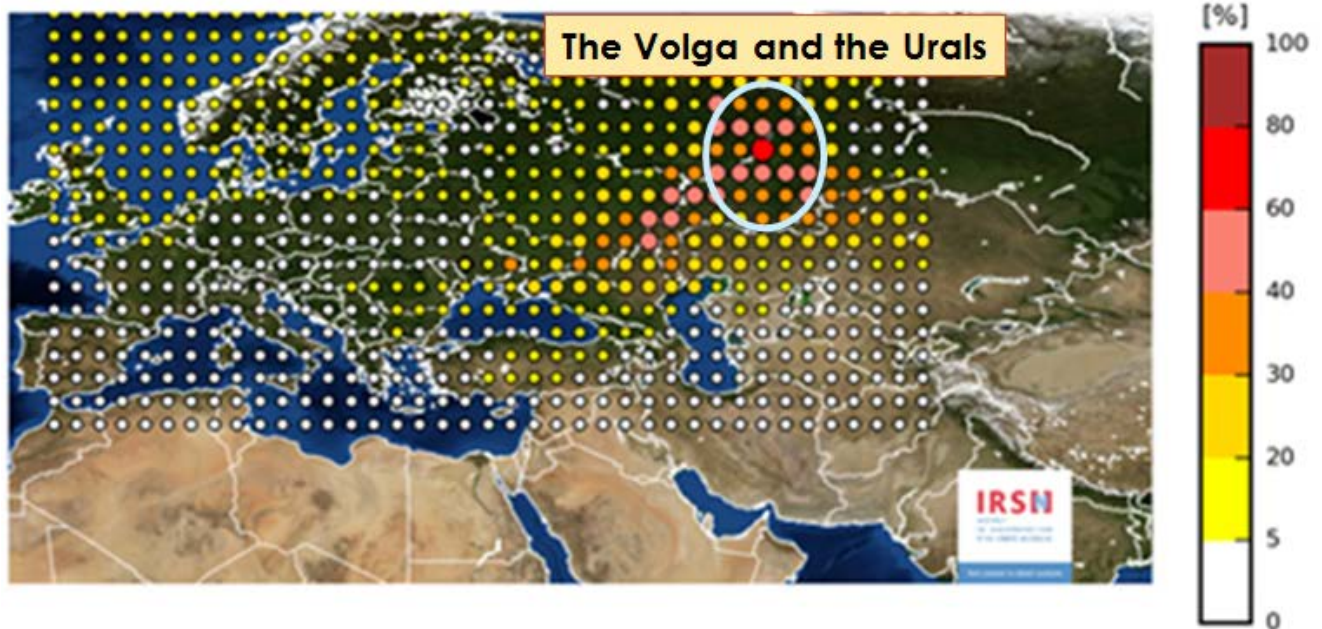


Fig. 3.2 The most possible release zone of ^{106}Ru lies between the Volga river and the Ural mountains [1].

On December 21, 2017, Belgium Nuclear Research center (SCK•CEN) report the journey of ^{106}Ru by simulation. The analysis carried out by Belgium Nuclear Research center (SCK•CEN) and The Royal Meteorological Institute of Belgium (KMI/IRM) experts used transport and atmospheric dispersion models combined with numeric meteorological data from the European Centre for Medium-Range Weather Forecasts (ECMWF) to determine the origin of ^{106}Ru based on measurements taken across Europe and around the world. In **Fig. 3.3**, the result of the analysis is shown. This ^{106}Ru has probably comes from a region in Russia where many nuclear facilities are located [3]. From this result it has probability that ^{106}Ru was transported to Japan in small concentration.

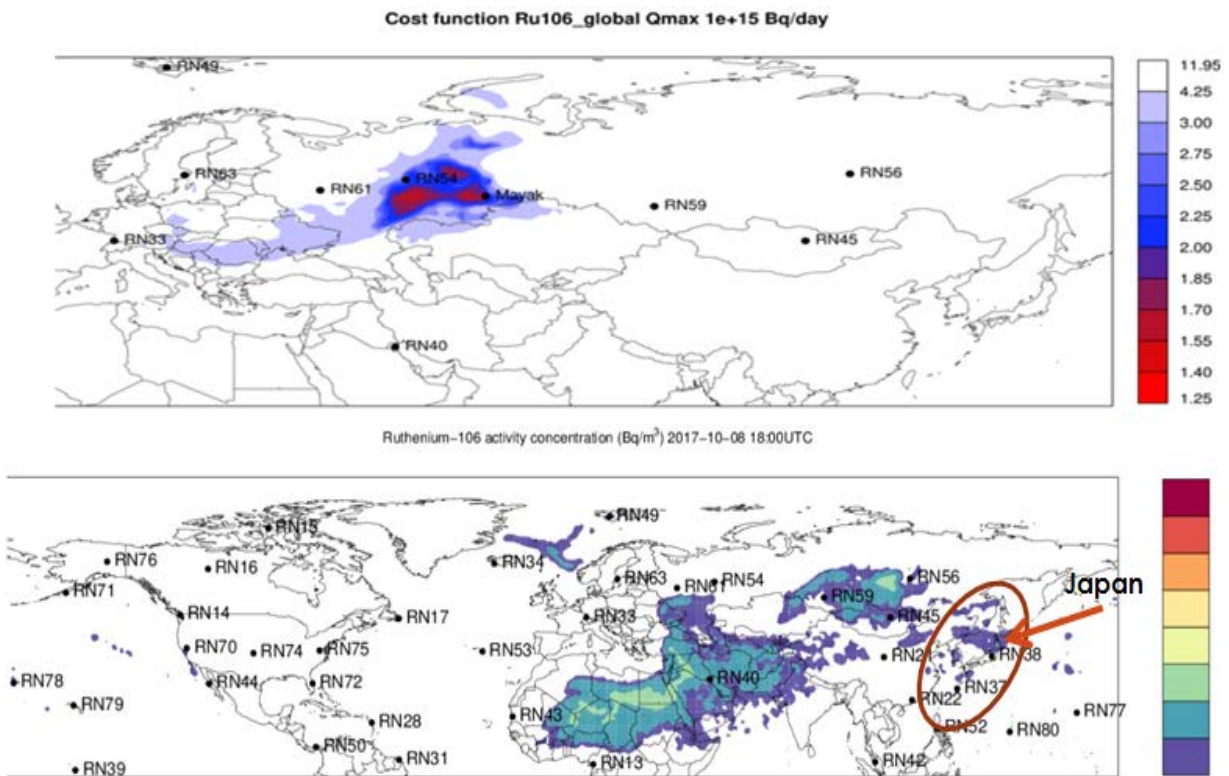


Fig. 3.3 The result of simulation of the journey reported by SCK•CEN [3].

On 16 FEBRUARY 2018 a journalist in Rome public the article, this article mention that based on a computer model from fence and German. ^{106}Ru most likely originated in the southern Urals The southern Urals are home to the Mayak nuclear facility, the scene of one of the world's worst nuclear accidents 60 years ago, and speculation soon turned to a possible accident at its reprocessing plant, which extracts isotopes from spent nuclear fuel. The IRSN report, mention that Mayak's attempt to manufacture a capsule of cerium-144 destined for Gran Sasso "should be investigated" as a possible cause. Scientists of Mayak PA at Gran Sasso needed the cerium for SOX (Short distance neutrino Oscillation) that testing the light sterile neutrinos hypothesis [4].

At our university campus we had been installed the High Volume Air Sampler at the rooftop of building No.16. We continuous to correct the air samples and measure it. We are using Ge Detectors, Model GC2018 made by CANBERRA to measure grammar ray and to confirm our result Prof. Umehara kindly help us to us to measure our sample at Kamioka underground lab by using very low background Ge detector (Model GC5019) made by CANBERRA. **Fig. 3.4** shows the Ge detector (Model GC5019) with its shielding system and background level before and after installed the shielding system.

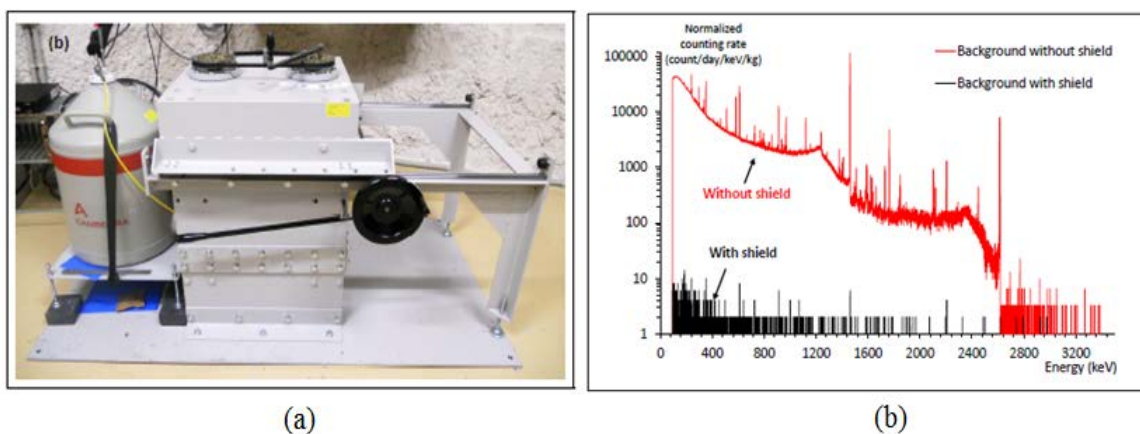


Fig. 3.4 (a) The Ge detector (Model GC5019) with its shielding system and (b) background level before and after installed the shielding system [5].

The weekly sample during October 9 to November 13, 2017 were searched and found small possible peak of ^{106}Rh during the sample collection October 23 – 30, 2017, shows in **Fig. 3.5**.

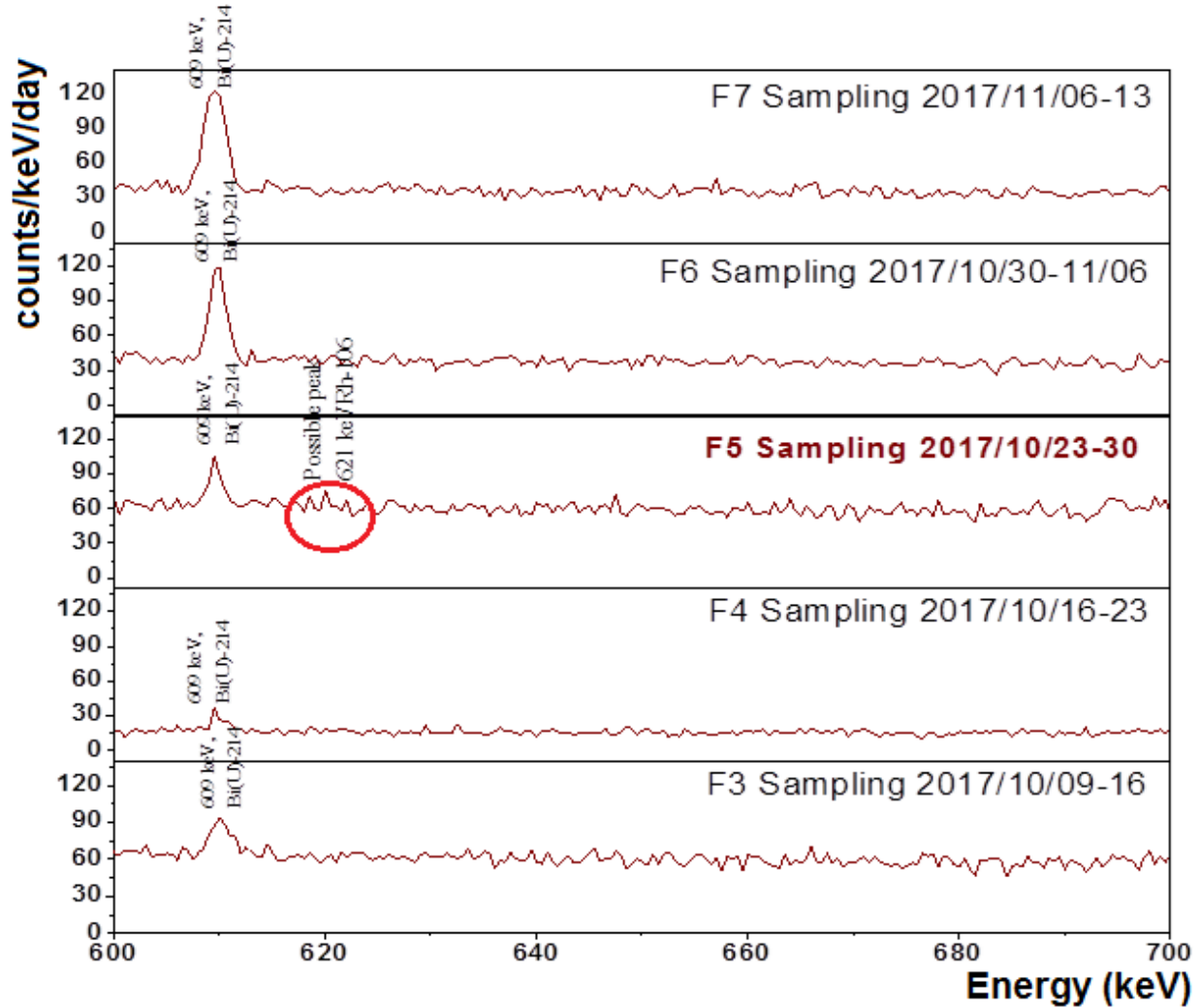


Fig 3.5 The measurement results of our weekly samples during October 9 to November 13, 2017 and the possible peak of ^{106}Rh in the sample collection October 23 – 30, 2017.

The possible peak of ^{106}Ru was found in our sample by using Ge detector (GX2018, CANBERRA) but the counts (24 ± 4 cpd/keV) was smaller than the detection limit at 622 keV (29 ± 5 cpd/keV). So, the possible peak was not identified. To confirm our result, Prof. UMEHARA Saori, Osaka University helps us to measure it at Kamioka Underground Lab. by using very low background Ge detector (GC5019, CANBERRA). **Fig 3.6** shows the result of the background at

Kamioka Underground lab (KM) very low when compared with Osaka Sangyo University (OSU).

Fig 3.7 shows the comparison between measurement at out lab in OSU and KM but the counts (1.53 ± 1.20 cpd/keV) was smaller than the detection limit at 622 KeV (2.20 ± 1.48 cpd/keV). The possible peak was not found. It's maybe the source of ^{106}Ru is quit far from Japan and the concentration very small among when ^{106}Ru was transport to Japan. Thus, ^{106}Ru was not observed in Osaka. However, ^{106}Ru was not found in this area, this system is still important in term of the monitoring during the any nuclear test, nuclear, and radiation accident.

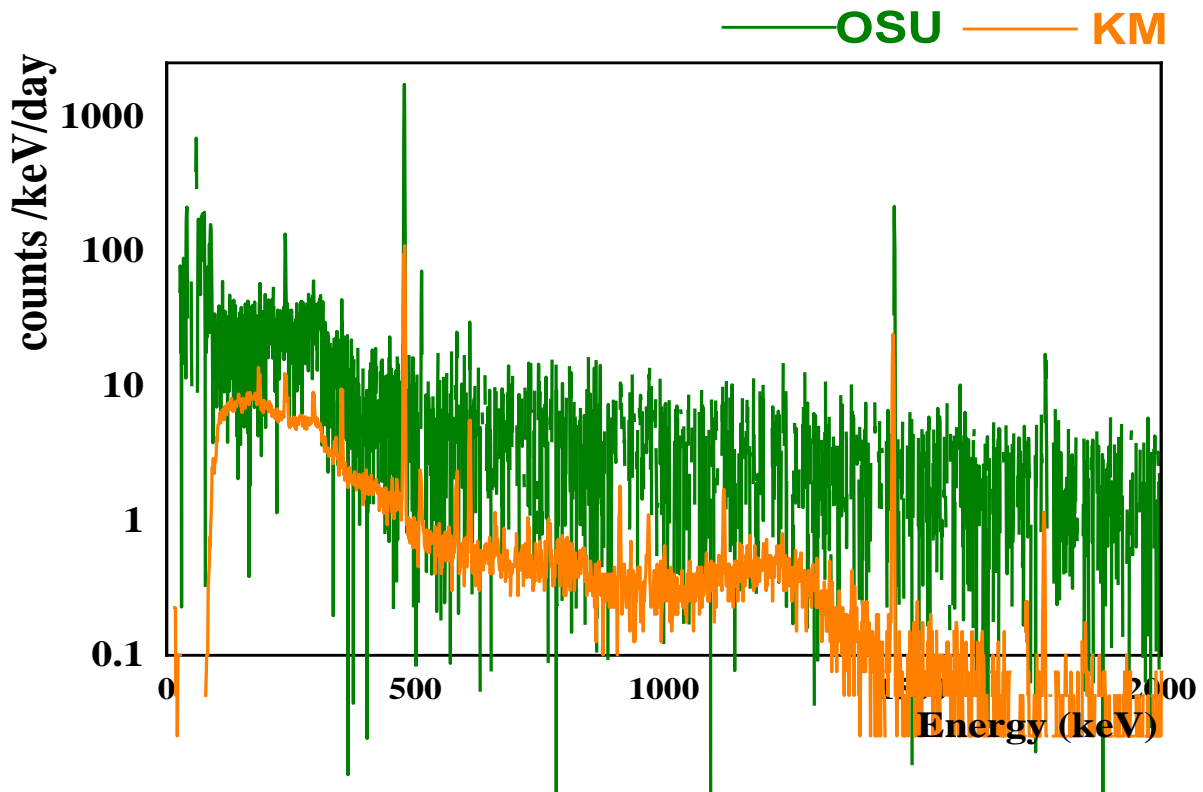


Fig 3.6 The result of the background at Kamioka Underground lab (KM, measurement time: 154 h) very low when compared with Osaka Sangyo University (OSU, measurement time: 72 h).

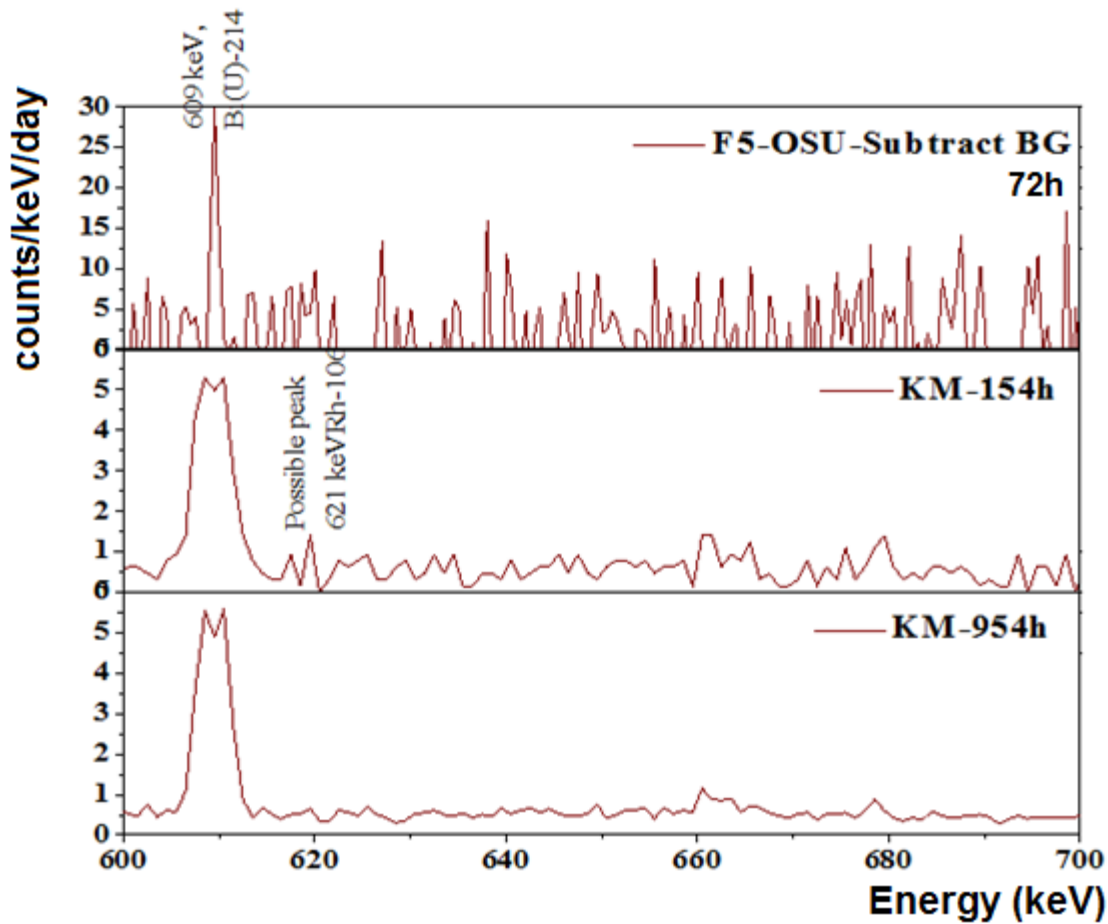


Fig. 3.7 The comparison between measurement at out lab in OSU and KM, the sample collection October 23 - 30, 2017.

3.1.2 ^7Be and ^{210}Pb concentration

In **Fig. 3.8** are shown the seasonal variation in surface air concentration of ^7Be at Daito, Osaka in 2018 - 2020 and comparing with our previous data in 2015 [6] and 2016 [7], and the long term data from 1993 to 1997 at Sakai, Osaka, which was reported by K. Megumi, et al. 2000 [8]. All data of the monthly average concentration of ^7Be in surface air at Osaka show the same trend and clearly showing maxima in spring and autumn and minima in summer. This tendency, two-peak variation pattern, found at Osaka is almost in agreement with other observations in Japan such as Nagano [9] and Yamagata [10]. The general aspect of the seasonal variations in

Japan can be interpreted that in spring and autumn, the moving high-pressure, which includes stratospheric air containing high concentrations of ^7Be carried into the troposphere, passes through from West to East [9]. On the other hand, in summer the air masses are transported from the subtropical high-pressure zone or low latitudes, which are carrying low ^7Be concentrations into the middle latitude region [8]. In each season the transient meteorological situations such as horizontal transport and moving of air masses would cause temporal changes in surface air concentrations of ^7Be [9].

Monthly averages of the atmospheric concentrations of ^7Be and ^{210}Pb are shown in **Fig. 3.9** and annual cycle shows in **Fig. 3.10**. The ^{210}Pb concentration in the air at Daito ranged from 0.42 to 1.9 mBq/m³ with an average of 0.78 mBq/m³ through the sampling period. The ^7Be concentrations in the air in Daito ranged from 2.15 to 8.84 mBq/m³, and an average was 5.03 mBq/m³. K. Megumi et al., 2000 [8] reported 6.06 mBq/m³ of ^7Be atmospheric concentration as an average during the period from 1983 to 1997 and ranged from 3.05 to 7.65 mBq/m³, which was comparable to the present observation in Daito. The atmospheric concentrations of ^7Be and ^{210}Pb revealed a clear seasonal variation, the ^7Be and ^{210}Pb concentrations have increased in autumn and spring, and decreased in summer. Similar seasonal variations with strong correlation ($CC = 0.68$) were observed in the activities for unit weight of aerosol, however, they showed more pronounced decreases on June and July 2018 than the corresponding atmospheric concentrations. The atmospheric ^7Be and ^{210}Pb concentrations show a seasonal variation, which makes us speculate on a change of ^7Be and ^{210}Pb sources in summer.

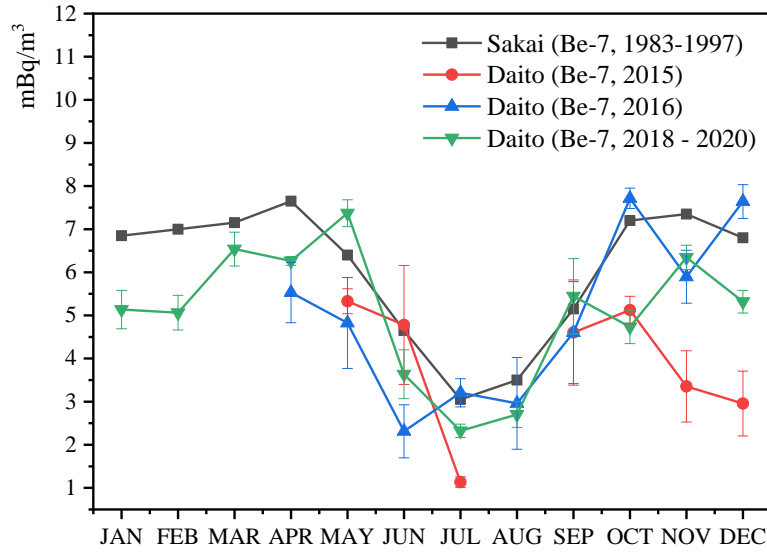


Fig. 3.8 ^7Be concentration data at Daito Osaka in 2018 – 2020 compare with our previous data in 2015 [6] and 2016 [7], and the long term data from 1993 to 1997 at Sakai [8].

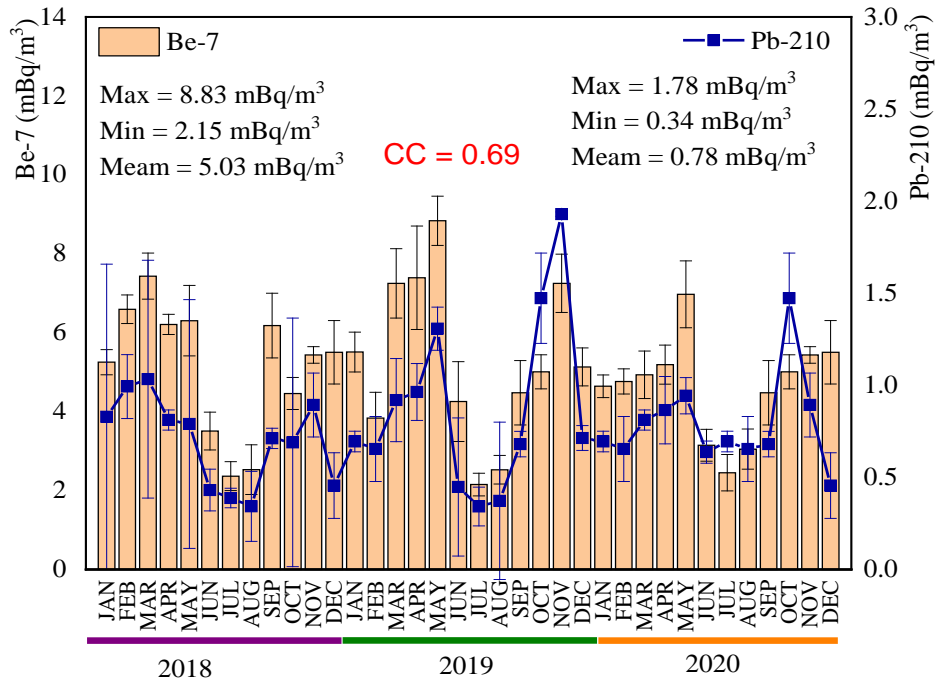


Fig. 3.9 ^7Be concentration data at Daito Osaka in 2018 – 2020 compare with ^{210}Pb concentration.

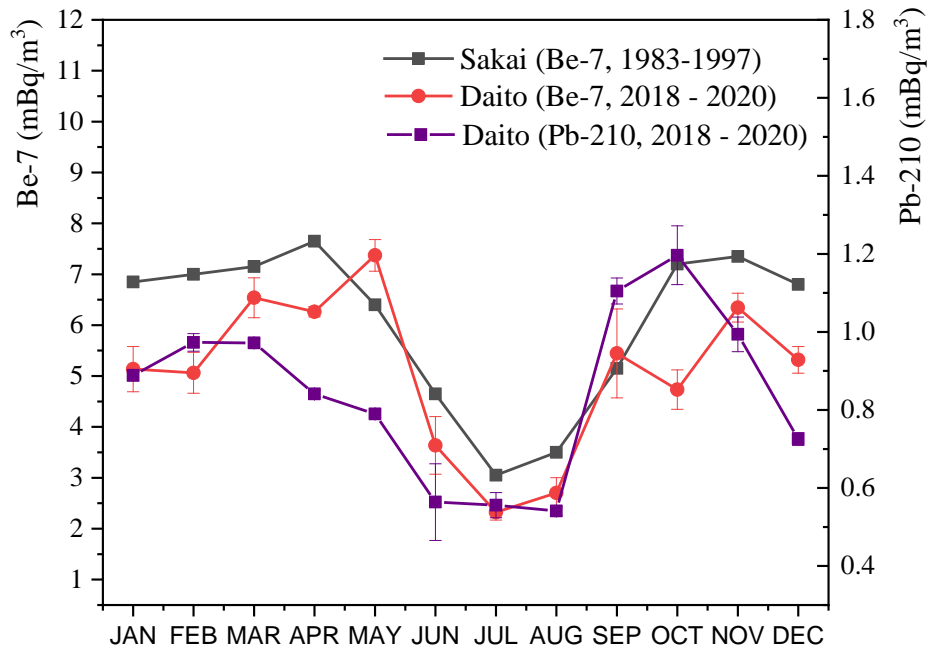


Fig. 3.10 The annual cycle of ^7Be and ^{210}Pb concentration data at Daito Osaka in 2018 ~ 2020, and at Sakai 1983 ~ 1997 [8].

3.1.3. Factors causing variation concentration of ^7Be and ^{210}Pb

In order to obtain information concerning the main mechanism controlling the ^7Be surface concentration, correlation coefficients (CC) were calculated. The relationship or correlation was interpreted following the **Table 3.1**.

Table 3.1 Interpretation of Correlation Coefficient [11].

Coefficient Interval	Correlation
0.00 ~ ± 0.199	Very Weak
± 0.20 ~ ± 0.399	Weak
± 0.40 ~ ± 0.599	Medium
± 0.60 ~ ± 0.799	Strong
± 0.80 ~ ± 1.000	Very Strong

The correlation between the monthly variations of ^7Be concentrations and total suspended particle (TSP), relative humidity, precipitation, sunspot number, cosmic ray intensity, and PM_{2.5} concentration on surface air ^7Be concentrations, the results are shown in **Fig. 3.11**. **Fig. 3.11** (a) shows monthly ^7Be concentration, and **Fig. 3.11** (b) shows the TSP concentration ranged from 26.84 to 54.03 $\mu\text{g}/\text{m}^3$, high concentrations were observed in spring and low in summer. The relationship shows medium positive correlation ($\text{CC} = 0.51$) between ^7Be and TSP concentration. It is known that north-western monsoons from the Asian continent during the season change from winter to spring carry air mass with natural and/or anthropogenic materials from continent to Japanese island. This result means that the main sources ^7Be and particulate matter are upper atmosphere and the troposphere over the Asian continent, respectively [12]. Obviously heavier weight aerosol, 54 $\mu\text{g}/\text{m}^3$ was observed on March and April 2019 as compared to other seasons, 26 $\mu\text{g}/\text{m}^3$ on July and August 2019, 42 $\mu\text{g}/\text{m}^3$ in autumn and spring 2019. The decrease of activity for unit weight could be attributed to dilution by aerosol with less ^7Be and ^{210}Pb activities.

The variation of ^7Be concentrations in near-surface air is commonly associated with meteorological parameters [13, 14, 15]. **Fig. 3.11** (c) and (d) showed the correlation between the concentration of ^7Be in surface air and relative humidity and precipitation, respectively. The negative correlation was observed in relative humidity ($\text{cc} = -0.40$) and precipitation ($\text{cc} = -0.32$). This is due to after production of ^7Be , it reacts with air constituents and turns into atoms or ^7BeO or $^7\text{Be}(\text{OH})_2$ molecules, which attached to available aerosol particles. This Isotope condenses on aerosol population, growing by condensation of non-radioactive species [16]. When humidity is higher, their size increases and their residence time in the atmosphere decreases under the influence of gravity, ^7Be resulting in a lower content in the surface air [17] In general, as aerosols are scavenged by rain, it is considered that the ^7Be concentrations are in low level at the large amount of precipitation, it mean that ^7Be concentration on the atmosphere was washout by rain

[9]. From the correlation coefficient value, we found that relative humidity has stronger relation with ^7Be concentrations than precipitation. Note that, high humidity leads to faster aerosol deposition, thus removing adsorbed ^7Be from the surface atmosphere [15]. However, a correlation was not strong enough in both relative humidity and precipitation. Therefore, in addition to the local meteorological effect it is necessary to investigate the transport processes of ^7Be on global scale. The air masses motions were estimated by using the HYSPLIT model to simulate the backward trajectories during the period from January 2018 to December 2020.

The correlation between ^7Be concentration and PM_{2.5} is shown in **Fig. 3.11** (e). We found a weak positive correlation ($CC = 0.30$) and it is agreed with our previous study in 2015 ($CC = 0.38$) and 2018 ($CC = 0.33$) [18]. However, the correlation between ^7Be concentration and PM_{2.5} did not significantly change with the correlation data only 3 year periods. **Fig. 3.11** (f) The sunspot number ($CC = -0.17$) and (g) neutron intensity ($CC = 0.02$) from cosmic ray shows very weak correlation in both factors. These two factors affect the production rate of ^7Be at the upper atmospheres. However, it should be noted that the temporal ^7Be concentration variation was not influenced by the sunspot number and neutron intensity because this study the period is short when compare with the solar cycle (11 years).

For the further confirmation, a longer sampling period should be required, not only for the relation with rainfall, and PM_{2.5} but also for the relation with sunspot number, and cosmic ray intensity and we will study more.

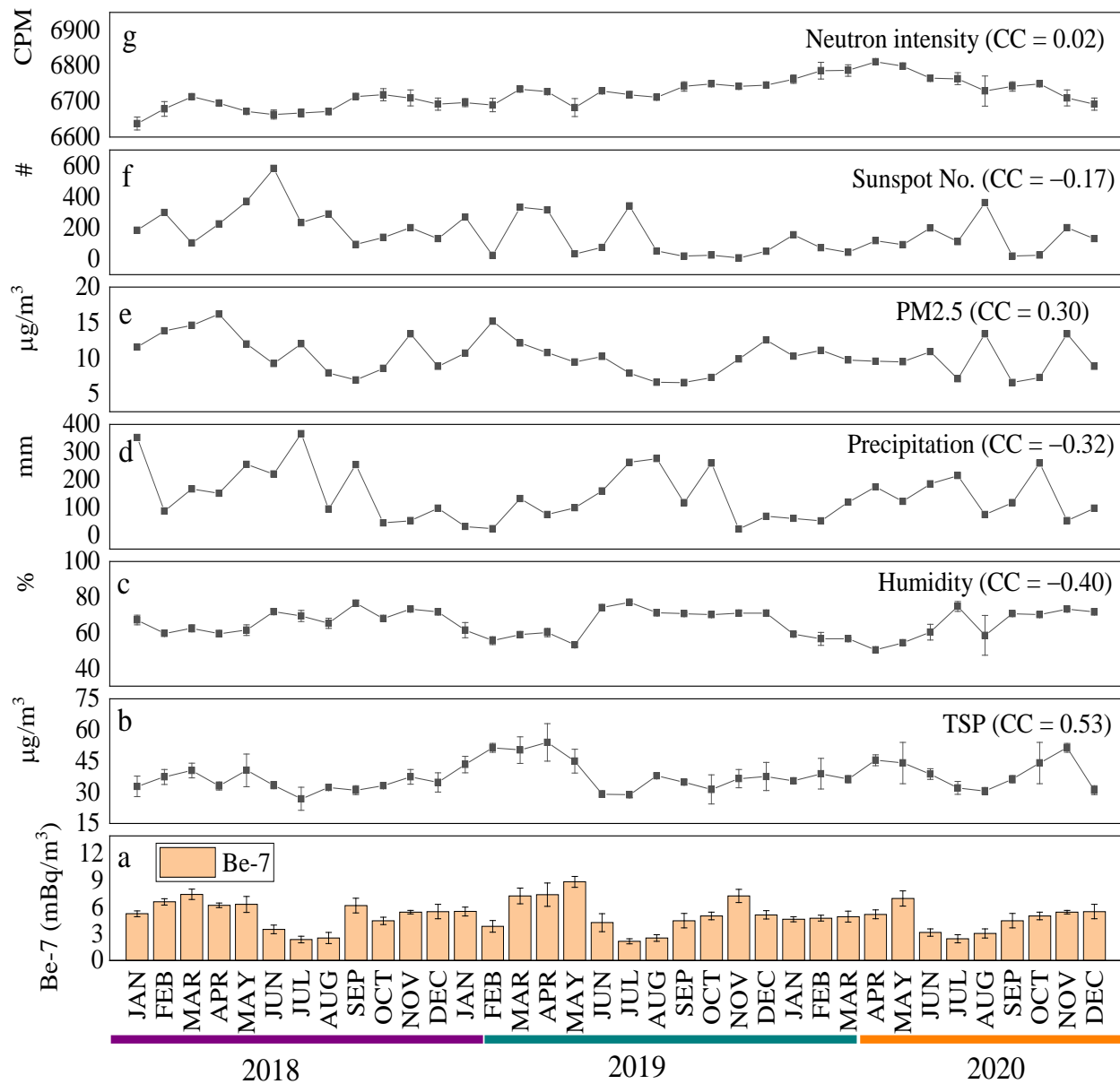


Fig. 3.11 Correlation between weekly variations of ^7Be concentrations in surface air (a) and TSP (b) relative humidity (c), precipitation (d), PM_{2.5} (e), sunspot number (f), and cosmic ray intensity (g).

Correlation coefficient (CC) was calculated between the weekly variations of ^{210}Pb concentrations and TSP, pressure, wind speed, precipitation, relative humidity, and PM_{2.5}. The results are shown in **Fig. 3.12**. **Fig. 3.12** (a) shows monthly ^{210}Pb concentration, and **Fig. 3.12** (b)

shows the TSP concentration shows strong positive correlation ($CC = 0.63$). The result show the high concentration in spring, and autumn and low in summer The high concentration of TSP in spring was observed in this area and this pattern also reported by Fang et al. [19], in Seoul, Korea during 1996 – 2006, Kanai et al. [20], in China and Japan, 2002, and Akata et al. [21], in Tsukuba, Japan. 2002. In spring, the strong dust events brought soil particles from arid and semi-arid regions of continent to Japan caused the high concentration of TSP and ^{210}Pb . [21]. **Fig. 3.12** shows the weak negative correlation was found in pressure (c) ($CC = -0.27$), wind speed (d) ($CC = -0.25$), precipitation (e) ($CC = -0.25$), and relative humidity (f) ($CC = -0.23$). **Fig. 3.12** (g) shows very weak correlation between the ^{210}Pb concentration and $\text{PM}_{2.5}$ ($CC = 0.12$). The results show no relationship between $\text{PM}_{2.5}$ and temporal ^{210}Pb concentration variation.

The negative correlation was found in meteorological condition. In general, Daito is often covered with a high pressure in summer developed in the Pacific Ocean, this situation would give low atmospheric ^{210}Pb concentration by a reduced supply of ^{222}Rn associated with low concentration of ^{226}Ra in seawater, while in fall and winter anticyclones come to Japan from northwest through continental Asia in which much larger ^{210}Pb concentrations were contained by an increased supply of ^{222}Rn from the ground. The change of meteorological condition in summer and other seasons is also possible to affect the atmospheric ^{210}Pb concentration at Daito.

In general, as aerosols are scavenged by rain, it is considered that the ^7Be and ^{210}Pb concentrations are in low level at the large amount of precipitation [9, 23]. However, a weak negative correlation between the ^7Be and ^{210}Pb concentrations and precipitation was observed. Therefore, in addition to the local meteorological effect it is necessary to investigate the transport processes of ^7Be and ^{210}Pb on global scale. The air masses motions were estimated by using the NOAA HYSPLIT model to simulate the backward trajectories during the period from January 2018 to December 2020.

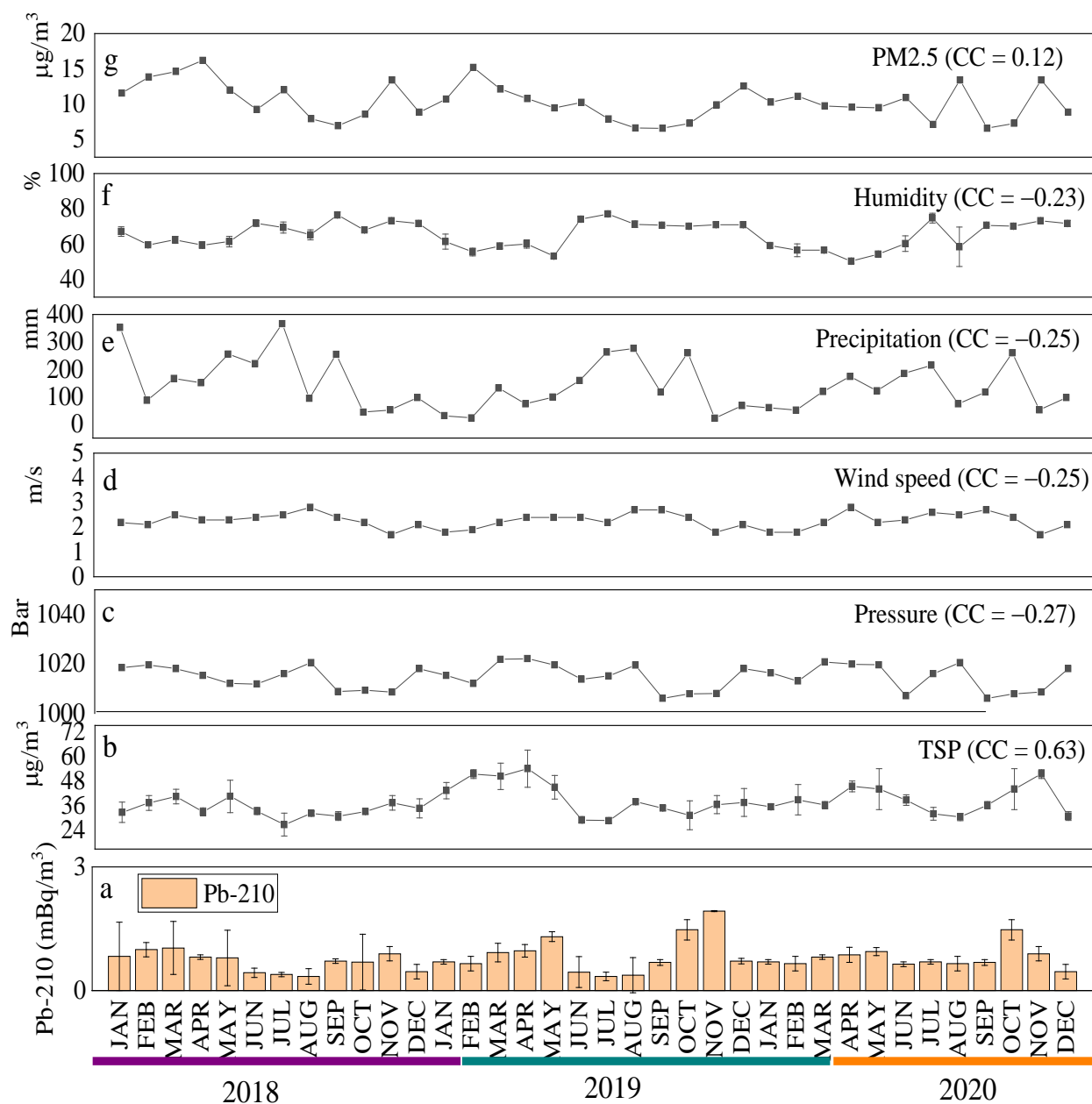


Fig. 3.12 Correlation between weekly variations of ^{210}Pb concentrations in surface air (a) and TSP (b), pressure (c), win speed (d), precipitation (e), relative humidity (f), and PM2.5 (g).

3.1.4 Backward air mass trajectories by using HYSPLIT simulation.

Fig. 3.13 shows the identification of the direction of air masses transport provided by the NOAA HYSPLIT model. The air masses transport is identified by the direction of the trajectory. In this study, the backward trajectories, which can estimate the origin of air masses located at any given place and time, were analyzed [24]. For example, if the data show a direction from N-NW or W-NE, it indicates that the air mass comes from the North-Northwest or West-Northwest, respectively; therefore, the origin of the air mass is located on the Asian continent. The direction from S-SE or S-SW denotes that the air mass comes from the South-Southeast or South-Southwest, respectively.

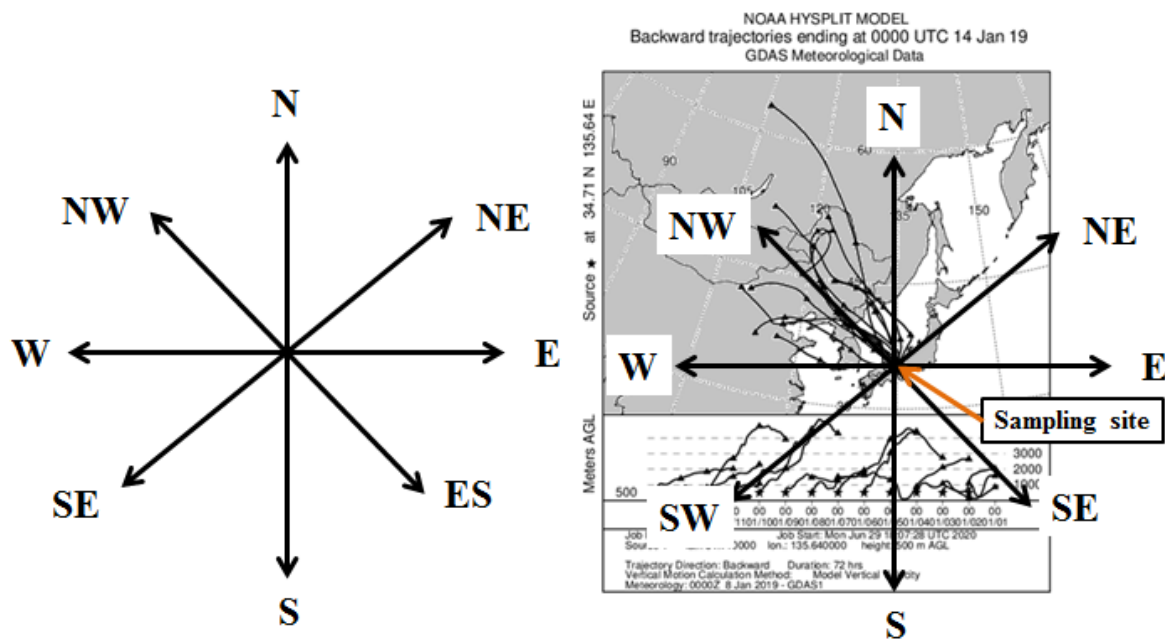


Fig. 3.13 Identification of the air masses transport by the NOAA HYSPLIT model.

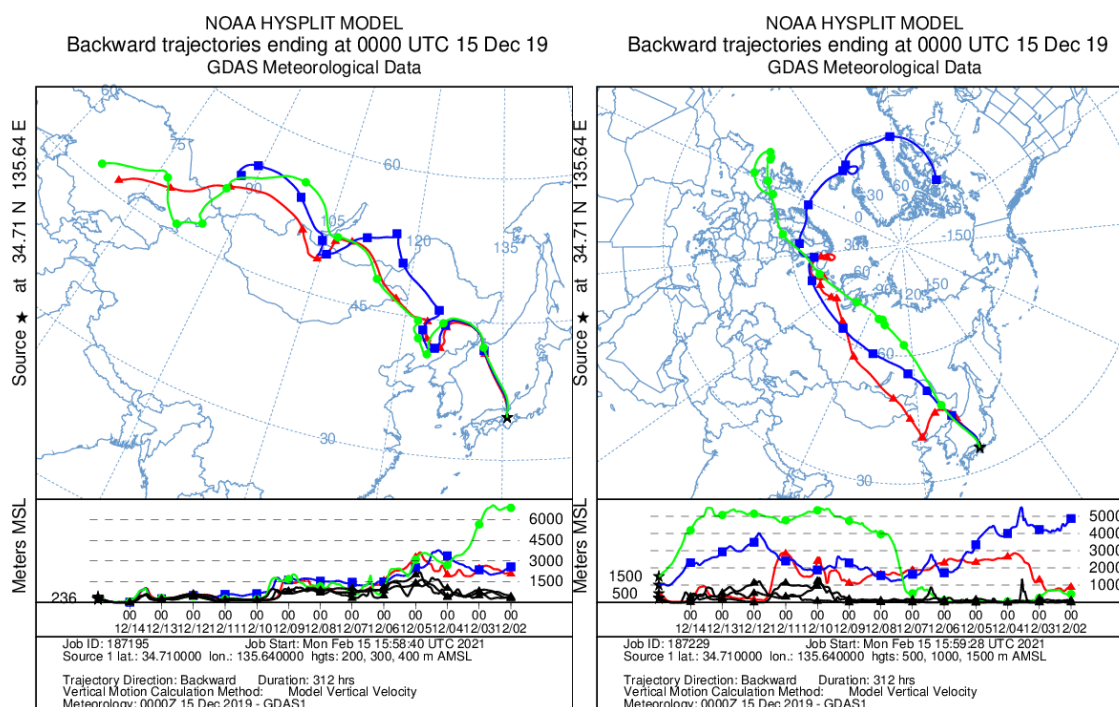
We analyzed the back trajectory of air mass motion using HYSPLIT [24]. In this simulation, the meteorological data set GDAS1 (Global Data Assimilation System) was provide by the NOAA's Air resources Laboratory (ARL). The 72 hours duration back trajectories were

calculated for every 24 hours during the sampling period for each weekly sample. The endpoint of trajectories was set at the sampling site, with the height of 200 m, 300 m, 400 m, 500 m, 1,000 m, and 1,500 m for ^{210}Pb and the high of 2,000 m, 6,000 m, and 20,000 m above mean sea-level (MSL) for ^7Be . These heights are chosen because ^{210}Pb is the decay products of ^{222}Rn from the ground. At very low altitude (200 m, 300 m, and 400 m) and the study of air motion in the atmospheric boundary layer, which is the seat of atmospheric turbulence that strongly influence the meteorology and dispersion (approximately lower 1500 m) should be analyzed. The higher altitude they allow the study the troposphere where occurs the long-range transport of aerosols (2,000 m, and 6,000 m) and the border between the troposphere and the stratosphere, which is the level of ^7Be production (20,000 m).

At very low altitude (200 m, 300 m, and 400 m) and the altitude that strongly influence the meteorology and dispersion (500 m, 1,000 m, and 1,500 m), the examples of the backward trajectories over Daito, Osaka are shown in **Fig. 3.14**. In summer, the air mass direction almost came from East-North and East-South. The air mass origin almost transports from the Pacific Ocean.

Measurements are scarce in the oceanic zones and are taken on island sites. The low concentration values reflect the absence of ^{210}Pb sources in the oceanic areas. The air mass origin in summer show good agreement with the reported by, the frequencies of trajectory endpoints in the sea area increased in summer when atmospheric ^{210}Pb concentrations were low. Small numbers of trajectories passed through the southeastern Asian Continent area and the other area [12]. In winter, spring, and autumn the air mass direction almost came from North-West. The air mass origin almost transports from the Asia continent or east of China. It shows the high concentration of ^{210}Pb . This high-value results from the large proportion of continental areas at these latitudes, compared with oceanic areas, in relation to the rest of the world [25], When ^{210}Pb

concentration was high (highest period: March to May), the air-mass had been transported from the continental inland area. On the other hand, when it was low (lowest period: June to August, summer season), the air-mass had been mainly coming from the Pacific Oceanside. The amount of ^{210}Pb concentration depends on the surrounding surface of the earth and the possibilities for exhalation of ^{222}Rn . The exhalation over sea is small due to the low concentration of ^{226}Ra in seawater. This is cause the low ^{210}Pb concentration over the sea.



(a1)

(a2)

Fig. 3.14 (a1, 2)

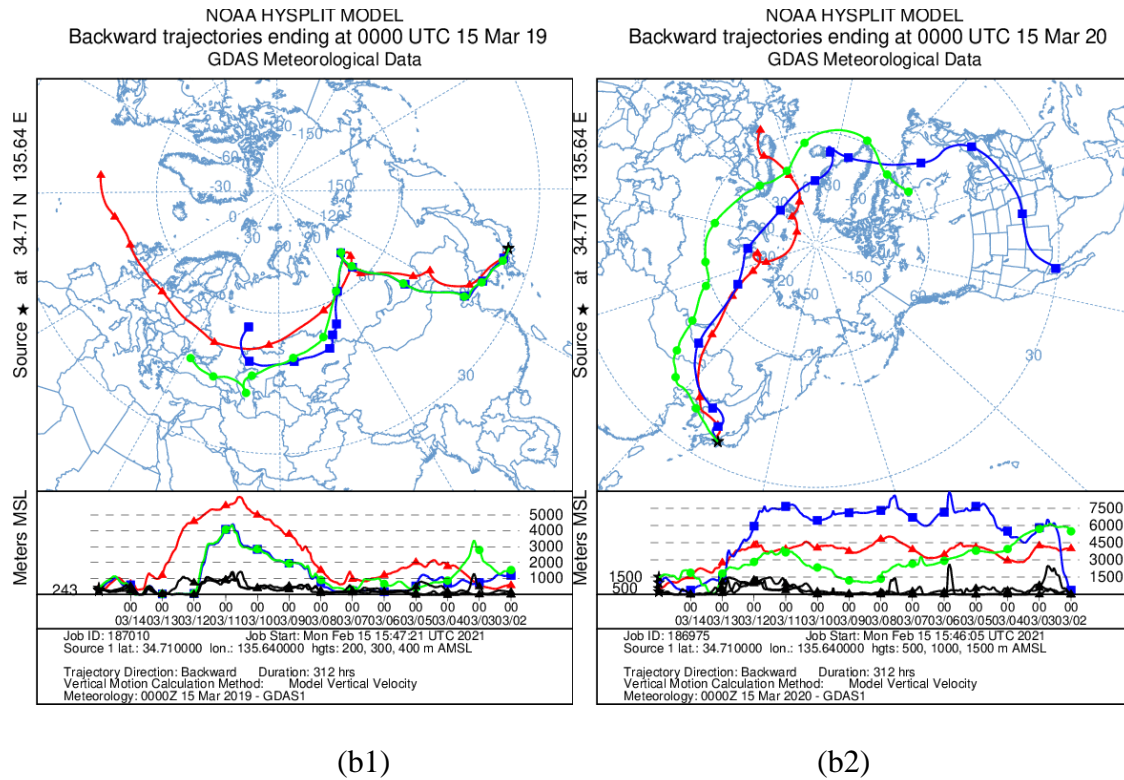


Fig. 3.14 (b1, 2)

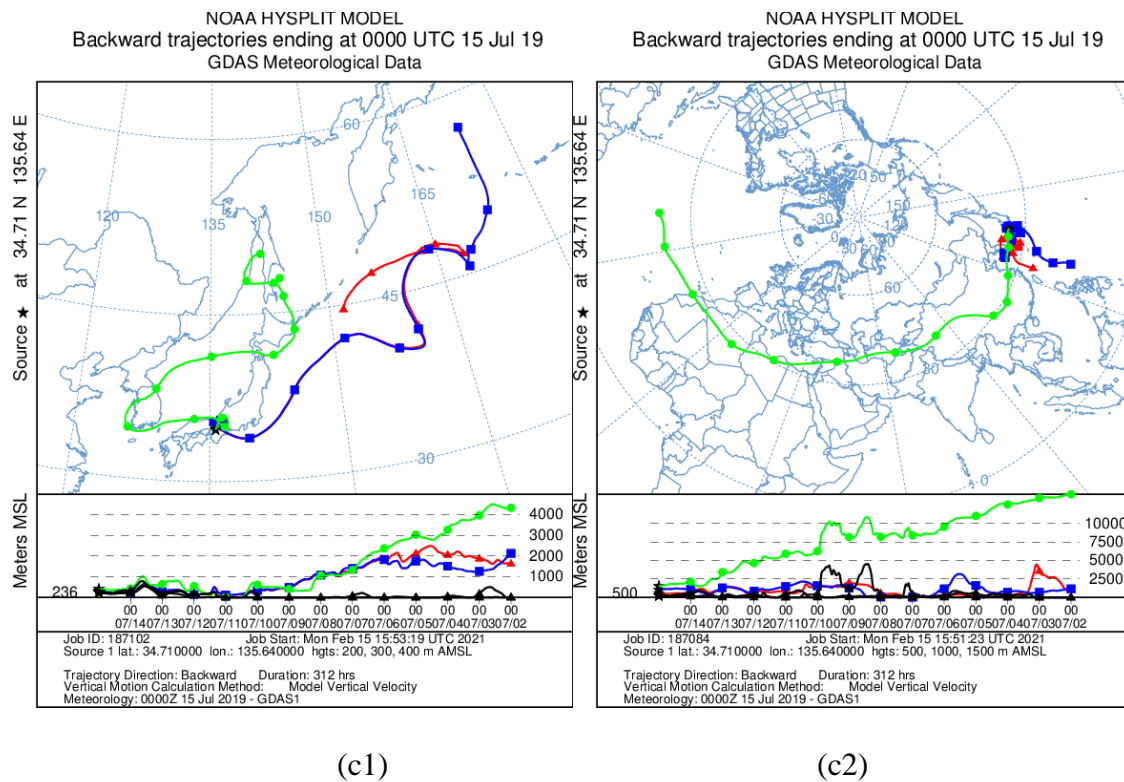


Fig. 3.14 (c1, 2)

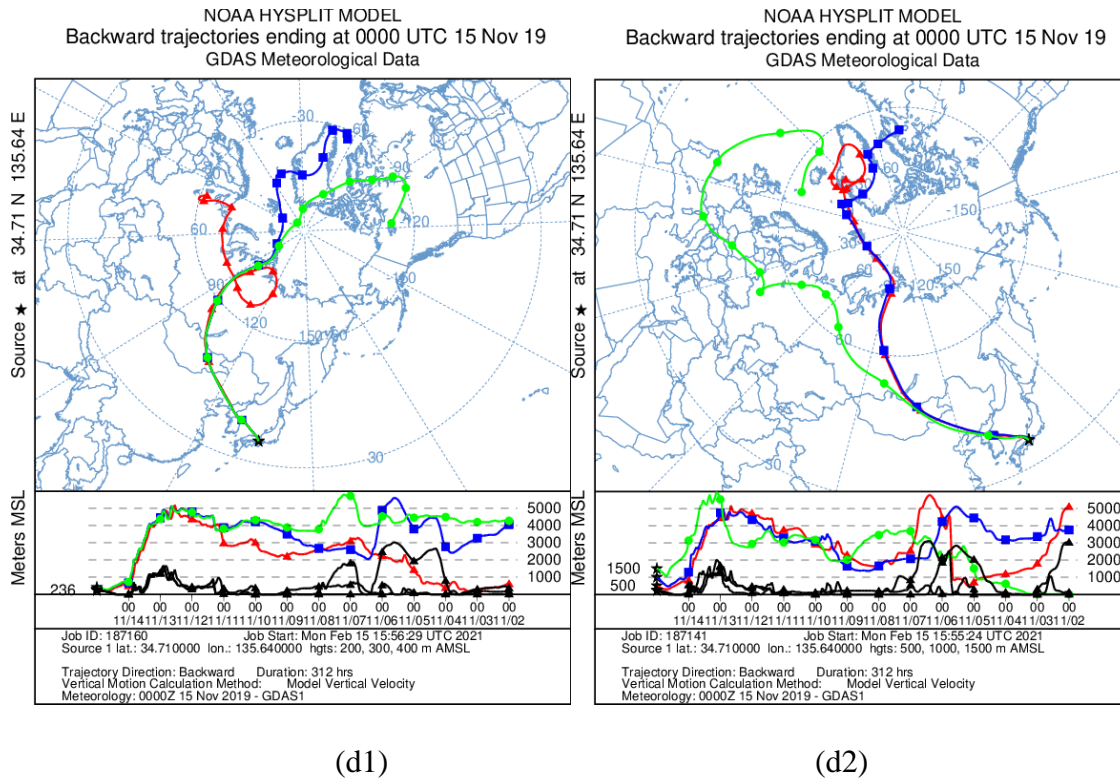


Fig. 3.14 The examples of the 72 hours duration back trajectories by HYSPLIT analysis (NOAA's ARL., 2020) ending at 00.00 UTC, 2,00 m and 500 m (red), 300 m and 1,000 m (blue), and 400 m and 1,500 m (green) MSL on the middle of December 2019 (a1) (a2), March, 2019 (b1) (b2), July 2019 (c1) (c2), and November 2019 (d1) (d2), represent winter, spring, summer and autumn, respectively. 1 represent the very low altitude (200 m, 300 m, and 400 m) and 2 represent the altitude that strongly influence the meteorology and dispersion (500 m, 1,000 m, and 1,500 m).

Table 3.2 Results of backward air mass trajectories at very low altitude (200 m, 300 m, and 400 m) and the altitude that strongly influence the meteorology and dispersion (500 m, 1,000 m, and 1,500 m) by HYSPLIT analysis during the period from January 2018 to December 2020.

Season	Month	200, 300, and 400 m		500, 1,000, and 1,500 m	
		Direction	Air transported from	Direction	Air transported from
Winter	Dec.	N-W	Continent	N-W	Continent
	Jan.	N-W	Continent	N-W	Continent
	Feb.	N-W	Continent	N-W	Continent
Spring	Mar.	N-W	Continent	N-W	Continent
	Apr.	N-W, W	Continent	N-W	Continent
	May.	N-W	Continent, Ocean	N-W	Continent
Summer	Jun.	E, E-ES	Ocean	E-EN, E-S	Ocean
	Jul.	N-E, S-E	Ocean	NE-SE	Ocean
	Aug.	S-E	Ocean	NE-SE	Ocean
Autumn	Sep.	N-W	Continent	S-W, SE-S	Continent, Ocean
	Oct.	N-W	Continent	NW-NE, N-W	Continent
	Nov.	N-W, W	Continent	N-W	Continent

At 2,000 m and 6,000 m, the examples of the backward trajectories over Daito, Osaka are shown in red line, and blue line, are shown in **Fig. 3.15**, respectively. We found that the air masses were transported from the same direction on every month. Japanese island which located at the middle latitude, the air mass from the continent and high latitude carry the higher concentration of ^7Be than the ocean and low latitude [26]. The trajectories in summer passed over the Pacific Ocean and lower latitude. These results confirmed that in summer, the air masses are transported from the subtropical high-pressure zone, which stagnates over the tropical sea or in low latitude areas carrying low ^7Be concentrations into the middle latitudes region [8]. While those in winter, spring, and autumn almost transited through the eastern part of the Asian Continent. The origin

of air masses transported from eastern and northern China for winter and autumn, from eastern and northern China, and far eastern part of Russia for spring. In May 2019 we observed the highest ^7Be concentration at Daito Osaka. The origin of air masses transported from the far eastern part of Russia and the Pacific Ocean. The maximum mixing of stratospheric and tropospheric air masses at mid-latitudes usually occurs in spring when the ^7Be usually reaches higher concentrations than other season and at the far eastern part of Russia, the high ^7Be concentration usually observed in spring due to the monsoon nature of the regional climate, the vertical mixing of tropospheric and stratospheric air, which is transported to the Far Eastern region, leading to high ^7Be concentrations in the region [15] and was transported to Japanese Island which located at the mid-latitudes region.

At 20,000 m MSL in green line, the examples of the backward trajectories over Daito, Osaka are shown in **Fig. 3.15**. We found that the air masses were transported from the same direction with 2000 m and 6000 m only in winter. For spring, summer, and autumn trajectories do not follow the seasonal variability described above. They have directional changes that occur in the same period. The trajectories passed over the Pacific Ocean and the Asian Continent, the direction North-West was observed throughout the year although the occurrence of these winds varies from one month to another.

From the **Table 3.3** in summer, the direction of the air mass transportation at the height 2000 m and 6000 m MSL is totally different from the height 20000 m MSL, it is also transport from the Continent and the higher latitude, which contain the high ^7Be concentration but in this season the low ^7Be concentration was observed. Indeed, in summer, trajectories mostly come from south or Pacific Ocean at the lower MSL (lower than 2000m). In winter, the directions of the air mass transportation are the same at the height 2000 m and 6000 m and 20000 m MSL.

Table 3.3 Results of backward air mass trajectories at 2,000 m, 6,000 m, and 20,000 m MSL by HYSPLIT analysis during the period from January 2018 to December 2020.

Season	Month	2,000 m		6,000 m		20,000 m	
		Direction	Air transported from	Direction	Air transported from	Direction	Air transported from
Winter	Dec.	N-W	Continent	N-W	Continent	N-W	Continent
	Jan.	N-W	Continent	N-W	Continent	N-W	Continent
	Feb.	N-W	Continent	N-W	Continent	N-W	Continent
Spring	Mar.	NW-NE	Continent	NW-NE	Continent	N-W, SE-W	Continent, Ocean
	Apr.	N-W	Continent	N-W	Continent	N-W, SE-W	Continent, Ocean
	May.	N-E	Continent, Ocean	N-E	Continent, Ocean	N-W, S-W	Continent, Ocean
Summer	Jun.	E-SE, S-SW	Ocean	E-SE, S-SW	Ocean	N-W, S-W	Continent, Ocean
	Jul.	S-E, S-W	Ocean	S-E, S-W	Ocean	N-W, SE-SW	Continent, Ocean
	Aug.	S-E	Ocean	S-E	Ocean	SE-ES, N-W	Continent, Ocean
Autumn	Sep.	NE-E, SE-S	Continent, Ocean	NE-E, SE-S	Continent, Ocean	N-W, SW-SE,	Continent, Ocean
	Oct.	NW-NE, N-W	Continent	NW-NE, N-W	Continent	N-W, W-S	Continent, Ocean
	Nov.	N-W	Continent	N-W	Continent	N-W,	Continent

It means that the trajectories show the north-west direction and mostly coming from the higher MSL than in summer, which is in a good agreement with other study at Fukuoka in 2011 [26]. The production rate of ^7Be has a latitude dependency, and has a maximum around 50°N and decreases gradually towards the equator. Considering the latitude of Daito (34.71°N), air masses coming from higher latitude in autumn and spring will have higher ^7Be concentration than those coming from lower latitude in summer.

Transport through atmospheric processes. The second process, which is the transport of ^7Be from the upper troposphere and lower stratosphere region to the surface, is mainly governed by the systematic vertical downward movement taking place within the Hadley-Ferrel Interface Zone (HFIZ), the HFIZ features the downward movement of air masses, while the tropical and polar interface zones feature convergence and upward movements. The HFIZ follows an annual cyclic latitudinal movement due to the pole-ward expansion of the Hadley cell during summer seasons in the respective Hemispheres [27].

3.2 Fallout density

The annual total depositions of ^7Be and ^{210}Pb in Daito were $1655 \pm 26 \text{ Bq/m}^2$ and $284 \pm 7 \text{ Bq/m}^2$ (November 2019 – October 2020), respectively. The present total depositions of ^7Be were within the range of annual depositions observed over Japan: MEGUMI et.al, [8] reported the range from 967 to 1752 Bq/m^2 in Osaka during the 1983 to 1997 period. NARAZAKI et.al, [26] reported the range from 325 to 4936 Bq/m^2 during the 1989 to 1994 period. IGARASHI et.al, [28] reported the range from 876 to 1780 Bq/m^2 in Tsukuba during the 1986 to 1993 period. The annual deposition of ^{210}Pb over Japan was reported by TSUNOGAI et.al. ranged from 167 to 380 Bq/m^2 and HIROSE et al. observed 176 and 182 Bq/m^2 in Tsukuba in 2000 and 2001, respectively, and 234 Bq/m^2 in Nagasaki in 2001. The present data are similar to the above ones. The total deposition of ^7Be increased from February to spring of 2020, showing the highest value in March 2020 and then decreased toward a minimum value in winter (November 2019). The total deposition of ^7Be showed a maximum value on March, July, and October 2020 and then decreased to the minimum value in winter (November 2020). The annual distribution pattern of the total ^7Be deposition at Daito would have two peaks around spring and summer, which continued from the preceding winter. According to the investigation of ^7Be deposition, which was carried out to cover wide regions of Japan, the deposition was classified into 4 patterns. The west part of Sakai, which is a

long term study (15 years) was classified as a region of a spring peak distribution pattern (High in spring) but our result is different that high in summer and spring show in **Fig. 3.16**. Our result is only 1 year period but the annual pattern is a bit different from the long-term study at Sakai. We expected that if we continue to collect to sample for long-term period, the annual pattern will be the same. For short-term in Daito, the different ^7Be deposition patterns between west and east parts of Daito are probably resulted from high mountains located from north to south in Daito and separates Sakai meteorologically [8]. Since ^7Be is of cosmogenic origin its production rate is high in the upper troposphere. On the other hand ^{210}Pb is supplied from ground and thus its production rate is high in the lower troposphere. In spite of quite different sources of ^7Be and ^{210}Pb , similarities of the deposition pattern were reported [29]. The total ^{210}Pb deposition's distribution pattern in **Fig. 3.16** The ^{210}Pb deposition pattern is also a single peak distribution, as in the case of ^7Be . The correlation coefficient between ^{210}Pb and ^7Be depositions was very high ($\text{CC} = 0.85$), suggesting that similar mechanisms controlled the total deposition of ^7Be and ^{210}Pb . It is known that washout occupies a considerable fraction of total deposition. The highest precipitation in regular years appears in July shows the highest concentration of ^7Be and ^{210}Pb .

The range and average of dry and wet depositions are summarized; the dry deposition was obtained by subtracting the wet deposition from the total deposition, shows in **Fig. 3.17**. It is clear that wet deposition is important as a removal process of aerosol, occupying 75.26% for ^{210}Pb and 80.12% for ^7Be . It should be stated that the total deposition on February 2020 was almost explained by the dry deposition. A clear elevation of dry deposition was observed in winter of 2020 (February 2020) that is attributable to two typhoons, which hit Japan Island. The fraction of dry deposition shows a more effective removal of ^{210}Pb (24.73%) than of ^7Be (19.88%) by a dry deposition process. A positive correlation between precipitation and deposition was observed, $\text{CC} = 0.70$ for ^{210}Pb and $\text{CC} = 0.88$ for ^7Be , between maximum wind velocity and dry deposition, indicating that

the dry deposition was certainly enhanced with an increase in wind velocity. The more considerable precipitation-normalized deposition of ^{210}Pb than that of ^7Be in winter would suggest an enormous contribution of dry removal of ^{210}Pb in winter because the wet removal process contributed almost equally for both. The similar result was reported by N. Momoshima, et al., (2006) at Kumamoto, Japan [29].

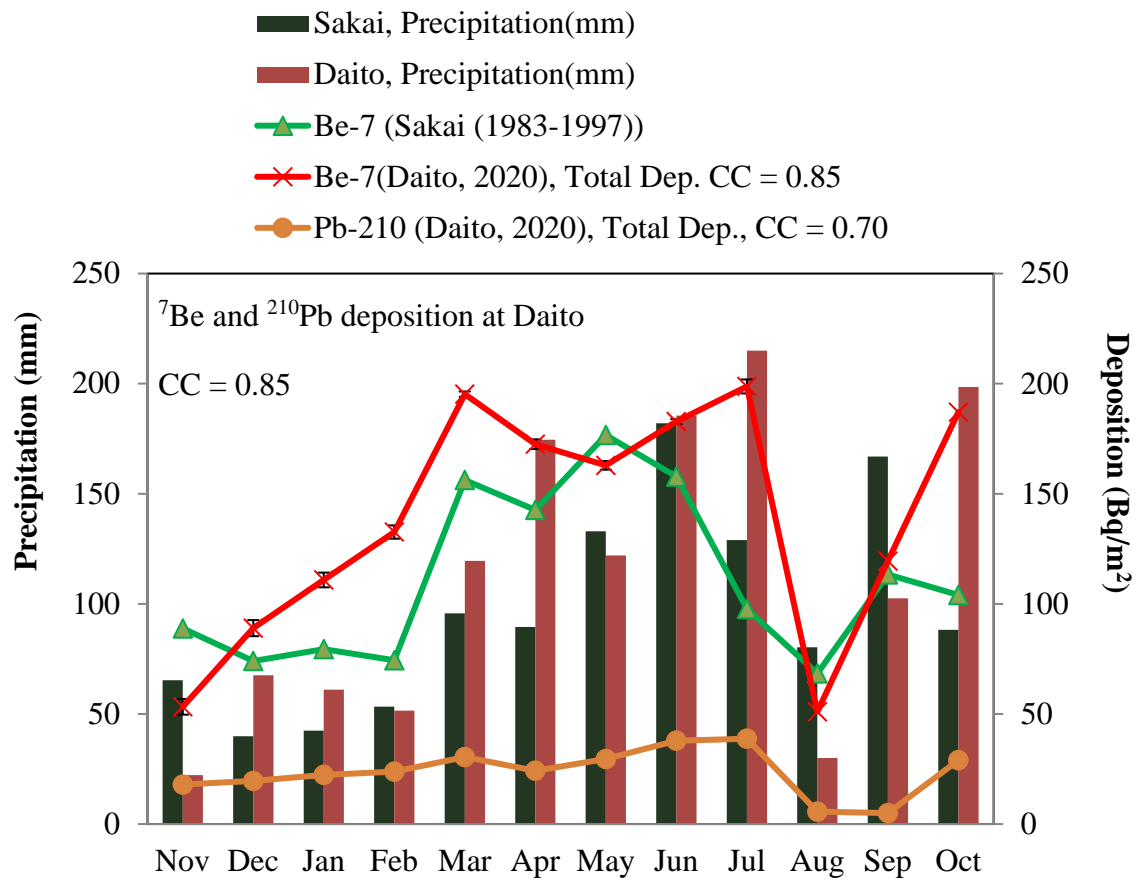


Fig. 3.16 ^7Be and ^{210}Pb deposition at Daito compare with Sakai (MEGUMI et.al., 2000).

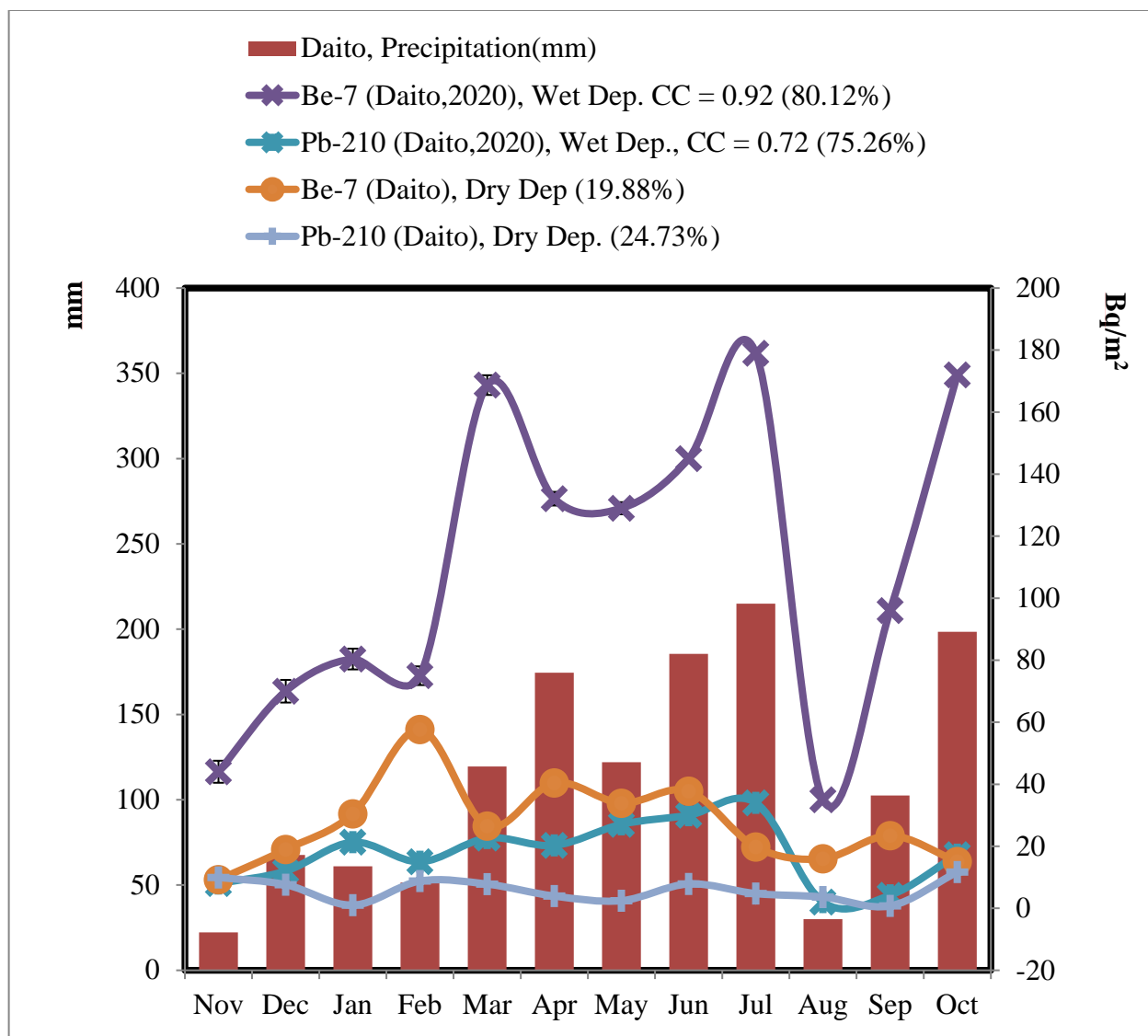


Fig. 3.17 Monthly variations of the dry and wet depositions of ^7Be and ^{210}Pb .

3.3. Aerosol size and Chemical form

A typical plot of the activity and mass size distribution of ^7Be and inorganic ion, respectively versus the particle diameters are shown. This distribution was plotted by from the average of 6 measurements, the samplings period was June 6, 2020 to August 28, 2020. AMADs were calculated from the 2-point interpolation of the data points representing the cumulative mass/activity percent above and below 50%. GSD was calculated from the 2-point interpolation

of the data points representing the cumulative mass/activity percent above and below 16%. GSD has no unit because it was calculated as the square root of the ratio of the diameter at 84% the cumulative percent to 16% the cumulative percent of the mass/activity (W. C. Hinds, 1999). Peak is the particle diameter size range found the highest mass/activity concentration. **Fig. 3.18** (a) shows a plot of the activity size distribution of ^7Be versus the particle diameter sizes. The accumulated measurement data during summer of 2020, showed the AMAD varied from 0.49 to 0.70 μm ($0.63 \pm 0.15 \mu\text{m}$), and mean was $0.53 \pm 0.18 \mu\text{m}$. GSD calculated from 2-point of the diameter sizes were 0.30, peaked in the 0.33 ~ 0.55 μm diameter sizes range, and $2.01 \pm 0.63 \mu\text{m}$, GSD was 2.50. In 2017, R. Matsubara et al. reported the study at Nagano, sampling site at the height 20 m AGL, and the period from May 25th to June 15th, 2016 that AMAD varied from 0.44 to 0.67 μm , peaked in the 0.33 ~ 0.76 μm diameter sizes range, and mean was $0.58 \pm 0.06 \mu\text{m}$ [30]. Our result was in a good agreement with the result at Nagano. Atmospheric aerosol size distribution has 2 main classes with the particle sizes ranging from 0.005 to 2 μm for fine particles and greater than 2 μm for coarse particles. The fine particle includes 2 size ranges: 1) Aitken nuclei, having sizes ranging from 0.005 to 0.05 and 2) accumulation particles having sizes ranging from 0.05 to 2 μm . [31]. In 1975, Young et al. mention that in the atmosphere, ^7Be is attached primarily to submicron-sized particles and report that about 88% of ^7Be was found on particles smaller than 1.1 μm in diameter [32]. In this study, the result showed that about 72.12%, 84.95 %, and 15.02% of ^7Be activity was presented on particles diameter smaller than 1.1, and 2 μm (fine particles), and greater than 2 μm (coarse particles), respectively. In 2009, P. Constantin [33] reported the 2 year period study at Thessaloniki, Greece (40.38°N, 22.58°E) that 69% of the ^7Be activity was associated with aerosol particles with diameter smaller than 1.1 μm with AMAD 0.9 μm (GSD = 2.24) at 20 m AGL, AMAD 0.68 μm (GSD = 2.18) at 250 m AGL, and AMAD 0.62 μm (GSD = 2.24) at 1000 m AGL. The ^7Be activity size distribution dominated a smaller size range of particles

diameter, showing a dependency on height [33]. On particles smaller than 1.1 μm in diameter, P. Constantin (2009) found the percent of ^7Be activity smaller than this study and AMAD greater than this study may because of the sampling site's height lower than our sampling site. However, the important parameter associated with AMAD not only the height AGL but also depending on the relative air humidity and local weather (A. Mohamed, 2005). The low humidity and high temperature in the period of this study (summer of 2020) contribute to the transport of fine particles in the air [34]. On the other hand, our result comparable with the study at Nagano reported by R. Matsubara et al. (2017) due to its study during the late of spring to early of summer. **Fig. 3.18** (b) ~ (f) show the typical plot of the inorganic ion mass size distribution in summer versus the particle diameters. **Fig. 3.18** (b) and (c) found the size distribution pattern of sulfate (d) and ammonium (c) ion had similar pattern and a major fraction in accumulation particle with MMAD of $0.63 \pm 0.15 \mu\text{m}$ (GSD = 2.66) and $0.61 \pm 0.15 \mu\text{m}$ (GSD = 2.64), respectively. **Fig. 3.18** (d) found a major fraction of nitrate ion in coarse particle with MMAD of $2.19 \pm 0.98 \mu\text{m}$ (GSD = 2.33). **Fig. 3.18** (e) and (f) show the MMAD of sodium and chloride ion were $2.18 \pm 0.98 \mu\text{m}$ (GSD = 4.59) and $2.01 \pm 0.63 \mu\text{m}$ (GSD = 2.66), respectively. The mass size distribution of sulfate and ammonium ion had similar pattern with the ^7Be activity size distribution. The results of this study in agreement with R. Matsubara et al (2017) who reported that dominant ionic species were sulfate ion among anions and ammonium ion among cations, and their MMAD were almost identical to the AMAD of ^7Be activity size distribution [30]. **Fig. 3.19** show the typical plot of the inorganic ion mass size distribution in December (winter) versus the particle diameters. December data didn't show the size distribution of ^7Be because we have not enough time measurement **Fig. 3.19** (a) and (b) found the size distribution pattern of sulfate (a) and ammonium (b) ion had similar pattern and a major fraction in accumulation particle with MMAD of $0.64 \pm 0.15 \mu\text{m}$ (GSD = 2.59) and $0.55 \pm 0.14 \mu\text{m}$ (GSD = 2.59), respectively. **Fig. 19** (c) found a major fraction of nitrate ion in coarse particle

with MMAD of $3.04 \pm 0.98 \mu\text{m}$ (GSD = 3.29). **Fig. 19** (d) and (e) show the MMAD of sodium and chloride ion were $2.91 \pm 0.99 \mu\text{m}$ (GSD = 2.79) and $3.01 \pm 0.99 \mu\text{m}$ (GSD = 2.95), respectively. The mass size distribution of inorganic species in winter have similar pattern in summer. But the MMAD in winter almost found bigger than summer. In general, winter season have higher humidity than summer. The explanation for this behaviour is that the aerosols behave as nuclei for water vapour condensation in the atmosphere; that is an important growth mechanism for submicrometer aerosol particles. When humidity is higher, their size increases that why we almost found the MMAD in winter greater than summer.

Fig. 3.20 shows biweekly ^7Be activity (a) and ionic species mass (b ~ f) concentration observed at Daito, Osaka in summer of 2020. The total ^7Be activity concentration ranged from 3.63 to 9.67 mBq/m³ (mean $1.40 \pm 0.29 \text{ mBq/m}^3$). The comparison between the variation of the total ^7Be activity concentration and ionic species mass concentration found only sulfate ion that had similar pattern with ^7Be activity concentration. This result was different from R. Matsubara et al. (2017) [30] reported that ^7Be activity, sulfate ion, and ammonium ion mass concentration have the similar variation and seasonal pattern; it might be caused by the origin of the inorganic species, local weather and airflow origin. However, in order to confirm the result, since its airflow origin is different, the winter data is quite important. Thus, continuous measurement and analysis are required. The mass concentrations followed the sequence of sulfate ion > nitrate ion > sodium ion, chloride ion > ammonium ion. Sulfate ion found the highest mass concentration; it might be pointed out that in the area of study the major pollution came from man-made activity. Experimental data showed the sequence of sulfate ion was preponderant ions in the fine particle mode and then nitrate ion in the coarse particle mode at all sampling periods. The sources of sulfate ion and nitrate ion not only included anthropogenic activity, but also mainly associated

with the secondary pollutants formed from SO_2 and NO_x . NH_4^+ dominated their respective mass concentrations in the fine and coarse modes, respectively [35].

Fig 3.21 shows the percent of activity/mass was found in fine ($<2\ \mu\text{m}$) and coarse ($>2\ \mu\text{m}$) particles found that more than 80% of ^7Be activity, and sulfate ion and ammonium ion mass were found in fine particles, their aerosols were principally in the fine mode in agreement with Wang et al. (2013) and Ye Tao et al. (2014) suggesting that the homogeneous gas-phase reaction between ammonia and acidic sulfate was the dominant formation mechanism of ammonium sulfate 72.62% of nitrate ion mass was found in coarse particles, it was principally in the coarse mode, this might be explained by coarse particle nitrate ion was formed in the reaction of nitric acid with sea- and soil-derived coarse particles [36]. About 50% of sodium ion and chloride ion mass were observed both in fine and coarse particles may depend on the origins. One major source of chloride in the coarse mode particle is sea-salt, in which chloride is mainly distributed in coarse particle and is associated with sodium [37, 38]. For the fine mode, sodium and chloride ion should have another formation except the sea salt. The fine particles may come from combustion sources, including incinerators and power plants [39, 40] and secondary aerosol formation [41].

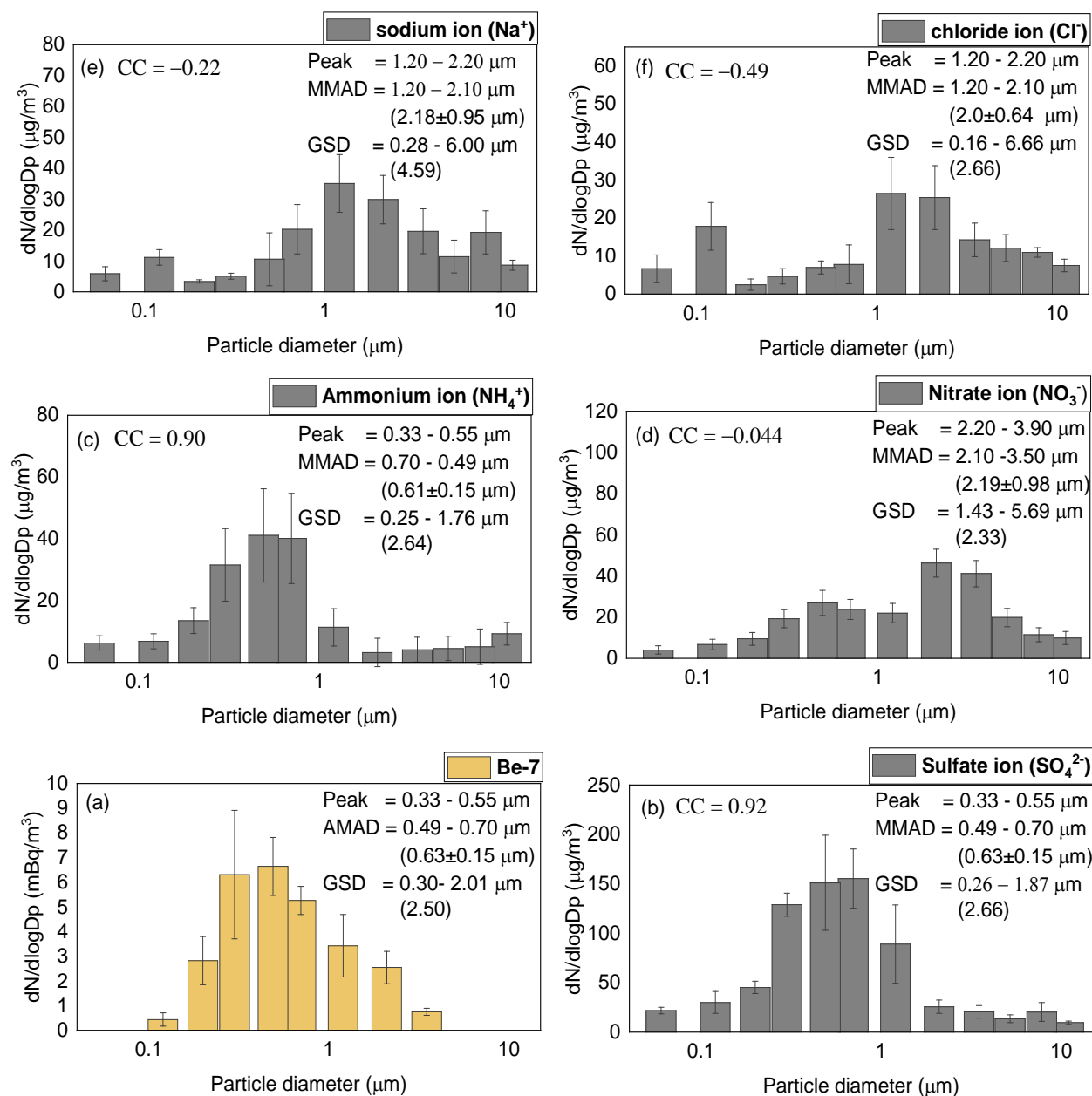


Fig. 3.18 The size distribution of ⁷Be compare with inorganic spices in summer.

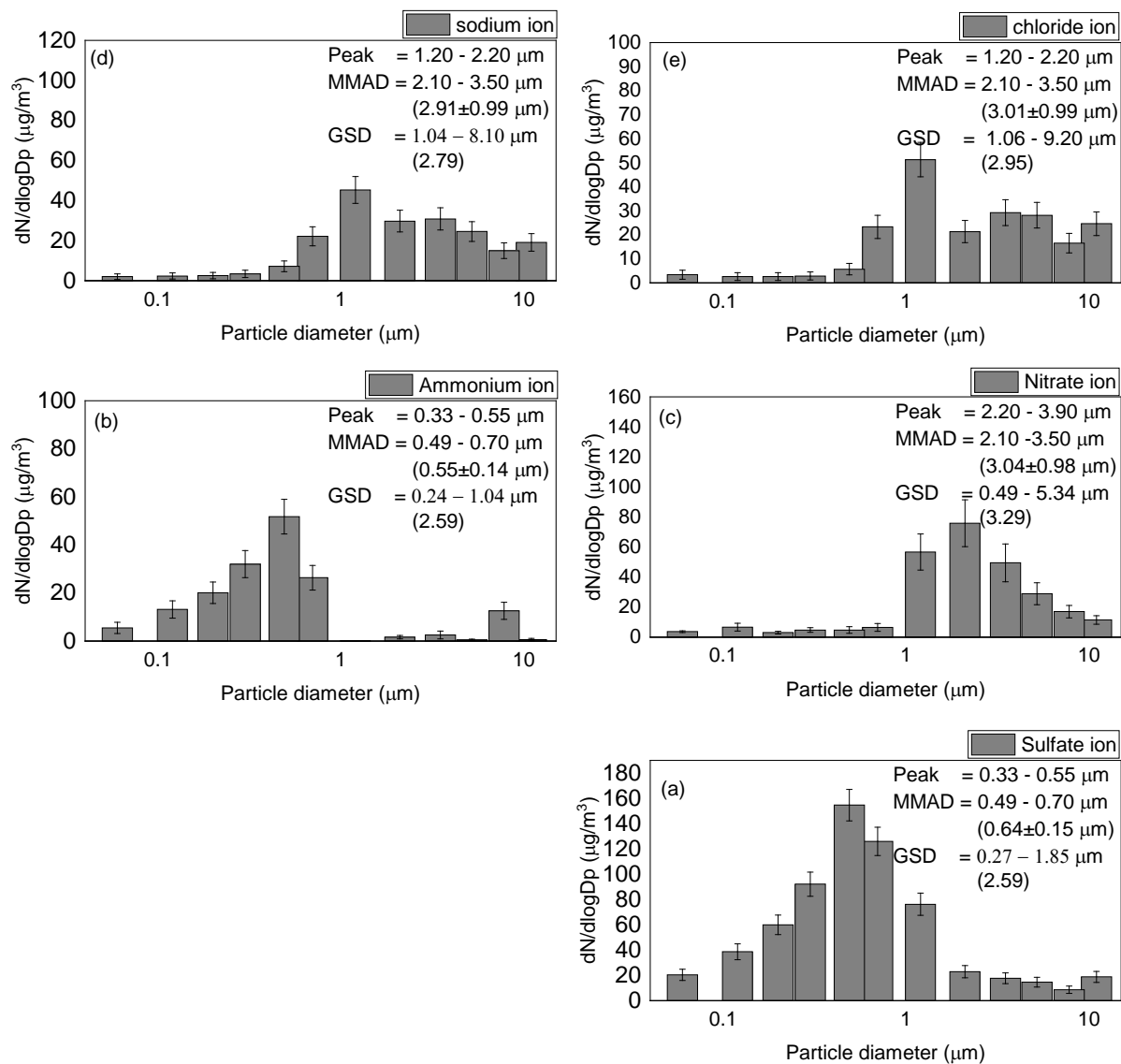


Fig. 3.19 The size distribution of inorganic species in winter.

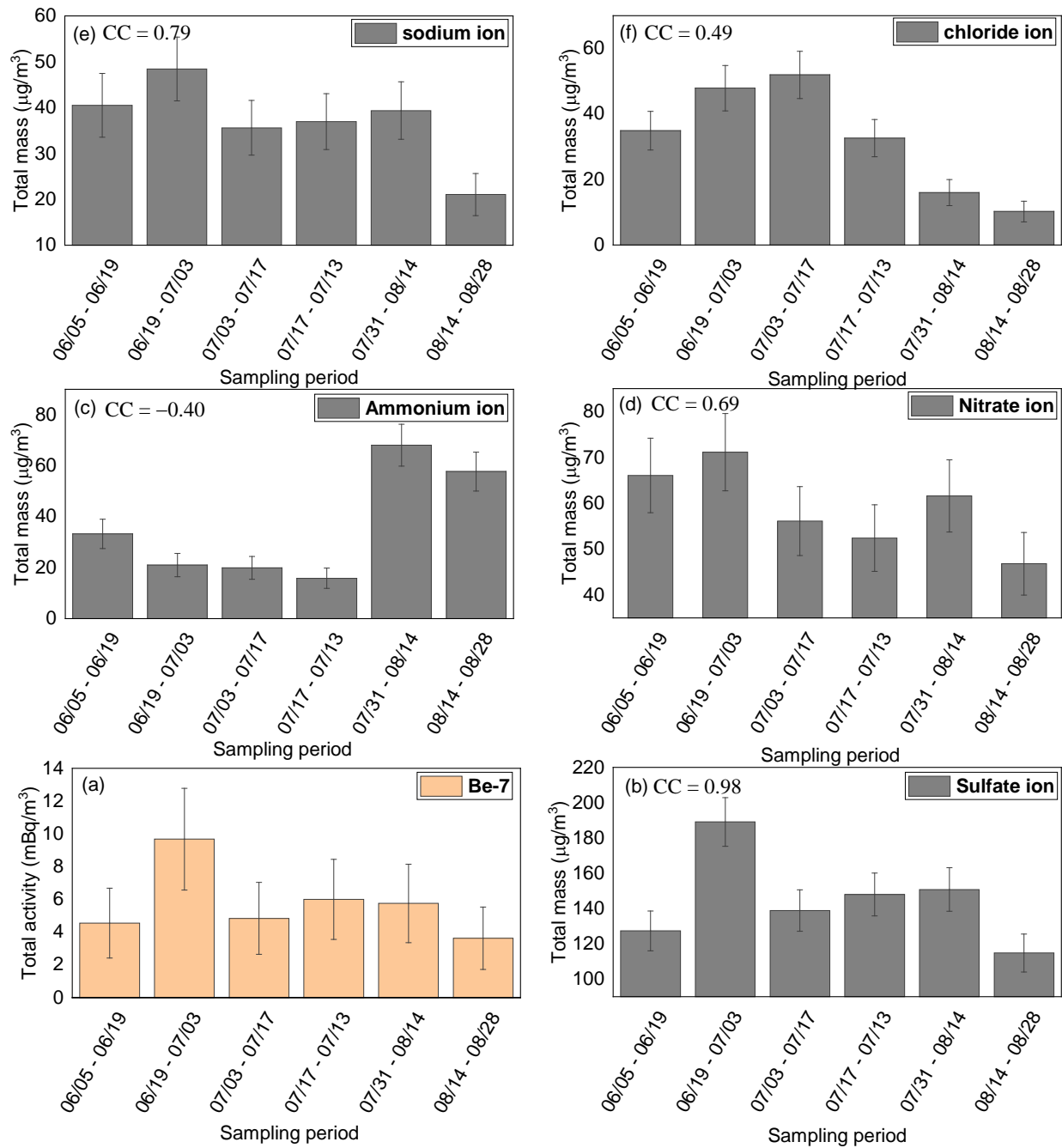


Fig. 3.20 The variation of ^7Be compare with inorganic species in summer.

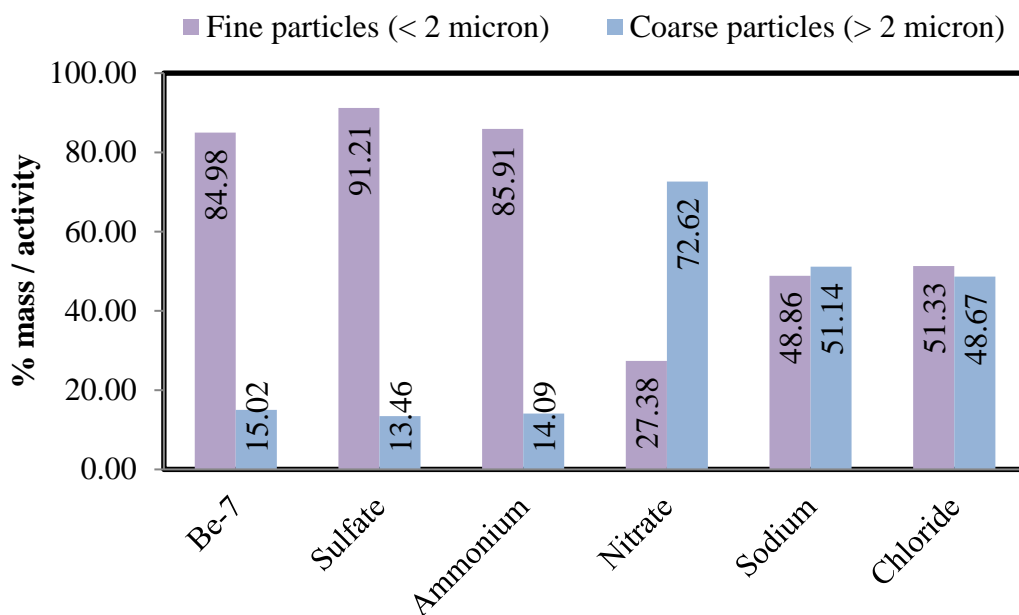


Fig. 3.21 The percent fraction of ^7Be activity and ionic species mass below $2\ \mu\text{m}$ for fine particles and larger than $2\ \mu\text{m}$ for coarse particles.

Reference

- [1] Detection of Ruthenium 106 in France and in Europe: Results of IRSN's investigations, Radioprotection and Nuclear Safety Institute (IRSN), French: https://www.irsn.fr/EN/newsroom/News/Pages/20171109_Detection-of-Ruthenium-106-in-France-and-in-Europe-Results-of-IRSN-investigations.aspx (obtained on 2021/1/09).
- [2] C.M. Lederer, V.S. Shierley, 1978, Table of Isotopes, Wiley, New York.
- [3] SCK•CEN publishes study on the presence of radioactive ruthenium-106 together with the RMI, the Belgian nuclear research centre, Belgian <https://www.zerohedge.com/news/2017-10-06/spike-airborne-radioactivity-detected-europe-source-located-southern-urals> (obtained on 2017/12/21).
- [4] Spike In Airborne Radioactivity Detected In Europe, Source Located In Southern Urals, Federal Office for Radiation Protection (FORP), Germany: https://www.sckcen.be/en/News/20171221_Ruthenium (obtained on 2017/11/20).

- [5] W. M. Chan et al. 1921, Development of CANDLES low background HPGe detector and half-life measurement of ^{180}Tm , AIP Conf. Proc. 030004-1–030004-6; <https://doi.org/10.1063/1.5018991>.
- [6] Jianglin Wang and Ryuta Hazama, 2016, Variation of ^7Be concentration in surface air and $\text{PM}_{2.5}$ with the solar activity, *KEK Proceedings*, 8 239.
- [7] Noithong, P. and Hazama, R., 2018, Variation of ^7Be concentration in surface air at Osaka, Japan, *Proceedings of 19th workshop on Environment Radioactivity*, (10) 248.
- [8] Kazuko Megumi, Tadao Matsunami, Norio Ito, Shunji Kiyoda, Akira M0, Takeyoshi A., Factors, 2000, especially sunspot number, causing variations in surface air concentrations and depositions of ^7Be in Osaka, Japan, *GEOPHYSICAL RESEARCH LETTERS*, 27(3), 361–364.
- [9] H. Muramatsu, S. Yoshizawa, T. Abe, T. Ishii, M. Wada, Y. Horiuchi, R. Kanekatsu, 2008, Variation of ^7Be concentration in surface air at Nagano, Japan, *Journal of Radioanalytical and Nuclear Chemistry* 275(2), 299–307.
- [10] Satoshi K, Hirohisa S, Shuichi G and Fuyuki T, 2009, *J. Environ. Radioact.* 100 515-21.
- [11] D Napitupulu1*, R Rahim, D Abdullah3, MI Setiawan4, LA Abdillah5, AS Ahmar6, J Simarmata, R Hidayat8, H Nurdianto9, A Pranolo, 2018, Analysis of Student Satisfaction Toward Quality of Service Facility, *IOP Conf. Series: Journal of Physics: Conf. Series* 954, 012019.
- [12] N. Akata, H. Kawabata, H. Hasegawa, K. Kondo, T. Sato, Y. Chikuchi, S. Hisamatsu, J. Inaba, 2009, Air mass origins by back trajectory analysis for evaluating atmospheric ^{210}Pb concentrations at Rokkasho, Aomori, Japan. *Journal of Radioanalytical and Nuclear Chemistry* 279(2), 493–498.
- [13] D. Sarvan, Đ. Stratimirović, S. Blesić, V. Djurdjevic, V. Miljković, J. Ajtić, 2017, Dynamics of beryllium-7 specific activity in relation to meteorological variables, tropopause height, teleconnection indices and sunspot number, *Physica A* 469, 813–823.
- [14] M.M. Rajacic, D.J. Todorovic, J.D. Krneta Nikolic, M.M. Jankovic, V.S. Djurdj, 2001, The Fourier analysis applied to the relationship between ^7Be activity in the Serbian atmosphere and meteorological parameters, *Environmental Pollution* 216, 919–923.
- [15] Andrey S. Neroda, Anna A. Goncharova, Vladimir A. Goryachev, Vasily F. Mishukov, Natalia V. Shlyk, 2016, Long-range atmospheric transport Beryllium-7 to region the Sea of Japan, *Journal of Environmental Radioactivity* 160, 102–111.
- [16] C.Papastefanou, A.Ioannidou, 1995, Aerodynamic size association of ^7Be in ambient aerosols, *Journal of Environmental Radioactivity* 26(3), 273–282.

- [17] Piñero García F, Ferro García MA, Azahra M, 2012, ^7Be behaviour in the atmosphere of the city of Granada January 2005 to December 2009. *Atmospheric Environment* 47, 84–91.
- [18] P Noithong, A Rittirong, and R Hazama, 2019, Study of the factors influence on variation of Be-7 concentration in surface air at Osaka, Japan, *IOP Conf. Series: Journal of Physics*, 1285.
- [19] Fang GC, Zhuang YJ, Cho MH, Huang CY, Xiao YF, Tsai KH, 2018, Review of total suspended particles (TSP) and PM_{2.5} concentration variations in Asia during the years of 1998–2015. *Environ Geochem Health* 40, 1127–1144.
- [20] Kanai Y, Ohta A, Kamioka H, Imai N, Shimizu H, Takahashi Y, Kai K, Hayashi M, Zhang R, 2005, Observation of mass concentration and particle size of atmospheric aerosol in east Asia and dry deposition in Tsukuba in combination with optical particle counter observation. *Bull Geolog Surv Jpn* 56, 273–301.
- [21] Naofumi Akata, Chie Iwata, Miki Nakada, Masahiro Tanaka, Hideki Kakiuchi, Tibor Kovács, 2021, Fumitaka Yanagisawa, Yutaka Kanai, Characterization of atmospheric ^{210}Pb concentration and its relation to major ion species at Tsukuba, Japan, *Journal of Radioanalytical and Nuclear Chemistry*, <https://doi.org/10.1007/s10967-020-07568-w>.
- [22] Akata N, Hasegawa H, Kawabata H, Chikuchi Y, Sato T, Ohtsuka Y, Kondo K, Hisamatsu S, 2007, Deposition of ^{137}Cs in Rokkasho, Japan and its relation to Asian dust. *J Environ Radioact* 95, 1–9.
- [23] Suzuki S. et. al., 2017, Observation of cosmogenic nuclide Be-7 concentrations in the air at Bangkok and trajectory analysis of global air-mass motion, *35th International Cosmic Ray Conference-PoS ICRC2017*, 10–20.
- [24] NOAA, Air Resources Laboratory, www.arl.noaa.gov/HYSPLIT_info.php, (Retrieved on 2020/05/20). CANBERA, Extended Range Coaxial Ge Detectors, 2016, <https://www.gammapdata.se/assets/Uploads/XtRa-detectors-C49310.pdf> (Retrieved on 2018/12/20).
- [25] Nicolas Preiss, Marie-Antoinette M61ires, and Michel Pourchet, 1996, A compilation of data on lead 210 concentration in surface air and fluxes at the air-surface and water-sediment interfaces, *JOURNAL OF GEOPHYSICAL RESEARCH*, VOL. 101, NO. D22, PAGES 28,847-28,862.
- [26] H. Itoh, Y. Narazaki, 2017, Meteorological Notes for Understanding the Transport of Beryllium-7 in the Troposphere, *Jpn. J. Health Phys.*, 52 (2), 122–133.
- [27] Lucrezia terzi, Gerhard Wotawa, Michael Schoeppner, Martin Kalinowski paul R. J. Saey, Philipp Steinmann, Lan Luan and paul W. Staten, 2020, Radioisotopes demonstrate changes in global atmospheric circulation possibly caused by global warming, *Scientific RepoRtS* 10:10695 | <https://doi.org/10.1038/s41598-020-66541-5>.

- [28] Y. NARAZAKI, K. FUJITAKA, S. IGARASHI, Y. ISHIKAWA, N. FUJINAMI, J., 2003, *Radioanal. Nucl. Chem.*, 256, 489.
- [29] N. Momoshima, S. Nishio, Y. Kusano, A. Fukuda, A. Ishimoto, 2006, Seasonal variations of atmospheric ^{210}Pb and ^7Be concentrations at Kumamoto, Japan and their removal from the atmosphere as wet and dry depositions, *Journal of Radioanalytical and Nuclear Chemistry* 268(2), 297–304.
- [30] R. Matsubara, M. Hiwatashi, A. Kondo, and H. Muramatsu, 2017, ^7Be and ionic species included in water-soluble aerosols classified by a 12-stages cascade impactor, 18th workshop on Environment Radioactivity 9, 327 - 332.
- [31] W. C. Hinds, 1999, *Aerosol Technology. Properties, Behavior, and Measurement of Airborne Particles*, 2nd ed. Wiley-VCH Verlag GmbH & Co., Weinheim.
- [32] J. A. Young, T. M. Tanner, C. W. Thomas, N. A. Wogman, and M. R. Petersen, 1975. Concentrations and Rates of Removal of Contaminants from the Atmosphere in and Downwind of St. Atmospheric Sciences 6(5), 70 - 76.
- [33] P. Constantin, 2009, Beryllium-7 Aerosols in Ambient Air, *Aerosol and Air Quality Research* 9(2), 187 -1 97.
- [34] M. Długosz-Lisiecka and H. Bem, 2020, Seasonal fluctuation of activity size distribution of ^7Be , ^{210}Pb , and ^{210}Po radionuclides in urban aerosols, *Journal of Aerosol Science*, 144(105544).
- [35] L. Bencs, K. Ravindra, J. de Hoog, E. O. Rasoazanany, F. Deutsch, N. Bleux, P. Berghmans, E. Roekens, A. Krata and R. V. Grieken, 2008, Mass and ionic composition of atmospheric fine particles over Belgium and their relation with gaseous air pollutants, *Journal of Environmental Monitoring, Journal of Environmental Monitoring*, 10, 1148 – 1157.
- [36] T. A. Pakkanen, 1996, Study of formation of coarse particle nitrate aerosol, *Atmospheric Environment*, 30(14), 2475 - 2482.
- [37] J. D. Herner, Q. Ying, J., Aw, O. Gao, D. P. Y. Chang, and M. J. Kleeman, 2006, Dominant mechanisms that shape the airborne particle size and composition in central California. *Aerosol Sci. Technol.* 40, 827 – 844.
- [38] J. Zhao, F. Zhang, Y. Xu, and J. Chen, 2011, Characterization of water-soluble inorganic ions in size-segregated aerosols in coastal city, Xiamen, *Atmospheric Research*, 99, 546 – 562.
- [39] M. A. Leiva, G. R. Toro, R. G. E. Morales, M. A. Ríos, and M. R. Gonzalez, 2014, A study of water-soluble inorganic ions in size-segregated aerosols in atmospheric pollution episode, *Int. J. Environ. Sci. Technol.* 11, 437 – 448.

- [40] N. Kaneyasu, H. Yoshikado, K. Sakamoto, and M. Soufuku, 1999, Chemical forms and sources of extremely high nitrate and chloride in winter aerosol pollution in Kanto Plain of Japan. *Atmos. Environ.*, 33, 1745 – 1756.
- [41] Y. Zhao, and Y. Gao, 2008, Mass size distributions of water-soluble inorganic and organic ions in size-segregated aerosols over metropolitan Newark in the US east coast. *Atmos. Environ.*, 42, 4063 – 4078.

CHAPTER FOUR

CONCLUSION

The sampling period from January, 2018 to December, 2020, the ^{210}Pb concentration in the air in Daito ranged from 0.42 to 1.9 mBq/m^3 with an average of 0.78 mBq/m^3 . The ^7Be concentrations in the air in Daito ranged from 2.15 to 8.84 mBq/m^3 and an average was 5.03 mBq/m^3 . K. Megumi et al., 2000 [1] reported 6.06 mBq/m^3 of ^7Be atmospheric concentration as an average during the period from 1983 to 1997 and ranged from 3.05 to 7.65 mBq/m^3 , which was comparable to the present observation in Daito. The atmospheric concentrations of ^7Be and ^{210}Pb revealed a clear seasonal variation, the ^7Be and ^{210}Pb concentrations have increased in autumn and spring, and decreased in summer. Similar seasonal variations with strong correlation ($\text{CC} = 0.68$) were observed in the activities for unit weight of aerosol, however, they showed more pronounced decreases on June and July 2018 than the corresponding atmospheric concentrations. The atmospheric ^7Be and ^{210}Pb concentrations show a seasonal variation, which makes us speculate on a change of ^7Be and ^{210}Pb sources in summer.

The TSP concentration ranged from 26.84 to 54.03 $\mu\text{g/m}^3$, high concentrations were observed in spring and low in summer. The relationship shows medium positive correlation ($\text{CC} = 0.51$) between ^7Be and TSP concentration. It is known that north-western monsoons from the Asian continent during the season change from winter to spring carry air mass with natural and/or anthropogenic materials from continent to Japanese island. [2]. Obviously heavier weight aerosol, 54 $\mu\text{g/m}^3$ was observed on March and April 2019 as compared to other seasons, 26 $\mu\text{g/m}^3$ on July and August 2019, 42 $\mu\text{g/m}^3$ in autumn and spring 2019. The decrease of activity for unit weight could be attributed to dilution by aerosol with less ^7Be and ^{210}Pb activities. The variation of ^7Be concentrations in near-surface air is commonly associated with meteorological parameters [3, 4, 5]. The correlation between the concentration of ^7Be in surface air and relative humidity and

precipitation, respectively, the negative correlation was observed in relative humidity ($cc = -0.40$) and precipitation ($cc = -0.32$). This is due to after production of ^7Be , it reacts with air constituents and turns into atoms or ^7BeO or $^7\text{Be}(\text{OH})_2$ molecules, which attached to available aerosol particles. This Isotope condenses on aerosol population, growing by condensation of non-radioactive species [6, 7]. From the correlation coefficient value, we found that relative humidity has stronger relation with ^7Be concentrations than precipitation. Note that, high humidity leads to faster aerosol deposition, thus removing adsorbed ^7Be from the surface atmosphere [5]. However, a correlation was not strong enough in both relative humidity and precipitation. Therefore, in addition to the local meteorological effect it is necessary to investigate the transport processes of ^7Be on global scale. The correlation between ^7Be concentration and $\text{PM}_{2.5}$ found a weak positive correlation ($CC = 0.30$) and it is agreed with our previous study in 2015 ($CC = 0.38$) and 2018 ($CC = 0.33$) [8]. However, the correlation between ^7Be concentration and $\text{PM}_{2.5}$ did not significantly change with the correlation data only 3 year periods. The sunspot number ($CC = -0.17$) and (g) neutron intensity ($CC = 0.02$) from cosmic ray shows very weak correlation in both factors. it should be noted that the temporal ^7Be concentration variation was not influenced by the sunspot number and neutron intensity because this study the period is short when compare with the solar cycle (11 years). TSP concentration shows strong positive correlation ($CC = 0.63$) with ^{210}Pb . The result shows the high concentration in spring, and autumn and low in summer. The high concentration of TSP in spring was observed in this area and this pattern also reported many research [9 - 12]. The weak negative correlation was found in pressure (c) ($CC = -0.27$), wind speed (d) ($CC = -0.25$), precipitation (e) ($CC = -0.25$), and relative humidity (f) ($CC = -0.23$), and a very weak correlation between the ^{210}Pb concentration and $\text{PM}_{2.5}$ ($CC = 0.12$). The results show no relationship between $\text{PM}_{2.5}$ and temporal ^{210}Pb concentration variation.

In general, as aerosols are scavenged by rain, it is considered that the ^7Be and ^{210}Pb concentrations are in low level at the large amount of precipitation. However, a weak negative correlation between the ^7Be and ^{210}Pb concentrations and precipitation was observed. Therefore, in addition to the local meteorological effect it is necessary to investigate the transport processes of ^7Be and ^{210}Pb on global scale. In this simulation, the endpoint of trajectories was set at the sampling site, with the height of 200 m, 300 m, 400 m, 500 m, 1,000 m, and 1,500 m for ^{210}Pb and the high of 2,000 m, 6,000 m, and 20,000 m above mean sea-level (MSL) for ^7Be . All altitude has similar direction and the origin of air mass. In winter, spring, and autumn the air mass direction almost came from North-West. The air mass origin almost transports from the Asia continent or east of China. It shows the high concentration of ^7Be and ^{210}Pb . [13]. On the other hand, when it was low in summer, the air mass direction almost came from East-North and East-South. The air-mass had been mainly coming from the Pacific Oceanside [14].

The annual total depositions of ^7Be and ^{210}Pb in Daito were $1655 \pm 26 \text{ Bq/m}^2$ and $284 \pm 7 \text{ Bq/m}^2$ (November 2019 ~ October 2020), respectively. The present total depositions of ^7Be were within the range of annual depositions observed over Japan. The annual distribution pattern of the total ^7Be deposition at Daito would have two peaks around spring and summer, At Sakai, which is a long term study was classified as a region of a spring peak distribution pattern [15]. Thus, the spring peak is expected for the long term study in the area. The ^{210}Pb deposition pattern is also a single peak distribution, as in the case of ^7Be . The correlation coefficient between ^{210}Pb and ^7Be depositions was very high ($\text{CC} = 0.85$), suggesting that similar mechanisms controlled the total deposition of ^7Be and ^{210}Pb . The wet deposition was obtained by subtracting the dry deposition from the total deposition, It is clear that wet deposition is important as a removal process of aerosol, occupying 75.26% for ^{210}Pb and 80.12% for ^7Be . A positive correlation between precipitation and deposition was observed, $\text{CC} = 0.70$ for ^{210}Pb and $\text{CC} = 0.88$ for ^7Be . The more considerable

precipitation-normalized deposition of ^{210}Pb than that of ^7Be in winter would suggest an enormous contribution of dry removal of ^{210}Pb in winter because the wet removal process contributed almost equally for both. The similar result was reported by N. Momoshima, et al., (2006) at Kumamoto, Japan.

The main inorganic species of PM are nitrate (NO_3^-), ammonium (NH_4^+), sulfate (SO_4^{2-}), and sea salt representing a 1:1 ratio of sodium ion (Na^+) and chloride ion (Cl^-). Every 2 weeks during June 6, 2020 to August 28, 2020, aerosols size distributions were collected and classified aerosol into 12 sizes ranging from 0.06 to 12.01 μm . The activity size distribution of ^7Be -aerosols peaked in the 0.5 ~ 0.76 μm size range. The mass size distribution of NH_4^+ and SO_4^{2-} peaked in the 0.5 ~ 0.76 μm size range, peaked in the 2.5 ~ 3.9 μm size range for NO_3^- , Na^+ , and Cl^- . The dominant ionic species were SO_4^{2-} among anions and NH_4^+ among cations, and their mass median aerodynamic diameter (MMAD) was almost identical to the activity median aerodynamic diameter (AMAD) of the ^7Be activity size distribution. For the variation of inorganic species and the variation of ^7Be , we found that only SO_4^{2-} has good agreement with the variation of ^7Be activity. Thus SO_4^{2-} would be the potential medium for ^7Be , and this inorganic species can be traced and predicted based on the behavior of ^7Be . This will can a tracer of Sulfate. Sulfate is an anthropogenic product and will be produced by burning of fossil fuels from Asian continent, especially from China.

Reference

- [1] Kazuko Megumi, Tadao Matsunami, Norio Ito, Shunji Kiyoda, Akira M0, Takeyoshi A., Factors, 2000, especially sunspot number, causing variations in surface air concentrations and depositions of ^7Be in Osaka, Japan, GEOPHYSICAL RESEARCH LETTERS, 27(3), 361–364.
- [2] Naofumi Akata, Chie Iwata, Miki Nakada, Masahiro Tanaka, Hideki Kakiuchi, Tibor Kovács, 2021, Fumitaka Yanagisawa, Yutaka Kanai, Characterization of atmospheric ^{210}Pb concentration and its relation to major ion species at Tsukuba, Japan, Journal of Radioanalytical and Nuclear Chemistry, <https://doi.org/10.1007/s10967-020-07568-w>.
- [3] D. Sarvan, Đ. Stratimirović, S. Blesić, V. Djurdjevic, V. Miljković, J. Ajtić, 2017, Dynamics of beryllium-7 specific activity in relation to meteorological variables, tropopause height, teleconnection indices and sunspot number, Physica A 469, 813–823.
- [4] M.M. Rajacic, D.J. Todorovic, J.D. Krneta Nikolic, M.M. Jankovic, V.S. Djurdj, 2016, The Fourier analysis applied to the relationship between ^7Be activity in the Serbian atmosphere and meteorological parameters, Environmental Pollution 216, 919–923.
- [5] Andrey S. Neroda, Anna A. Goncharova, Vladimir A. Goryachev, Vasily F. Mishukov, Natalia V. Shlyk, 2016, Long-range atmospheric transport Beryllium-7 to region the Sea of Japan, Journal of Environmental Radioactivity 160, 102–111.
- [6] C.Papastefanou, A.Ioannidou, 1995, Aerodynamic size association of ^7Be in ambient aerosols, Journal of Environmental Radioactivity 26(3), 273–282.
- [7] Piñero García F, Ferro García MA, Azahra M, 2012, ^7Be behaviour in the atmosphere of the city of Granada January 2005 to December 2009. Atmospheric Environment 47, 84–91.
- [8] P Noithong, A Rittirong, and R Hazama, 2019, Study of the factors influence on variation of Be-7 concentration in surface air at Osaka, Japan, IOP Conf. Series: Journal of Physics, 1285.
- [9] Fang GC, Zhuang YJ, Cho MH, Huang CY, Xiao YF, Tsai KH, 2018, Review of total suspended particles (TSP) and PM_{2.5} concentration variations in Asia during the years of 1998–2015. Environ Geochem Health 40, 1127–1144.

- [10] Kanai Y, Ohta A, Kamioka H, Imai N, Shimizu H, Takahashi Y, Kai K, Hayashi M, Zhang R, 2005, Observation of mass concentration and particle size of atmospheric aerosol in east Asia and dry deposition in Tsukuba in combination with optical particle counter observation. *Bull Geolog Surv Jpn* 56, 273–301.
- [11] Naofumi Akata, · Chie Iwata · Miki Nakada · Masahiro Tanaka³ · Hideki Kakiuchi · Tibor Kovács · Fumitaka Yanagisawa, Yutaka Kanai, 2021, Characterization of atmospheric ²¹⁰Pb concentration and its relation to major ion species at Tsukuba, Japan, *Journal of Radioanalytical and Nuclear Chemistry*, <https://doi.org/10.1007/s10967-020-07568-w>.
- [12] Akata N, Hasegawa H, Kawabata H, Chikuchi Y, Sato T, Ohtsuka Y, Kondo K, Hisamatsu S, 2007, Deposition of ¹³⁷Cs in Rokkasho, Japan and its relation to Asian dust. *J Environ Radioact* 95, 1–9.
- [13] Nicolas Preiss, Marie-Antoinette M61ires, and Michel Pourchet, 1996, A compilation of data on lead-210 concentration in surface air and fluxes at the air-surface and water-sediment interfaces, *JOURNAL OF GEOPHYSICAL RESEARCH*, VOL. 101, NO. D22, PAGES 28, 847-28, 862.
- [14] N. Akata, H. Kawabata, H. Hasegawa, K. Kondo, T. Sato, Y. Chikuchi, S. Hisamatsu, J. Inaba, 2009, Air mass origins by back trajectory analysis for evaluating atmospheric ²¹⁰Pb concentrations at Rokkasho, Aomori, Japan. *Journal of Radioanalytical and Nuclear Chemistry* 279(2), 493–498.
- [15] N. Momoshima, S. Nishio, Y. Kusano, A. Fukuda, A. 2006, Ishimoto, Seasonal variations of atmospheric ²¹⁰Pb and ⁷Be concentrations at Kumamoto, Japan and their removal from the atmosphere as wet and dry depositions, *Journal of Radioanalytical and Nuclear Chemistry* 268(2), 297–304.

Appendix

Appendix 1 Weekly Be-7 and Pb-210 (January, 2018 to September, 2020) (N.A. (negligibly small))

Collection period (Weekly)	concentration of Be-7 (mBq/m ³)	error	concentration of Pb-210 (mBq/m ³)	error
2018/01/8 - 01/15	4.56	0.04	0.98	0.10
01/15 - 01/22	6.03	0.08	1.01	0.01
01/22 - 01/29	4.97	0.07	1.10	0.14
01/29 - 02/05	5.45	0.07	0.69	0.07
02/05 - 02/12	5.88	0.08	1.35	0.13
02/12 - 02/19	6.84	0.08	0.87	0.10
02/19 - 02/26	7.06	0.08	0.57	0.06
02/26 - 03/05	7.99	0.08	0.69	0.07
03/05 - 03/12	7.55	0.08	0.88	N.A.
03/12 - 03/19	7.32	0.07	0.67	N.A.
03/19 - 03/26	5.37	0.06	0.57	N.A.
03/26 - 04/02	8.93	0.08	0.72	N.A.
04/02 - 04/09	6.88	0.07	0.01	N.A.
04/09 - 04/16	5.64	0.06	1.37	0.14
04/19 - 04/23	6.23	0.06	0.01	0.00
04/23 - 04/30	6.10	0.06	1.37	0.14
04/30 - 05/07	8.01	0.07	0.69	0.07
05/07 - 05/14	4.47	0.05	1.35	0.13
05/14 - 05/21	5.09	0.05	0.97	0.10
05/21 - 05/28	7.64	0.06	0.57	0.06
05/28 - 06/04	4.70	0.05	0.44	0.04
06/04 - 06/11	2.82	0.04	0.85	0.09
06/11 - 06/18	2.32	0.03	0.40	0.04
06/18 - 06/25	4.60	0.04	0.21	0.02
06/25 - 07/02	2.92	0.04	0.25	0.02
07/02 - 07/09	1.77	0.03	0.54	0.05
07/09 - 07/16	2.31	0.03	0.53	0.05
07/16 - 07/23	1.97	0.03	0.75	0.07
07/23 - 07/30	3.41	0.04	0.53	0.05
07/30 - 08/06	4.06	0.04	0.30	0.03
08/06 - 08/13	3.98	0.04	0.30	0.03
08/13 - 08/20	1.49	0.03	0.36	0.04
08/20 - 08/27	1.03	0.02	0.39	0.04
08/27 - 09/03	2.09	0.03	1.11	0.11
09/03 - 09/10	3.80	0.04	0.55	0.06

Collection period (Weekly)	concentration of Be-7 (mBq/m ³)	error	concentration of Pb-210 (mBq/m ³)	error
09/10 - 09/17	4.12	0.05	0.35	0.03
09/17 - 09/24	5.30	0.05	1.05	0.10
09/24 - 10/01	2.13	0.03	1.33	0.13
10/01 - 10/08	3.41	0.04	1.54	0.15
10/08 - 10/15	4.88	0.07	0.99	0.10
10/15 - 10/22	5.28	0.07	1.29	0.13
10/22 - 10/29	4.27	0.06	1.40	0.14
11/05 - 11/12	5.70	0.07	0.72	0.07
11/12 - 11/19	5.04	0.06	0.72	0.07
11/19 - 11/26	5.89	0.07	1.17	0.12
11/26 - 12/03	5.12	0.06	0.70	0.07
12/03 - 12/10	5.65	0.08	0.12	0.01
12/10 - 12/17	4.01	0.06	0.52	0.05
12/17 - 12/24	7.69	0.09	0.73	0.07
12/24 - 12/31	4.66	0.06	0.52	0.05
12/31 - 01/07	5.25	0.07	0.01	N.A.
2019/01/07 - 01/14	7.49	0.08	1.37	0.14
01/14 - 01/21	4.77	0.07	0.01	N.A.
01/28 - 02/02	5.23	0.07	1.37	0.14
02/04 - 02/11	4.81	0.07	0.71	N.A.
02/11 - 02/18	6.97	0.08	0.68	N.A.
02/18 - 02/25	7.03	0.08	0.56	N.A.
02/25 - 03/04	4.54	0.06	0.88	N.A.
03/04 - 03/11	6.77	0.08	0.67	N.A.
03/11 - 03/18	5.56	0.07	0.67	N.A.
03/18 - 03/25	6.94	0.09	0.72	N.A.
03/25-04/01	9.72	0.11	0.67	N.A.
04/01 - 04/08	5.12	0.08	0.01	N.A.
04/08 - 04/15	4.33	0.15	1.37	0.14
04/15 - 04/22	5.10	0.07	0.01	N.A.
04/22 - 04/29	5.03	0.07	1.37	0.14
04/29 - 05/06	10.08	0.10	0.69	0.07
05/06 - 05/13	8.11	0.09	1.35	0.13
05/13 - 05/20	9.69	0.10	1.07	0.10
05/20 - 05/27	7.47	0.08	0.67	0.06
05/27 - 06/03	4.94	0.10	0.69	0.07
06/03 - 06/10	5.65	0.05	0.61	N.A.
06/17 - 06/24	4.83	0.05	0.77	N.A.
06/24 - 07/01	2.29	0.03	0.56	N.A.

Collection period (Weekly)	concentration of Be-7 (mBq/m ³)	error	concentration of Pb-210 (mBq/m ³)	error
07/01 - 07/08	3.74	0.12	0.33	N.A.
07/08 - 07/15	1.87	0.05	0.45	N.A.
07/15 - 07/22	1.74	0.05	0.83	N.A.
07/22 - 07/29	2.01	0.06	0.56	N.A.
07/29 - 08/05	2.08	0.04	0.81	N.A.
08/05 - 08/12	1.60	0.04	1.01	N.A.
08/12 - 08/19	2.22	0.03	0.58	N.A.
08/19 - 08/26	3.49	0.05	0.98	N.A.
08/26 - 09/02	3.24	0.04	0.75	N.A.
09/02 - 09/09	2.18	0.03	0.91	N.A.
09/09 - 09/16	5.80	0.05	1.63	0.02
09/16 - 09/23	5.45	0.05	1.90	0.01
09/23 - 09/30	4.49	0.04	1.38	0.02
09/30 - 10/07	5.08	0.04	1.79	N.A.
10/07 - 10/14	4.53	0.14	0.98	0.10
10/14 - 10/21	6.10	0.05	1.41	0.13
10/21 - 10/28	4.85	0.04	1.10	0.14
10/28 - 11/04	9.46	0.06	0.88	N.A.
11/04 - 11/11	6.38	0.05	0.67	N.A.
11/11 - 11/18	6.65	0.05	0.88	N.A.
11/18 - 11/25	6.51	0.05	0.67	N.A.
11/25 - 12/02	6.22	0.03	0.57	N.A.
12/02 - 12/09	4.52	0.02	0.61	N.A.
12/09 - 12/16	4.66	0.03	0.67	N.A.
12/16 - 12/23	5.39	0.06	0.91	N.A.
12/23 - 12/30	4.01	0.06	0.67	N.A.
01/06 - 01/13	3.56	0.05	0.69	N.A.
01/13 - 01/20	5.63	0.06	0.80	N.A.
2020/01/20 - 01/27	4.34	0.04	0.75	N.A.
01/27 - 02/03	3.39	0.03	0.54	N.A.
02/03 - 02/10	5.17	0.04	0.73	N.A.
02/10 - 02/17	3.87	0.04	0.85	N.A.
02/17 - 02/24	5.28	0.05	0.36	N.A.
02/24 - 03/02	4.73	0.05	0.90	N.A.
03/02 - 03/09	4.76	0.04	0.71	N.A.
03/09 - 03/16	4.57	0.04	0.77	N.A.
03/23 - 03/30	3.78	0.04	0.56	N.A.
03/30 - 04/06	6.63	0.04	0.81	N.A.
04/06 - 04/13	4.46	0.04	1.01	N.A.

Collection period (Weekly)	concentration of Be-7 (mBq/m ³)	error	concentration of Pb-210 (mBq/m ³)	error
04/13 - 04/20	5.04	0.04	0.58	N.A.
04/20 - 04/27	4.64	0.04	0.98	N.A.
04/27 - 05/04	6.80	0.04	0.62	N.A.
05/04 - 05/11	7.15	0.04	0.70	N.A.
05/11 - 05/18	5.19	0.05	1.29	N.A.
05/18 - 05/25	2.46	0.04	0.45	N.A.
05/25 - 06/01	7.71	0.07	1.25	N.A.
06/01 - 06/08	2.30	0.04	0.60	N.A.
06/08 - 06/15	4.23	0.05	0.88	N.A.
06/15 - 06/22	2.89	0.04	0.68	N.A.
06/22 - 06/29	3.18	0.06	0.79	N.A.
06/29 - 07/06	2.38	0.04	0.33	N.A.
07/06 - 07/13	1.21	0.03	0.45	N.A.
07/13 - 07/20	2.84	0.04	0.83	N.A.
07/20 - 07/27	3.38	0.04	0.56	N.A.
07/27 - 08/03	4.06	0.04	0.62	N.A.
08/03 - 08/10	3.98	0.04	0.70	N.A.
08/10 - 08/17	1.49	0.03	0.57	N.A.
08/17 - 08/24	2.22	0.03	0.61	N.A.
08/24 - 08/31	3.49	0.05	0.67	N.A.
08/31 - 09/07	3.24	0.04	0.61	N.A.
09/07 - 09/14	4.01	0.05	1.63	0.02
09/14 - 09/21	8.44	0.06	0.90	0.01
09/21 - 09/28	7.02	0.07	1.18	0.02
09/28 - 10/05	3.11	0.13	0.79	N.A.

Appendix 2 Be-7 and Pb-210 deposition

The sampling period from November 2019 to August 2020

Total Be-7 and Pb-210 deposition

Month	Precipitation(mm)	Be-7(Bg/m ²)	error	Pb-210 (Bg/m ²)	error
Nov	22.2	53.24	3.55	17.92	0.63
Dec	67.6	88.98	3.65	19.61	0.65
Jan	61	110.85	3.35	22.33	0.69
Feb	51.5	132.62	3.02	23.79	0.71
Mar	119.5	198.74	3.18	30.44	0.80
Apr	174.5	172.51	2.21	24.21	0.72
May	122	162.89	1.96	29.53	0.78
Jun	185.5	182.77	1.14	37.85	0.51
Jul	215	195.24	1.22	38.75	0.52
Aug	74	90.68	3.02	21.37	0.69

Wet Be-7 and Pb-210 deposition

Month	Precipitation(mm)	Be-7(Bg/m ²)	error	Pb-210 (Bg/m ²)	error
Nov	22.2	44.03	3.42	10.97	0.81
Dec	67.6	70.00	3.42	12.00	0.80
Jan	61	80.38	1.78	21.31	0.54
Feb	51.5	75.00	2.00	15.00	0.50
Mar	119.5	118.72	1.45	22.64	0.55
Apr	174.5	94.09	3.64	20.28	0.87
May	122	119.01	1.21	27.08	0.63
Jun	185.5	125.00	1.78	30.00	0.54
Jul	215	139.00	3.00	34.00	0.50
Aug	74	76.68	2.34	18.34	0.90

Dry Be-7 and Pb-210 deposition

Month	Precipitation(mm)	Be-7(Bg/m ²)	error	Pb-210 (Bg/m ²)	error
Nov	22.2	9.21	0.10	6.95	0.13
Dec	67.6	18.98	0.16	7.61	0.11
Jan	61	30.47	1.11	1.02	0.10
Feb	51.5	57.62	0.72	8.79	0.15
Mar	119.5	80.02	1.22	7.80	0.18
Apr	174.5	78.43	1.01	3.94	0.11
May	122	43.88	0.53	2.45	0.11
Jun	185.5	57.77	0.46	7.85	0.02
Jul	215	56.24	1.26	4.75	0.01
Aug	74	14.00	0.68	3.03	0.21

Appendix 3 Result from the impactor

Sampling period from June to August 2020

The result of NO_3^- from June

Stage	Pore size (μm)	06/05 - 06/19 ($\mu\text{g}/\text{m}^3$)	06/19 - 07/03 ($\mu\text{g}/\text{m}^3$)	Average ($\mu\text{g}/\text{m}^3$)	error
IM-0	12.10	2.39	1.94	2.17	0.31
IM-1	8.50	3.53	3.62	3.57	0.06
IM-2	5.70	8.26	7.28	7.77	0.69
IM-3	3.90	15.49	16.19	15.84	0.50
IM-4	2.50	22.37	26.75	24.56	3.10
IM-5	1.25	7.06	9.28	8.17	1.57
IM-6	0.76	0.68	0.95	0.82	0.19
IM-7	0.52	0.94	0.67	0.80	0.19
IM-L1	0.33	1.90	0.38	1.14	1.07
IM-L2	0.22	0.66	0.92	0.79	0.18
IM-L3	0.13	2.05	2.07	2.06	0.02
IM-L4	0.06	0.75	1.09	0.92	0.24

The result of NO_3^- from July

Stage	Pore size (μm)	07/03 - 07/17 ($\mu\text{g}/\text{m}^3$)	07/17 - 07/31 ($\mu\text{g}/\text{m}^3$)	Average ($\mu\text{g}/\text{m}^3$)	error
IM-0	12.10	1.86	1.73	1.79	0.09
IM-1	8.50	2.33	2.76	2.55	0.30
IM-2	5.70	4.53	6.09	5.31	1.10
IM-3	3.90	9.09	10.65	9.87	1.11
IM-4	2.50	16.53	16.88	16.71	0.24
IM-5	1.25	13.79	8.79	11.29	3.53
IM-6	0.76	1.64	1.75	1.69	0.08
IM-7	0.52	1.44	1.80	1.62	0.25
IM-L1	0.33	0.63	0.60	0.61	0.02
IM-L2	0.22	0.48	0.44	0.46	0.03
IM-L3	0.13	1.87	0.41	1.14	1.04
IM-L4	0.06	1.91	0.50	1.21	1.00

The result of NO₃⁻ from August

Stage	Pore size (μm)	07/31 - 08/14 (μg/m ³)	08/14 - 08/28 (μg/m ³)	Average (μg/m ³)	error
IM-0	12.10	1.32	1.31	1.31	0.01
IM-1	8.50	2.29	2.26	2.28	0.02
IM-2	5.70	5.02	4.96	4.99	0.04
IM-3	3.90	12.59	9.83	11.21	1.95
IM-4	2.50	22.12	15.08	18.60	4.98
IM-5	1.25	9.51	6.03	7.77	2.46
IM-6	0.76	1.18	0.76	0.97	0.29
IM-7	0.52	0.91	0.62	0.76	0.20
IM-L1	0.33	0.85	0.65	0.75	0.14
IM-L2	0.22	0.68	0.95	0.81	0.19
IM-L3	0.13	3.93	3.16	3.55	0.55
IM-L4	0.06	1.20	1.19	1.20	0.01

The result of SO₄²⁻ from June

Stage	Pore size (μm)	06/05 - 06/19 (μg/m ³)	06/19 - 07/03 (μg/m ³)	Average (μg/m ³)	error
IM-0	12.10	2.07	0.64	1.35	1.01
IM-1	8.50	2.27	4.40	3.33	1.51
IM-2	5.70	2.18	2.11	2.15	0.05
IM-3	3.90	3.40	10.08	6.74	4.73
IM-4	2.50	5.19	5.08	5.14	0.08
IM-5	1.25	6.51	12.63	9.57	4.33
IM-6	0.76	21.00	46.31	33.66	17.89
IM-7	0.52	37.01	51.78	44.39	10.45
IM-L1	0.33	19.28	29.90	24.59	7.50
IM-L2	0.22	8.56	13.75	11.15	3.67
IM-L3	0.13	8.80	7.92	8.36	0.62
IM-L4	0.06	11.02	4.46	7.74	4.64

The result of SO_4^{2-} from July

Stage	Pore size (μm)	07/03 - 07/17 ($\mu\text{g}/\text{m}^3$)	07/17 - 07/31 ($\mu\text{g}/\text{m}^3$)	Average ($\mu\text{g}/\text{m}^3$)	error
IM-0	12.10	0.99	2.54	1.76	1.10
IM-1	8.50	1.32	2.27	1.80	0.67
IM-2	5.70	3.54	3.91	3.72	0.26
IM-3	3.90	3.52	6.49	5.01	2.10
IM-4	2.50	5.86	11.44	8.65	3.94
IM-5	1.25	23.20	19.72	21.46	2.46
IM-6	0.76	23.67	22.77	23.22	0.63
IM-7	0.52	20.67	25.50	23.09	3.41
IM-L1	0.33	24.92	21.05	22.99	2.73
IM-L2	0.22	11.66	10.69	11.18	0.68
IM-L3	0.13	14.25	14.40	14.32	0.11
IM-L4	0.06	5.23	7.14	6.18	1.35

The result of SO_4^{2-} from August

Stage	Pore size (μm)	07/31 - 08/14 ($\mu\text{g}/\text{m}^3$)	08/14 - 08/28 ($\mu\text{g}/\text{m}^3$)	Average ($\mu\text{g}/\text{m}^3$)	error
IM-0	12.10	1.56	1.06	1.31	0.35
IM-1	8.50	4.86	4.97	4.91	0.08
IM-2	5.70	2.53	2.57	2.55	0.03
IM-3	3.90	5.23	1.88	3.56	2.36
IM-4	2.50	5.66	7.36	6.51	1.21
IM-5	1.25	16.96	6.55	11.76	7.36
IM-6	0.76	28.44	24.33	26.38	2.90
IM-7	0.52	32.30	33.88	33.09	1.12
IM-L1	0.33	23.79	17.30	20.54	4.59
IM-L2	0.22	11.17	6.27	8.72	3.46
IM-L3	0.13	11.34	3.76	7.55	5.36
IM-L4	0.06	6.96	4.81	5.88	1.52

The result of Cl⁻ from June

Stage	Pore size (μm)	06/05 - 06/19 ($\mu\text{g}/\text{m}^3$)	06/19 - 07/03 ($\mu\text{g}/\text{m}^3$)	Average ($\mu\text{g}/\text{m}^3$)	error
IM-0	12.10	0.63	1.82	1.23	0.84
IM-1	8.50	1.22	2.08	1.65	0.61
IM-2	5.70	3.18	3.55	3.36	0.26
IM-3	3.90	2.39	5.91	4.15	2.49
IM-4	2.50	8.22	10.14	9.18	1.36
IM-5	1.25	3.33	7.47	5.40	2.93
IM-6	0.76	0.27	2.68	1.47	1.71
IM-7	0.52	0.69	1.64	1.17	0.67
IM-L1	0.33	3.40	0.26	1.83	2.22
IM-L2	0.22	1.04	0.56	0.80	0.34
IM-L3	0.13	8.93	9.03	8.98	0.07
IM-L4	0.06	1.61	2.74	2.17	0.80

The result of Cl⁻ from July

Stage	Pore size (μm)	07/03 - 07/17 ($\mu\text{g}/\text{m}^3$)	07/17 - 07/31 ($\mu\text{g}/\text{m}^3$)	Average ($\mu\text{g}/\text{m}^3$)	error
IM-0	12.10	2.63	0.09	1.36	1.79
IM-1	8.50	2.62	0.83	1.73	1.26
IM-2	5.70	3.39	0.96	2.18	1.71
IM-3	3.90	6.89	3.14	5.02	2.65
IM-4	2.50	11.21	6.53	8.87	3.31
IM-5	1.25	8.09	5.14	6.61	2.09
IM-6	0.76	0.50	4.03	2.26	2.50
IM-7	0.52	3.07	3.31	3.19	0.17
IM-L1	0.33	0.30	0.16	0.23	0.10
IM-L2	0.22	0.27	0.08	0.17	0.13
IM-L3	0.13	7.30	8.04	7.67	0.52
IM-L4	0.06	5.69	0.31	3.00	3.81

The result of Cl⁻ from August

Stage	Pore size (μm)	07/31 - 08/14 ($\mu\text{g}/\text{m}^3$)	08/14 - 08/28 ($\mu\text{g}/\text{m}^3$)	Average ($\mu\text{g}/\text{m}^3$)	error
IM-0	12.10	1.16	0.58	0.87	0.41
IM-1	8.50	2.04	2.02	2.03	0.02
IM-2	5.70	2.03	2.00	2.01	0.02
IM-3	3.90	2.26	0.70	1.48	1.10
IM-4	2.50	2.84	1.15	1.99	1.19
IM-5	1.25	1.06	0.35	0.71	0.50
IM-6	0.76	0.82	0.08	0.45	0.52
IM-7	0.52	0.26	0.32	0.29	0.05
IM-L1	0.33	0.64	0.16	0.40	0.34
IM-L2	0.22	0.64	0.80	0.72	0.12
IM-L3	0.13	1.39	1.18	1.29	0.15
IM-L4	0.06	0.86	0.85	0.86	0.01

The result of NH₄⁺ from June

Stage	Pore size (μm)	06/05 - 06/19 ($\mu\text{g}/\text{m}^3$)	06/19 - 07/03 ($\mu\text{g}/\text{m}^3$)	Average ($\mu\text{g}/\text{m}^3$)	error
IM-0	12.10	0.49	1.51	1.00	0.72
IM-1	8.50	0.27	0.36	0.31	0.07
IM-2	5.70	1.13	0.35	0.74	0.55
IM-3	3.90	1.08	0.38	0.73	0.50
IM-4	2.50	0.16	0.16	0.16	0.00
IM-5	1.25	0.08	1.91	0.99	1.29
IM-6	0.76	6.68	3.56	5.12	2.21
IM-7	0.52	8.69	4.89	6.79	2.69
IM-L1	0.33	6.55	3.38	4.96	2.24
IM-L2	0.22	3.44	2.39	2.91	0.74
IM-L3	0.13	2.87	1.36	2.12	1.07
IM-L4	0.06	1.82	0.76	1.29	0.75

The result of NH_4^+ from July

Stage	Pore size (μm)	07/03 - 07/17 ($\mu\text{g}/\text{m}^3$)	07/17 - 07/31 ($\mu\text{g}/\text{m}^3$)	Average ($\mu\text{g}/\text{m}^3$)	error
IM-0	12.10	1.53	0.87	1.20	0.47
IM-1	8.50	0.36	0.17	0.26	0.14
IM-2	5.70	0.29	0.17	0.23	0.09
IM-3	3.90	0.28	0.10	0.19	0.13
IM-4	2.50	0.16	0.11	0.13	0.04
IM-5	1.25	0.08	0.10	0.09	0.02
IM-6	0.76	1.67	2.84	2.26	0.83
IM-7	0.52	4.70	5.49	5.09	0.56
IM-L1	0.33	4.77	2.92	3.84	1.30
IM-L2	0.22	1.51	1.09	1.30	0.29
IM-L3	0.13	2.50	0.63	1.57	1.32
IM-L4	0.06	2.10	1.34	1.72	0.54

The result of NH_4^+ from August

Stage	Pore size (μm)	07/31 - 08/14 ($\mu\text{g}/\text{m}^3$)	08/14 - 08/28 ($\mu\text{g}/\text{m}^3$)	Average ($\mu\text{g}/\text{m}^3$)	error
IM-0	12.10	0.03	4.09	2.06	2.87
IM-1	8.50	0.15	3.71	1.93	2.51
IM-2	5.70	0.10	3.59	1.85	2.47
IM-3	3.90	0.51	3.77	2.14	2.31
IM-4	2.50	0.64	3.83	2.23	2.26
IM-5	1.25	4.09	4.62	4.36	0.38
IM-6	0.76	21.71	6.53	14.12	10.73
IM-7	0.52	23.87	7.06	15.47	11.89
IM-L1	0.33	9.76	5.95	7.86	2.69
IM-L2	0.22	4.11	5.97	5.04	1.32
IM-L3	0.13	2.13	4.25	3.19	1.50
IM-L4	0.06	0.98	4.32	2.65	2.36

The result of Na⁺ from June

Stage	Pore size (μm)	06/05 - 06/19 ($\mu\text{g}/\text{m}^3$)	06/19 - 07/03 ($\mu\text{g}/\text{m}^3$)	Average ($\mu\text{g}/\text{m}^3$)	error
IM-0	12.10	0.89	2.32	1.60	1.01
IM-1	8.50	1.44	9.07	5.25	5.40
IM-2	5.70	3.86	3.47	3.66	0.28
IM-3	3.90	5.12	7.16	6.14	1.44
IM-4	2.50	8.56	11.23	9.89	1.89
IM-5	1.25	8.07	6.51	7.29	1.10
IM-6	0.76	7.38	2.80	5.09	3.24
IM-7	0.52	0.91	1.62	1.27	0.50
IM-L1	0.33	1.26	0.46	0.86	0.56
IM-L2	0.22	1.19	0.69	0.94	0.35
IM-L3	0.13	7.96	1.43	4.69	4.61
IM-L4	0.06	1.89	1.68	1.79	0.15

The result of NH₄⁺ from July

Stage	Pore size (μm)	07/03 - 07/17 ($\mu\text{g}/\text{m}^3$)	07/17 - 07/31 ($\mu\text{g}/\text{m}^3$)	Average ($\mu\text{g}/\text{m}^3$)	error
IM-0	12.10	1.53	0.73	1.13	0.56
IM-1	8.50	1.57	2.82	2.19	0.89
IM-2	5.70	2.26	1.20	1.73	0.75
IM-3	3.90	4.06	7.28	5.67	2.28
IM-4	2.50	7.19	4.37	5.78	1.99
IM-5	1.25	2.44	6.37	4.40	2.78
IM-6	0.76	1.74	5.35	3.54	2.55
IM-7	0.52	2.23	6.84	4.53	3.26
IM-L1	0.33	0.50	0.97	0.74	0.33
IM-L2	0.22	0.52	0.30	0.41	0.15
IM-L3	0.13	6.40	0.42	3.41	4.23
IM-L4	0.06	5.17	0.29	2.73	3.45

The result of NH_4^+ from August

Stage	Pore size (μm)	07/31 - 08/14 ($\mu\text{g}/\text{m}^3$)	08/14 - 08/28 ($\mu\text{g}/\text{m}^3$)	Average ($\mu\text{g}/\text{m}^3$)	error
IM-0	12.10	1.23	1.22	1.23	0.01
IM-1	8.50	2.28	1.82	2.05	0.32
IM-2	5.70	2.61	0.85	1.73	1.24
IM-3	3.90	3.30	2.33	2.81	0.68
IM-4	2.50	9.66	6.17	7.92	2.47
IM-5	1.25	6.12	4.23	5.17	1.33
IM-6	0.76	2.62	1.84	2.23	0.55
IM-7	0.52	1.87	0.53	1.20	0.95
IM-L1	0.33	1.46	0.69	1.08	0.54
IM-L2	0.22	1.37	0.49	0.93	0.62
IM-L3	0.13	5.77	0.44	3.10	3.76
IM-L4	0.06	1.07	0.42	0.75	0.46

The result of Be-7 from June

Stage	Pore size (μm)	06/05 - 06/19 (mBq/m^3)	06/19 - 07/03 (mBq/m^3)	Average (mBq/m^3)	error
IM-0	12.10	N.A.	N.A.	N.A.	N.A.
IM-1	8.50	N.A.	N.A.	N.A.	N.A.
IM-2	5.70	N.A.	N.A.	N.A.	N.A.
IM-3	3.90	0.05	0.26	0.15	0.15
IM-4	2.50	0.60	1.13	0.86	0.37
IM-5	1.25	0.80	0.77	0.78	0.02
IM-6	0.76	0.40	1.70	1.05	0.92
IM-7	0.52	1.20	2.31	1.76	0.79
IM-L1	0.33	1.05	2.08	1.57	0.73
IM-L2	0.22	0.45	1.29	0.87	0.59
IM-L3	0.13	N.A..	0.14	0.07	0.10
IM-L4	0.06	N.A.	N.A.	N.A.	N.A.

The result of Be-7 from July

Stage	Pore size (μm)	07/03 - 07/17 (mBq/m ³)	07/17 - 07/31 (mBq/m ³)	Average (mBq/m ³)	error
IM-0	12.10	N.A.	N.A.	N.A.	N.A.
IM-1	8.50	N.A.	N.A.	N.A.	N.A.
IM-2	5.70	N.A.	N.A.	N.A.	N.A.
IM-3	3.90	0.13	0.25	0.19	0.09
IM-4	2.50	0.56	0.70	0.63	0.10
IM-5	1.25	0.38	0.45	0.42	0.05
IM-6	0.76	0.85	0.85	0.85	0.00
IM-7	0.52	1.16	1.70	1.43	0.38
IM-L1	0.33	1.04	1.20	1.12	0.11
IM-L2	0.22	0.64	0.65	0.65	0.00
IM-L3	0.13	0.07	0.20	0.13	0.09
IM-L4	0.06	N.A.	N.A.	N.A.	N.A.

The result of Be-7 from August

Stage	Pore size (μm)	07/31 - 08/14 (mBq/m ³)	08/14 - 08/28 (mBq/m ³)	Average (mBq/m ³)	error
IM-0	12.10	N.A.	N.A.	N.A.	N.A.
IM-1	8.50	N.A.	N.A.	N.A.	N.A.
IM-2	5.70	N.A.	N.A.	N.A.	N.A.
IM-3	3.90	0.45	0.00	0.23	0.32
IM-4	2.50	0.65	0.40	0.53	0.18
IM-5	1.25	0.70	0.20	0.45	0.35
IM-6	0.76	1.25	0.60	0.93	0.46
IM-7	0.52	1.45	1.03	1.24	0.30
IM-L1	0.33	0.50	0.80	0.65	0.21
IM-L2	0.22	0.35	0.50	0.43	0.11
IM-L3	0.13	0.40	0.10	0.25	0.21
IM-L4	0.06	N.A.	N.A.	N.A.	N.A.